Mimetic Spectral Elements for Lagrangian Hyperelasticity

A Structure-Preserving Discretisation on a Space-Time Manifold

Sahir Sujahudeen

Delft University of Technology

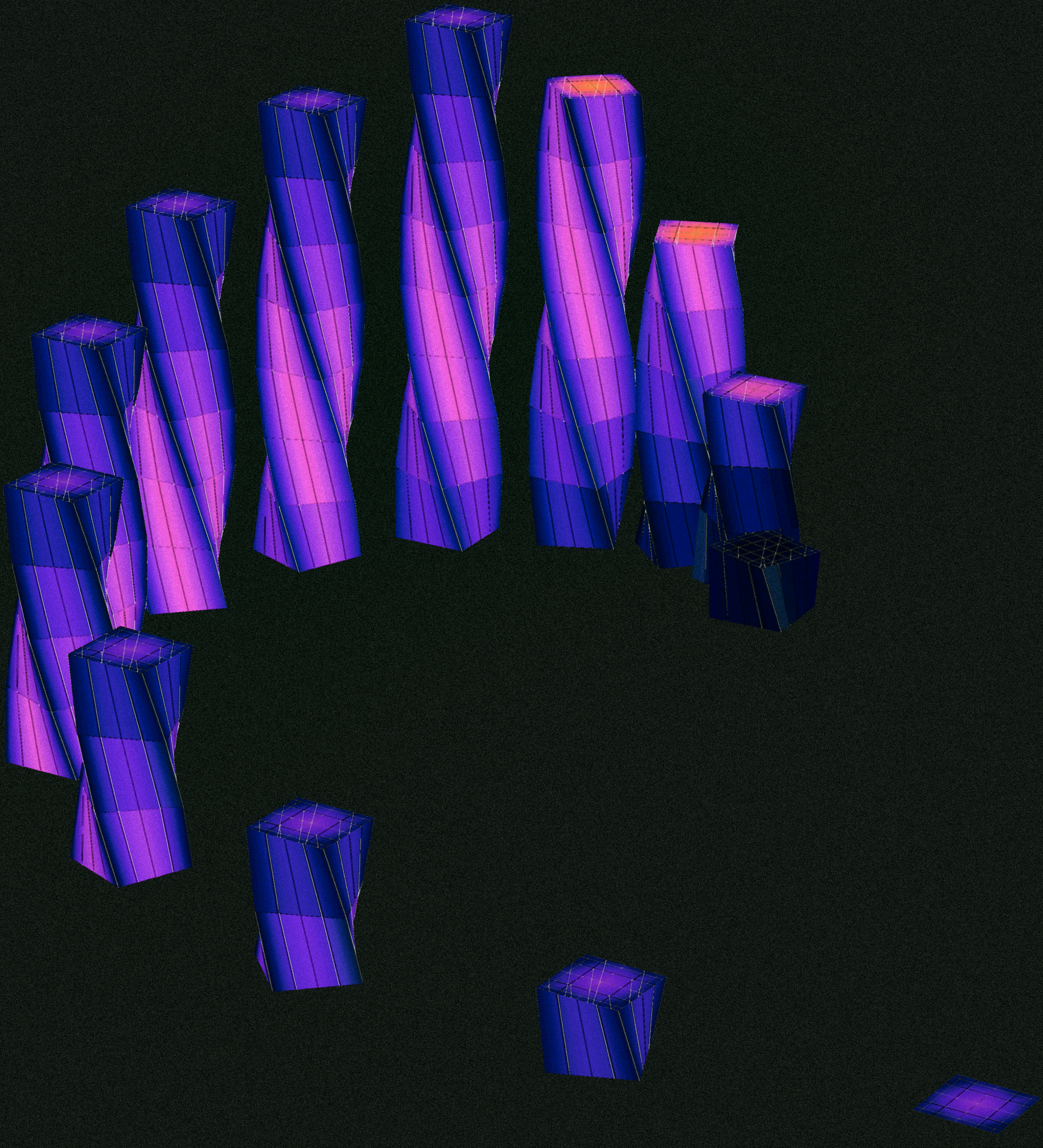

MIMETIC SPECTRAL ELEMENTS FOR LAGRANGIAN HYPERELASTICITY

A Structure-Preserving Discretisation on a Space-Time Manifold

by

Sahir Sujahudeen

in partial fulfilment of the requirements for the degree of

Master of Science
in Aerospace Engineering

at the Delft University of Technology,
to be defended publicly on Tuesday, 16 December 2025 at 9:30 AM

Track: Aerodynamics, Flow Physics and Technology (FPT)
Project duration: March, 2025 – December, 2025

Supervisors: Dr. Marc Gerritsma
Dr. Artur Palha
MSc Suyash Shrestha
Chair: Dr. Sergio Turteltaub
Examiner: Dr. Bianca Giovanardi

Cover: Simulation of space-time slabs, in $\mathbb{R}^3$, subject to an initial couple moment. Cauchy Stress σ_{xx} is coloured and occurs as the domain is in a non-inertial reference frame. Own work rendered with PyVista, though largely inspired by the visualisation suites of Nicolas Rougier and legacy works of Klaus-Jürgen Bathe.

ABSTRACT

This thesis develops a structure-preserving discretisation for modelling hyperelastic flow in a fully Lagrangian and variational flat space-time in $\mathbb{R}^3$ (two-dimensional in space, and one-dimensional in time) via the Mimetic Spectral Element Method (MSEM). Continuum mechanics is used as the primary modelling framework, and its links to differential geometry and duality are made explicit with examples. Deformations are treated as smooth mappings between configurations, with stress, and hence strain, measures understood as metric-dependent mappings. The natural construction of MSEM additionally transfers the symplectic nature of the governing equations onto a high-order discrete mesh, such that Noether invariants, i.e. conservation laws, present in the continuous formulation are upheld at the discrete level.

A generalised, isotropic hyperelastic formulation is constructed as a non-linear, deformation-dependent discrete Hodge operation. Extensions to multiple discrete space-time elements in a spatial sense are formulated through means of hybridisation. Anderson acceleration for fixed-point iterations is utilised as a robust, super-linearly-convergent alternative to stock fixed-point solvers for highly non-linear problems. Numerical experiments demonstrate convergent and conservative behaviour on non-curved geometries under linear mappings, as well as strongly-prescribed and weak boundary conditions. Additionally, the time-dependent solver admits a steady limit, which is used to validate the Hodge operation through the Cook's Membrane benchmark in plane-strain. These results support the notion that hyperelastic flow can indeed be modelled in a structure-preserving and multi-symplectic manner using a Lagrangian formulation on space-time manifolds in $\mathbb{R}^3$.

Keywords: **Finite Element Method, Structure-Preserving Discretisations, Mimetic Spectral Element Method, Differential Geometry, Non-Linear Elasticity, Continuum Mechanics, Solid Mechanics, Lagrangian Methods, Hamiltonian Mechanics, Non-Linear Dynamics, Variational Methods, Multi-Symplectic, Space-Time Finite Elements**

PREFACE

It's sort of interesting because I had actually met Artur before Marc during WI-4011-17, an unconventional pick for an aerospace student (according to Andrea). I still remember randomly showing him fancy outputs from the final assignment of AE4136 on "weird, mimetic stuff that not sure you heard of". Of course, I totally didn't know back then he had spent quite some years on the field, having been a student of Marc's. Needless to say I enjoyed both courses, and I think I knew right I wanted to find some junction between continuum physics and numerical analysis - under the both of them. They happily agreed :D

Artur, thank you so much for being such a mentor figure throughout the thesis, but also the entirety of the MSc. From motivating me to keep on with computational methods and helping a lot with building an intuition on the complicated field of geometry, it's been invaluable. I also very much owe the storyline and basis of this thesis to your fantastic PhD work. To Marc, amidst my chaotic passion for exploring various avenues I went on, I was very glad that you gave direction and clarity in pursuing this thesis. I really value the effort, care, and feedback you give to your students. To be frank, I felt overwhelmed at the start after realising just how alien the fundamentals felt compared to everything I'd done in my studies. Though I felt the capacity and space to learn just that much little more. To Suyash, thanks for all the insights and bits of debugging, and taking the time to give the much needed & sharp criticism throughout. I wish you all the best in the final bits of your PhD and the road ahead! Lastly, this thesis wouldn't be if it weren't for the brilliance of Muktesh's work. Thanks for laying the strong foundation for me to continue on and always being supportive.

Throughout the MSc and the thesis, I was surrounded by the most amazing and hard-working people, i.e. our cozy aquarium group: Ana, Ado, Nacho, Affan, Robbin, Arham, Aya, the Michaels, Bartosz, Dom, Jan, Niko, Justin, Caitlin, Ian, Luka, Philippina, Roel, Rasa, Filippo, Thommy, Archie, Gleb, and Pouyan. From lunches, dinners, movies, long coffee breaks, and making life-lasting friendships; I loved spending every bit and getting to know you individually, and you guys have always inspired me to push forward. To the many friends I made during Stratos, who continuously were a source of inspiration, comical downtime, and beach volleyball. To the first AE friends, Bhavya, Sari, Elias, Marcos (from Legendary Guitar Pieces), Julien, Wing, Tilen, Gad, and Karthik; we've all come so far! To Panos, Marcel, Jarek, Oliver, Thommy, Ellie, Jan, Ale, Lolo, Alberts, Matty, and Daniel for being there since day one. To Nienke who I absolutely loved working with and learned so much from on programming & creative thinking during my time at the Science Centre. To the DelftBlue HPC team who continually support education and provide such an invaluable resource to all of us at the TU (do go check it out). To all the many professors and fellow students, who provided counsel and guidance when I needed it. And to Pavel, Laura, Marjan, and all the inspiring minds I met through the ASML scholarship; thank you for everything. I'm so excited to see where life takes all of us and staying in touch.

Dancing was such an important part of my time here, in terms of community and as a creative outlet. To the fellow Lindy Hoppers & dancers at Blue Suede Shoes, thank you for introducing me to swing dancing and letting me contribute to the association (shoutout to our awesome committee!). In Dynamic, from our breakdance crew, to Broadway jazz, to learning ballet, and meeting many creative & passionate people; all of you guys have been so kind and I have never felt so accepted. Here's to many more of Niko's warm-ups and Shim Shams.

To the MB6 housemates who are literal family to me, thank you for all the heartfelt memories and countless experiences together. You guys made my time in Delft super cozy and gave me a place I could call home. Emma, Paul (and your amazing family who treat me like their own), Victor, Yongxing, Wiktoria, Asia, and Anne; I genuinely miss and love you all.

Delft is a truly a lovely place, but I really felt safe and because of its people. There's quite literally thousands I could name. So again, thank you all for being a part of that journey.

Lastly and importantly, I wouldn't be here if it weren't for my Deda and Mama, and all the sacrifices they've made to bring me here. And to my annoying and loving little sister, who always amazes and inspires me with how smart and talented she is (I'm not kidding); and my late aunt who I owe to teaching me most life skills. There's not a day when I don't think about you guys, especially during tea time. Artur had a proposition in his PhD thesis on it being [un]easy to feel like a foreigner in your own country at some point, and I can very much resonate with that. I always know that the folks and cousins back in Sri Lanka are stoked to see me - regardless of the years passed and the many issues back home in recent times I can't say I have been a part of. I am forever grateful for you all and being so understanding, and I will see you soon!

Sahir Sujahudeen
Delft, December 2025

CONTENTS

Abstract iii

Preface v

1 Introduction 1
- 1.1 Prior Work 2
  - 1.1.1 Discretisation: From Models to Applications 2
  - 1.1.2 The Advent of Geometric Perspectives 3
  - 1.1.3 Modern Geometric Frameworks 3
  - 1.1.4 Towards Geometric Elasticity 4
  - 1.1.5 Constitutive Models in Elasticity 4
- 1.2 Scope and Outline 4

2 Mathematical Preliminaries for Mimetic Spectral Element Method 7
- 2.1 Introduction to Mimetic Discretisations 7
- 2.2 Orientation of Entities 8
- 2.3 Differential Geometry: The Language of Forms 10
  - 2.3.1 Differentiable Manifolds 10
  - 2.3.2 Objects on Manifolds 10
  - 2.3.3 Differential Forms 11
  - 2.3.4 Pullbacks of Forms 13
  - 2.3.5 Treating Bundle-Valued Forms 15
- 2.4 Algebraic Topology: To Discrete Computation 16
- 2.5 Mimetic Spectral Discretisation 17
  - 2.5.1 Mimetic Basis functions 17
  - 2.5.2 Multi-dimensional Bases 18
  - 2.5.3 Discrete Hodge 18
  - 2.5.4 Dual Basis Functions 19

3 Continuum Mechanics Formulation 21
- 3.1 Configurations and Kinematics 21
  - 3.1.1 Material and Spatial Descriptions 21
  - 3.1.2 Flowmap: Material Coordinates 21
  - 3.1.3 Deformation Gradient 22
  - 3.1.4 A Differential Geometry Perspective 22
- 3.2 Measures of Deformation 23
  - 3.2.1 Right Cauchy-Green Tensor 23
  - 3.2.2 Green-Lagrange Strain Tensor 23
- 3.3 Stress Measures 24
  - 3.3.1 Cauchy Stress Tensor 25
  - 3.3.2 Piola-Kirchhoff Stress Tensors 25
- 3.4 Hyperelastic Constitutive Relations 25
  - 3.4.1 Hyperelasticity 26
  - 3.4.2 Isotropic Hyperelasticity 26
  - 3.4.3 Saint Venant-Kirchhoff Model 26
  - 3.4.4 Plane Strain Formulation for Two-Dimensional Problems 27
- 3.5 Geometric Structure of Elasticity 28
  - 3.5.1 Stress, a Covector-Valued Two-form 28
  - 3.5.2 Piola Transformation as a Pullback 29
  - 3.5.3 Towards MSEM 29
- 3.6 Lagrangian Variational Formulation for Hyperelasticity 30

4 Discrete Variational Formulation **31**
4.1 Strong Form . . . 31
4.2 Discrete Variable Representation . . . 31
4.3 Weak Formulation . . . 33
4.3.1 Discrete Weak Formulation . . . 33
4.3.2 Discrete Momentum-Velocity Constitutive Relation . . . 33
4.3.3 Discrete Material Law . . . 34
4.3.4 Tensor-Valued Stress Hodge Operator . . . 34
4.4 Boundary Conditions and System Assembly . . . 35
4.4.1 Initial Conditions and Temporal Coupling . . . 35
4.4.2 Spatial Boundary Conditions . . . 35
4.4.3 Boundary Augmented Saddle-Point System . . . 36
4.4.4 Complete System Matrix Structure . . . 37
4.4.5 Spatial Hybridization for Multi-Element Domains . . . 38
4.5 Discrete Mappings & Transformations . . . 39
4.5.1 Pullback of Configuration Variables . . . 39
4.5.2 Pullback of Discrete Stress . . . 40
4.5.3 Pushforward of Deformation Gradient . . . 40
4.5.4 Pushforward of Cauchy Stress in Physical Coordinates . . . 40
4.6 Discrete Symmetries and Conservation Properties . . . 41
4.6.1 Conservation of Linear Momentum . . . 41
4.6.2 Conservation of Angular Momentum . . . 42
4.6.3 Conservation of Energy . . . 44
4.6.4 Conservation of Mass . . . 45

5 Numerical Testing **47**
5.1 Non-Linear Solutions . . . 47
5.1.1 General Techniques . . . 47
5.1.2 Anderson Acceleration . . . 47
5.1.3 Convergence in Continuum Flow . . . 48
5.2 Unsteady Hyperelasticity . . . 48
5.2.1 Inducing Angular Momentum . . . 48
5.2.2 Prescribing Boundary Conditions . . . 50
5.2.3 Establishing Convergence . . . 53
5.3 Steady Hyperelasticity . . . 55
5.3.1 Cook's Membrane Benchmark . . . 55
5.3.2 Results on a Coarse Mesh . . . 56
5.3.3 *hp*-Convergence . . . 58

6 Conclusions **59**

7 Looking Ahead **61**

Bibliography **63**

1

Introduction

Elasticity - the ability of a material body to deform under load and then recover its original configuration when the load is removed - is a foundational concept in the world of continuum mechanics. In many engineering applications, the simplifying assumption of Robert Hooke's Law on elasticity pays dividends in reducing the modelling complexity of deformable matter [Hooke, 1678]. It is a rather accurate first-order, *linear* approximation of the elastic response of bodies undergoing small deformations, i.e. relative to the body itself.

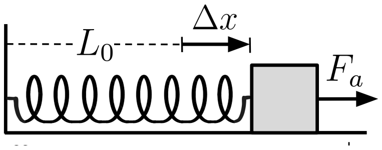

Figure 1.1: The force $\vec{F}_a$ a spring exerts on an object is related to the spring's change in length from equilibrium $\Delta\vec{x}$: $\vec{F}_a = -k\,\Delta\vec{x}$ [Khan Academy, 2025]

> *"ut tensio, sic vis"*
> *("as the extension, so the force")*
> - Robert Hooke

Nevertheless, many real-world materials and applications violate these assumptions. Consider rubber seals, biological tissue [Holzapfel and Ogden, 2025], metal subjected to high amounts of work [Jung-Ho and Noboru, 1985], or cloth & membrane deformation [Ando, 2024] are just a few to name. The deformation gradients experienced by the body are therefore no longer considered "small-enough", rotations may become significant, and the deformed configuration may depart substantially from the initial, "reference" configuration. Hooke's Law begins to break down. And so, more generally *non-linear* constitutive laws of elasticity can be formulated to capture the aforementioned effects [Fu and Ogden, 2001]. These, as a subset, may incorporate higher-order or discontinuous terms, compressibility, plasticity, dissipation, material-specific non-linearities, and their combinations [Khaniki et al., 2023] [Dastjerdi et al., 2022a].

(a) The 70.5 ft diameter parachute that delivered NASA's Perseverance Rover to the Martian surface [Airborne Systems, 2020]

(b) The Japanese cheesecake (スフレ チーズケーキ) is lighter in texture than its New York counterpart and is known for its 'jiggle' [Phil and Mama, 2020]

Figure 1.2: Examples of highly-deformable media that do not satisfy Hooke's Law

In finite-strain or non-linear elasticity, deformations can no longer be treated as small perturbations but as large, smooth "mappings" between reference and deformed configurations. This naturally supports a more *geometric* view of the problem, where deformation gradients define how lengths, areas, and orientations evolve under motion. Stress and strain thus arise as measures of change within geometry, capturing the distortion of the body's metric rather than just algebraic quantities [Yavari, 2008]. Moreover, by framing elasticity in geometric terms, one uncovers the intrinsic structure of the governing equations, revealing conservation laws and symmetries that persist even in the non-linear regime. A closely related viewpoint arises in the Lagrangian specification of flow fields, where material points are tracked as they move and deform through space-time. By expressing the governing equations in the reference frame, stresses or fluxes computed in the deformed configuration can be related back to their material origins. This treatment provides a consistent geometric foundation for continuum flow, facilitating the development formulations across multiphysics settings such as fluid–structure interaction [Demoures and Gay-Balmaz, 2022]. This recognition forms the basis for modern, structure-preserving numerical methods that seek to replicate these geometric and topological properties at the discrete level, ensuring stable and physically meaningful simulations of complex deformations.

Now, computational modelling has understandably been become invaluable for studying the complexity of elasticity and its application to the real-world [Marsden et al., 1984]. However, many traditionally-used discretisations fail to respect the aforementioned geometric and variational structure inherent to the numerical solution of partial differential equation systems [Arnold et al., 2010]. When energy and momentum are not properly conserved, simulations may exhibit artificial modes, energy drift, or non-physical deformations, in the context of elasticity. This recognition forms the basis for structure-preserving numerical methods that seek to uphold most properties - symmetries, topological identities, conservation laws, etc. - at the discrete level.

Specific to this thesis are the use of so-called mimetic (compatible) numerical discretisation methods, which extend geometric ideas into the discrete domain by "mimicking" the physics [Gerritsma, 2012]. They transfer notions of differential geometry and algebraic topology onto discrete meshes, and satisfy topological identities of vector calculus through the association of physical quantities to the geometry of the problem. Rather early on, Emily Noether presented that if a system has a continuous symmetry, then there are corresponding quantities whose values are conserved in time [Noether, 1918] - which Hamiltonian integration schemes are built upon, i.e. symplecticity [Hairer et al., 2013]. Multi-symplectic formulations generalise the symplectic nature of Hamiltonian integrators to space–time manifolds, given a Lagrangian formalism [Stern and Desbrun, 2006]. When combined with high-order spectral element techniques, these principles yield the mimetic spectral element method which bring in geometric intuition and high-order discretisations [Palha and Gerritsma, 2015]. Consequently, this thesis explores a locally space-time-embedded mimetic spectral element approach to solving Lagrangian hyperelastic flow in $\mathbb{R}^3$.[1]

1.1. PRIOR WORK

This section briefly highlights contributions to computational modelling and discretisations, the mimetic methods, and non-linear elasticity. These do not just serve to understand the material presented in either an intuitive or rigorous perspective, but can also be inspiration for future extensions and applications in this thesis.

1.1.1. DISCRETISATION: FROM MODELS TO APPLICATIONS

Partial differential equations (PDEs) constitute the mathematical backbone of physical modelling. They appear across virtually every branch of physics and engineering; from the Poisson equation [Palha et al., 2014], hyperbolic problems [Shrestha, 2022] [Georgi, 1993], electromagnetism [Griffiths, 2017], quantum mechanics [Griffiths and Schroeter, 2018], magnetohydrodynamics [Hu and Xu, 2017], and fluid dynamics [Versteeg and Malalasekera, 2007] [LeVeque, 2002] [Kreeft and Gerritsma, 2013]. These governing equations express fundamental relationships between quantities that characterize matter, energy, and geometry in motion. Broadly speaking, they consist of two types of relations: *constitutive relations*, which define the material-specific behaviour of physical quantities, and *topological relations*, which encode conservation laws that are regarded as universal.

Constitutive relations describe empirical links between conjugate variables - for example, stress and strain in elasticity, heat flux and temperature gradient in heat transfer, or flow velocity and potential in porous media - through material parameters such as stiffness, conductivity, or permeability. These relationships, while experimentally determined, inherently carry uncertainty. In contrast, topological relations express exact conservation principles, such as the conservation of energy, mass, or charge, and are typically independent of material properties. A representative example is the Poisson equation:

$$-\nabla\cdot\left(k\nabla\varphi\right)=f \tag{1.1}$$

This can be written in mixed form as

$$\mathbf{u}=k\,\nabla\varphi \tag{1.2}$$

$$\nabla\cdot\mathbf{u}=-f \tag{1.3}$$

Here the first equation represents a constitutive law (relating flux to potential) and the second expresses a topological conservation law. Depending on the physical context, these relations correspond to Fourier's law in heat diffusion, Darcy's law in porous media [Jain et al., 2020a], or analogous statements of local balance. The topological relation

---

[1] Two-dimensional in space, and one-dimensional in time

ensures that the net flux through a control volume equals the total source or sink within it - a fundamental principle across scales.

Analytical solutions to such PDEs are generally unattainable for realistic geometries or boundary conditions, requiting the use of numerical methods. Classical discretisation approaches - including finite difference [Gedney, 2011], finite volume [Versteeg and Malalasekera, 2007], and finite element methods [Zienkiewicz et al., 2006] [Ciarlet, 2002] - approximate field quantities by piecewise polynomials or local averages over a discrete mesh. While these methods achieve impressive accuracy in many settings, they rarely preserve fundamental structural properties of the governing equations. For instance, in a standard mixed finite element discretisation of the Poisson problem, the computed flux field $\mathbf{u}^h \approx \mathbf{u}$ satisfies $\nabla \cdot \mathbf{u}^h \approx 0$ only approximately, introducing small but cumulative violations of mass or energy conservation. This inconsistency can manifest as artificial sources or sinks in the simulation - numerical artifacts that degrade stability and physical realism. As a result, traditional discretisations may reproduce the *appearance* of the solution without maintaining its essential *physics*.

To mitigate such issues, *structure-preserving* or *mimetic* methods have been developed, designed to replicate at the discrete level the geometric, topological, and variational identities that underpin the continuous theory. These methods ensure that discrete operators - divergence, curl, and gradient - satisfy exact analogues of their continuous identities, such as $\nabla \cdot (\nabla \times \mathbf{A}) = 0$, or discrete forms of the Gauss and Stokes theorems. By encoding integral forms of conservation laws directly into the discrete formulation, mimetic methods preserve invariants such as energy, momentum, and mass, and maintain compatibility between adjacent physical quantities [Bochev, 2003].

1.1.2. THE ADVENT OF GEOMETRIC PERSPECTIVES

In the 1960s, staggered-mesh methods models were introduced to motivate discrete conservation of mass and momentum [Harlow and Amsden, 1968] [Lilly, 1966], i.e. the start of physics-compatible thinking. Tonti provided a rigorous theoretical framework for this intuition by formalizing the correspondence between physical quantities and geometric entities [Tonti, 1975] [Tonti, 1971]. Drawing from algebraic topology [Hatcher, 2002] and differential geometry [Frankel, 2011], he also introduced the notion that physical variables reside on geometrical supports - points, lines, surfaces, and volumes - corresponding to oriented k-cells in a cellular complex. These k-cells form *chains*, and their dual entities, *cochains*, represent discrete physical quantities such as fluxes or potentials. This revealed connections between different physical theories and provided a geometric classification of the variables and operators involved in conservation laws [Tonti, 2013].

Parallel developments emerged from geometric integration theory. Whitney [Hassler, 1957] introduced an interpolation between cochains and differential forms, later used in discrete Hodge theory [Lohi and Kettunen, 2021]. These *Whitney forms* serve as a bridge between continuous and discrete representations of differential forms, forming the foundation of mixed finite element spaces. In the 1970s and 1980s, Brezzi, Raviart, Thomas, Nédélec, and Douglas [Brezzi, 1974] [Raviart and Thomas, 1977] [Nédélec, 1980] [Brezzi et al., 1985] developed mixed finite element methods. These were later recognized as equivalent to Whitney forms in finite element settings by Bossavit - in his "Japanese Papers" collection [Bossavit, 1988] [Bossavit, 1999]. He built these ideas from computational electromagnetism, employing differential forms and Whitney elements to achieve physically consistent simulations.

1.1.3. MODERN GEOMETRIC FRAMEWORKS

By the late 1980s, a more explicit formalization of *mimetic discretisation* emerged with the development of *mimetic finite differences*. Hyman and Scovel [Hyman and Scovel, 2005] first proposed a mimetic finite difference scheme based on analogies between algebraic topology and differential forms, emphasizing that discrete differential operators must preserve identities such as symmetry and self-adjointness. Their work, and later extensions established a consistent mimetic framework for discrete differential operators [Hyman et al., 1997] [Lipnikov et al., 2006]. Bochev and Hyman proposed a unifying framework for mimetic discretisation that applied across finite difference, finite volume, and finite element contexts [Bochev and Hyman, 2006]. At its core are two key operations: *reduction*, mapping k-forms to k-cochains a simplicial complex; and *reconstruction*, which recover approximate differential forms from their discrete analogues.

Discrete Exterior Calculus (DEC) provided a geometric and algebraic framework for defining discrete analogues of the exterior derivative, codifferential, and Hodge star [Hirani, 2003] [Desbrun et al., 2005]. DEC embodies the same spirit as the mimetic framework but emphasizes a differential-geometric perspective rooted in simplicial complexes and discrete manifolds. Related to is *Finite Element Exterior Calculus* (FEEC) which formalised these concepts within the finite element setting [Arnold et al., 2006] [Arnold et al., 2010]. Another is the *Mimetic Spectral Element Method* (MSEM) [Gerritsma, 2012] [Gerritsma, 2011] [Gerritsma et al., 2014] which integrates the high-order accuracy of spectral elements with structure-preserving benefits. It provides a natural setting for formulating structure-preserving solvers in elasticity, fluid mechanics [Zhang et al., 2022] [Kreeft and Gerritsma, 2013], and other continuum systems where both topology and geometry must be respected [Palha et al., 2014]. Lastly, work on melding multi-symplectic variational principles and structure-preservation [Hairer et al., 2013] [Stern and Desbrun, 2006] [Leok and Ohsawa, 2011] sought to allow time and space to be treated symmetrically, leading to local conservation of symplectic forms in multiple dimensions [Demoures et al., 2013] [Palha and Gerritsma, 2015].

A recommendation is also made to course notes developed by Crane at Carnegie Mellon, for an intuitive and applied introduction to computational geometry [Crane et al., 2013].

1.1.4. TOWARDS GEOMETRIC ELASTICITY

This thesis assumes the use of continuum mechanics in modelling elastic media, i.e. bodies described as a *continuous* body rather than discrete particles. In a nutshell, the subject provides a framework for describing geometry, kinematics, and material behaviour amidst deformation across scales. The reader is referred to [Reddy, 2013] for a simple yet rigorous explanation of the subject and an extensive overview of applications beyond elasticity. A special recommendation is made to the freely-accessible set of open-access lecture notes provided by Massachusetts Institute of Technology (MIT), that covers the subject's mathematical preliminaries and finite elasticity applications [Abeyaratne, 2006] [Abeyaratne, 2012] [Abeyaratne, 2022].

In the context of geometry in continuum mechanics (sometimes referred to as "geometric continuum mechanics"), differential geometry is used to form a unifying framework [Rashad et al., 2023]. An elastic body is represented as an embedding of a material manifold into physical space - replacing coordinate-based descriptions with intrinsic mappings, where deformation, strain, and stress emerge from pullback and pushforward operations between the body and its configuration [Truesdell et al., 1966] [Marsden et al., 1984]. The principle of *intrinsicality* created the basis for distinguishing between Eulerian and Lagrangian in a geometric sense [Noll, 1974]. Within this setting, strain can be defined as the pullback of the ambient metric, making each deformation a point on the manifold of Riemannian metrics [Rougée, 2006], while stresses and rates of deformation naturally reside in its tangent and cotangent spaces.

From a topological perspective that separates metric-dependent relations from metric-free ones, quantities such as mass, momentum, and stress power are expressed as differential forms integrated over material or spatial manifolds [Frankel, 2011]. It was noted that these fields would be best represented using bundle-valued differential forms, which distinguish between a “form leg” - encoding the integration domain - and a “bundle-value leg” - encoding the physical quantity itself [Kanso et al., 2007]. This distinction separates spatial and material representations, where a de Rham complex can be associated, i.e. the topological foundation for FEEC and DEC [Desbrun et al., 2005] [Arnold and Winther, 2001]. Geometric discretisations of elasticity have been developed for crystalline materials [Ariza and Ortiz, 2005], finite-deformation solids [Yavari, 2008] [Angoshtari and Yavari, 2013], and Riemannian 3D elasticity [Ciarlet and Li, 2008]. Extensions have also been made to variational problems to provide more unified perspectives of Lagrangian and Hamiltonian mechanics [Marsden et al., 2001] [Demoures et al., 2013] [Demoures and Gay-Balmaz, 2022].

With regards to MSEM, recent developments have extended it towards elasticity applications, demonstrating pointwise conservation properties and providing a structure-preserving framework compatible with continuum mechanics [Olesen et al., 2018] [Zhang, 2022]. Application to linear elasticity and planar barotropic flow have been studied extensively, in addition to efforts towards non-linear problems with bundle-valued forms [Zhang et al., 2021] [Mahadev, 2025] [Sharma, 2023]

1.1.5. CONSTITUTIVE MODELS IN ELASTICITY

Constitutive models of elasticity describe how materials store and transmit energy under deformation through relations between stress and strain. For small deformations, Hooke's law adequately relates stress and strain, but at large strains or rotations, this linear assumption fails. Non-linear elasticity instead distinguishes between reference and current configurations via finite strain measures to capture large-deformation behaviour. These naturally lead to non-linear stress-strain relations [Dastjerdi et al., 2022a]. Classical contributions by Beatty [Beatty, 1996], Ogden [Fu and Ogden, 2001], and Pedregal [Pedregal, 2000] established foundational models and variational formulations for such behaviour, viewing non-linear elasticity as an extension of linear theory that incorporates geometric and material non-linearities [Reddy, 2013]. For materials exhibiting highly non-linear responses, *hyperelasticity* offers a more accurate framework: stresses are derived from a strain energy density function defined in terms of invariants of the Cauchy–Green deformation tensor [Hackett, 2018] [Boyce and Arruda, 2000]. Various hyperelastic models have been proposed, including the Neo-Hookean [Treloar, 1943], Mooney–Rivlin [Mooney, 1940][Rivlin, 1948], Gent [Gent, 1996], and Ogden [Ogden, 1973] formulations, along with numerous extended and generalized versions [Horgan, 2021] [Anssari-Benam and Bucchi, 2021] [Pucci and Saccomandi, 2002]. These models have been extensively applied to simulate large-strain behaviour in beams [Mylapilli and Udwadia, 2017] [Lubbers et al., 2017], plates [Breslavsky et al., 2014], and shells [Alijani and Amabili, 2014] [Dastjerdi et al., 2022b].

1.2. SCOPE AND OUTLINE

Given the current trend of expanding applicability of MSEM in physics, this thesis consequently aimed to investigate the following question:

Could hyperelastic flow be modelled in a multi-symplectic and structure-preserving manner, using a Lagrangian and variational approach in space-time?

To this end, the following sub-questions were also formulated, to provide a step-by-step map towards an answer to the primary goal above.

Research Question 1

Can the tensorial subject of continuum mechanics be reimagined from a differential geometry perspective and in the framework of the Mimetic Spectral Element Method?

Research Question 2

To what extent does the derived method preserve symmetries, i.e. uphold conservation laws, present in the continuous statement of the problem, and amidst the application of essential and natural boundary conditions

Research Question 3

Can the derived method illustrate convergent solutions on arbitrary, non-curved space-time geometries in $\mathbb{R}^3$?

Research Question 4

Are the discrete hyperelastic constitutive and metric-dependent operations physically representative, under the premise of refinement?

Given this schematic and these target objectives, the structure of the thesis has holistically arranged. The current Chapter 1 builds rationale for the thesis' objectives and contains reference reading material on a varity of topics (Section 1.1). Chapter 2 provides a short background to the used Mimetic Spectral Element Method (Section 2.5) from a physical problem's standpoint and duality in Section 2.1, relevance of differential geometry and forms in Section 2.3, and discrete mathematics via algebraic topology in Section 2.4. Chapter 3 introduces continuum mechanics as a framework to modelling hyperelastic flow, by firstly introducing kinematics in Sections 3.1, 3.2, and 3.3. Hyperelastic modelling is noted in Section 3.4, followed by an important link to differential geometry in Section 3.5. In Chapter 4, the discrete, variational form is posed and the construction of discrete operators (Section 4.3). The discrete system and its symmetries are stated in Section 4.4 and Section 4.6, respectively. Chapter 5 presents a short selection of notable results in steady (Section 5.3) and unsteady (Section 5.2) hyperelasticity, through a non-linear solution technique described in Section 5.1. Finally some conclusions on the work are given in Chapter 6, with some "food for thought" on shortcomings and possible, future ventures in Chapter 7.

2

MATHEMATICAL PRELIMINARIES FOR MIMETIC SPECTRAL ELEMENT METHOD

This chapter provides the mathematical background to understanding the Mimetic Spectral Element Method (MSEM). MSEM is then introduced in a concisely with a physics-driven perspective in Section 2.1 and the dual nature of variables in 2.2.The foundations of differential geometry and operations on its fundamental "form" objects are in Section 2.3, with algebraic topology as its discrete counterpart in Section 2.4. Special note is given to the pullback procedure (Subsection 2.3.4) and treatment of bundle-valued forms (Subsection 2.3.5). Finally, MSEM is introduced as well as its general implementation in Section 2.5. The reader is advised to read [Palha, 2013] [Gerritsma, 2012], for more in-depth forewords on the fundamentals of MSEM.

2.1. INTRODUCTION TO MIMETIC DISCRETISATIONS

Continuum physics is concerned with measurable quantities, such as displacement, velocity, traction and flux, and how these observables evolve across space and time. While standard vector calculus notes these as *scalars* or *vectors*, that classification alone hides the geometric setting in which each quantity is naturally evaluated. A scalar potential $\phi(x,y,z)$ is intrinsically a *pointwise* value; a velocity field $\mathbf{u}(x,y,z)$ can be sampled along paths; and a flux like $\mathbf{u}\cdot\mathbf{n}\,dA$ is accumulated over surfaces. As highlighted in Tonti's perspective [Tonti, 1975], reducing everything to “field variables” tends to blur this geometric character - an effect that is amplified when moving to differential formulations via limiting processes.

Example 2.1.1

Mass conservation offers a familiar illustration. For a fixed control volume $V \in \mathbb{R}^3$ with boundary ∂V, the total mass is $\int_V \rho\, dV$. The balance statement asserts that changes in the mass of V are caused solely by the net mass flux through ∂V:

$$\int_V \rho(t+\Delta t)\,dV - \int_V \rho(t)\,dV + \int_t^{t+\Delta t}\int_{\partial V} \rho(\tau)\mathbf{u}(\tau)\cdot\mathbf{n}\,dS\,d\tau = 0 \tag{2.1}$$

By the mean value theorem, the flux term equals $\Delta t \int_{\partial V} \rho(\tau)\mathbf{u}(\tau)\cdot\mathbf{n}\,dS$ for some $\tau \in [t, t+\Delta t]$. Dividing by Δt, taking $\Delta t \to 0$ (so that $\tau \to t$), and using the divergence theorem converts the boundary integral into a volume integral,

$$\int_V \frac{\partial \rho}{\partial t}\,dV + \int_V \nabla\cdot(\rho\mathbf{u})\,dV = 0 \tag{2.2}$$

and, since this holds for every sufficiently smooth V, we obtain the local form

$$\frac{\partial \rho}{\partial t} + \nabla\cdot(\rho\mathbf{u}) = 0 \tag{2.3}$$

The transition from the global balance (2.1) to the local expression (2.3) is mathematically sound, but it suppresses the original geometric meaning: ρ is fundamentally volumetric, and the driving term is a surface flux-facts no longer explicit once the limit is taken.

Now a more geometry-aware view keeps these roles visible from the start. More generally and structurally putting the above example, let $E(V)$ denote the conserved quantity contained in V, and let $Q(\partial V)$ be the net inflow across ∂V.

The transition from global to local statements can be posed as:

$$\frac{\partial}{\partial t}E(V) = Q(\partial V) \quad \xrightarrow[\lim V\to P]{} \quad \frac{\partial e}{\partial t} = \nabla\cdot\mathbf{q} \tag{2.4}$$

where e is the *density* (per unit volume) and $\mathbf{q}$ the *flux* (per unit area per unit time). The right-hand identity in the equation (2.4) is Gauss' divergence theorem in differential form. In $\mathbb{R}^3$, the fundamental theorem of calculus (values on the endpoints of a curve L) and Stokes' theorem (circulation along some boundary of a surface ∂S induced by a rotation in S), are also examples whereby conservation relates a global quantity attached to a object to a global quantity attached to its boundary. These connections reveal that physical variables are associated to points, curves, surfaces, and volumes; i.e. geometric objects.

Once a model is rewritten purely in local form, this geometric structure is easy to lose sight of. Traditional discretisations - finite differences and nodal finite elements - represent unknowns exclusively with nodal interpolants, which can trigger instabilities or subtly violate balance laws. Simulation therefore requires more than just function-space approximations. The relations among spaces induced by the integral balance laws should be reflected as well. Recognising that different variables live on the discrete versions of those different objects enables a setting where the discrete laws are exactly met.

Remark 2.1.1

By assigning discrete quantities to vertices, edges, faces, and volumes in a mesh, one can obtain *exact* matrix realizations of *grad*, *curl*, and *div* that satisfy the fundamental identities $\nabla\times\nabla = \mathbf{0}$ and $\nabla\cdot(\nabla\times) = 0$

Discrete Exterior Calculus (DEC) [Hirani, 2003], Finite Element Exterior Calculus (FEEC) [Arnold et al., 2006], and the Mimetic Spectral Element Method (MSEM) [Gerritsma, 2012] pursue this goal. They expose the common geometric and topological foundations shared by physical theories and build discretisations that *commute* with fundamental operators. The resulting "mimetic" spaces preserve the integral theorems at the discrete level, yielding stability and consistency by design. Moreover, integral conservation becomes *basis-independent* (polynomial or otherwise), regardless of mesh resolution or curvature.

2.2. ORIENTATION OF ENTITIES

Continuum physics is most naturally described in terms of *global* quantities measured over finite geometric objects, rather than solely in terms of pointwise fields. For instance, Mass, momentum or energy are obtained by integrating densities over volumes, circulation is the integral of a velocity along a path, and fluxes measure how much of a quantity crosses a surface. These global variables attach to geometric objects of increasing dimension (for e.g. OD points, 1D curves, 2D surfaces and 3D volumes) and reflect how measurements are actually made with finite resolution, i.e. discretisation.

Not all global quantities play the same role. One distinguishes *configuration variables* (e.g. displacements or potentials), *source variables* (forces, loads, stresses), and *intermediate variables* (strains, fluxes) that mediate between them [Tonti, 2013]. From these arise three classes of governing relations: definition equations express intermediates as derivatives of configurations (potentials); balance equations encode conservation laws (momenta, energy, helicity, etc.); and constitutive equations tie intermediate quantities together or to the sources via material properties (e.g. stress-strain laws). A point in this construction is that every geometric entity carries an *orientation*, and physical variables must respect this. Two kinds of orientation occur:

1. An *Inner orientation* picks a direction *within* the object. For a curve it selects the "forward" direction; for a surface it determines the cyclic order of its boundary; for a volume it induces orientations on its bounding faces. Quantities like displacements, rotations measured on a surface, or strains along a fibre use inner orientation and do not change sign when the ambient orientation is reversed.

2. An *Outer orientation* orients an object relative to the ambient space-an outward normal on a surface or a choice of "positive" volume. Fluxes, forces and other source variables are outer-oriented, and their signs flip when the orientation of the ambient space is reversed; hence they are sometimes called pseudo-scalars, pseudo-vectors or pseudo-tensors.

Example 2.2.1: Inner-oriented quantities

Temperature or the position of an object's centre of mass are pointwise quantities, strain is associated with a curve, work done is the integral of a force along a path; and the rotation of a solid body can be measured over a surface without reference to an external normal. None of these would change sign if we reverse the orientation of space.

Example 2.2.2: Outer-oriented quantities

Mass flux through a surface, electric charge (as a *source* variable in generating a magnetic field [Tonti, 2000]) or energy contained in a volume, and traction forces on a surface all require an outward normal; reversing that normal reverses the sign of the measurement. Likewise, circulation of a vortex filament in electromagnetism (Biot–Savart law) depends on the chosen direction around the filament.

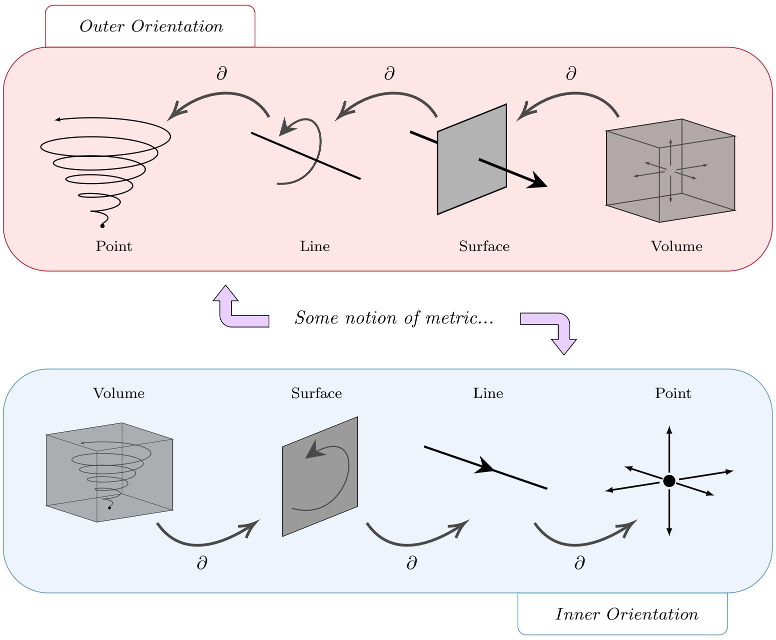

Figure 2.1: The metric connection between orientations, and the topological relation between geometries within an orientation. The ∂ operation refers to the boundary of the geometric object.

This orientation framework distinguishes between *topological* and *constitutive* laws. Balance equations such as conservation of mass or momentum are topological: they depend only on how geometric objects fit together and are entirely metric-free. Constitutive relations, on the other hand, are metric-dependent: they relate variables on *dual* geometric objects (e.g. stress and strain, viewed as inner- and outer-oriented variables) via material parameters, and they rely on notions of length, area, and volume (see Figure 2.1). And thus, there exists a natural emergence of a dual orientation of space-time dependent fields.

Remark 2.2.1

The association of physical quantities with inner or outer orientations is *not* rigid; what matters is that the choice is made consistently throughout the formulation. For instance, in mixed formulations of Stokes flow, velocity may be represented either on curves (inner orientation) or on surfaces (outer orientation). The circulation of a velocity field around a closed surface, for example, represents rotation or vorticity (inner orientation), while the total flux of velocity through a surface or volume represents divergence (outer orientation). In solid or fluid mechanics, displacement plays a role analogous to velocity: it may be integrated along a line in the inner orientation or over a surface in the outer orientation. Interpretations are valid so long as the corresponding balance and constitutive relations respect the induced orientations.

Furthermore, this association is not limited to a single geometric representation. A more general approach-used in most modern formulations assigns each vector component to distinct geometric entities. In $\mathbb{R}^n$, this results in n outer-oriented cell complexes and n corresponding inner-oriented complexes, one per vector component. This leads to a *vector-valued* representation, where each vector component (e.g. u_x and u_y in $\mathbb{R}^2$) is attached to the same point or cell, forming what are called *fibres* of the field. These fibres can also be linked to higher-order quantities such as stress tensors in the elasticity complex, where individual vector (or any geometrical object as a matter of fact, e.g. a tensor) components correspond to fluxes across specific surfaces, i.e. a *multi-linear* map. In this way, the divergence of stress for each component can be evaluated as the sum of fluxes through the associated surfaces, maintaining both geometric consistency and physical interpretability.

The subjects of *differential geometry* and *algebraic topology* together offer a language to connect global, integral descriptions of physical laws with their local, pointwise representations. By emphasizing orientation, connectivity, and the use of discrete cell complexes, they bridge physical measurements with the underlying geometric and topological structure of space, ensuring that both the integral and local perspectives remain consistent. When finite regions are gradually reduced to infinitesimal size, as in classical calculus, this limiting process reveals how changes measured across extended regions become variations described along smaller geometric elements through what differential geometry formalizes as successive differentiation.

In computation, however, these infinitesimals are replaced by finite, discrete elements that partition space and time into a network of a cell complex. A *primal* complex is formed by points, edges, faces, and volumes, while its *dual* counterpart is offset and oriented so that each dual element intersects the corresponding primal element of complementary dimension. Within algebraic topology, these discrete building blocks, i.e. 0-cells, 1-cells, 2-cells, and 3-cells, form the foundation for expressing global variables as combinations of oriented cells (chains) or as numerical values assigned to them (cochains). The relationships between these cells capture how physical quantities associated with boundaries connect to those contained within the enclosed regions, reflecting the same logic as the continuous differential relations but in a fully discrete, algebraic form. From this perspective, one can directly construct an algebraic system suited for computation, while still recovering the continuous behaviour of the fields.

2.3. DIFFERENTIAL GEOMETRY: THE LANGUAGE OF FORMS

This section summarily presents foundational concepts from differential geometry and algebraic topology that serve as the skeleton for mimetic discretisation methods. It begins by defining manifolds and the objects on them, and then introduces differential forms along with their principal operations. Lengthier descriptions are given to connections in continuum mechanics in the following chapter.

2.3.1. DIFFERENTIABLE MANIFOLDS

Definition 1 (Differentiable manifolds)**.** *A k-dimensional manifold comprises a topological space $\mathcal{M}$ along with a countable collection of open subsets $\{U_0, U_1, \ldots\}$ (coordinate charts), whereby each point of $\mathcal{M}$ exists in at least one of these U_i (so that $\mathcal{M} = U_0 \cup U_1 \cup \cdots$). Moreover, there exists bijective coordinate maps $\varphi_{U_i} : U_i \to \mathbb{R}^k$ such that $\varphi_{U_i}(U_i) \in \mathbb{R}^k$ are open and connected.*

A manifold is described as a space where one can *locally* apply calculus in roughly the same manner in Euclidean space. Thus, a manifold motivates the idea of calculating on general coordinate systems, such as considering straight or curved objects like surfaces belonging to $\mathbb{R}^k$. The topological nature of the space $\mathcal{M}$ maintains that there is no natural measure of distances between points, nor a measure of angles on a manifold - i.e. it is a metric-free concept.

2.3.2. OBJECTS ON MANIFOLDS

Definition 2 (Tangent space and tangent bundle)**.** *Let $\mathcal{M} \subset \mathbb{R}^k$ be open and let $P \in \mathcal{M}$. The tangent space to $\mathcal{M}$ at P is the vector space $\mathbb{R}^k$ regarded as vectors based at P; we denote it by $T_P\mathcal{M}$. The tangent bundle of $\mathcal{M}$ is the product $T\mathcal{M} = \mathcal{M} \times \mathbb{R}^k$ whose elements are pairs (P, V) with base point $P \in \mathcal{M}$ and tangent vector $V \in \mathbb{R}^k$ at P. The projection $\pi : T\mathcal{M} \to \mathcal{M}$, $\pi(P, V) = P$, maps a tangent vector to its base point.*

Definition 3 (Tangent vector at a point)**.** *Let P be a point on a k-dimensional manifold $\mathcal{M}$ and let f be a real-valued smooth function defined in a neighbourhood of P. Given a vector $V = (V^1, \ldots, V^k)$ with components expressed in coordinates $\{X^\alpha\}$ at P, the directional derivative of f along V at P is*

$$V_P(f) = \sum_{\alpha=1}^{k} V^\alpha \frac{\partial f}{\partial X^\alpha}\Big|_P \tag{2.5}$$

A tangent vector at P is any linear operator $V_P : C^\infty(\mathcal{M}) \to \mathbb{R}$ that acts on smooth functions and in local coordinates has the form

$$V_P = \sum_{\alpha=1}^{k} V^\alpha \frac{\partial}{\partial X^\alpha}\Big|_P \tag{2.6}$$

Essentially, a tangent vector is a vector equipped with a base point. Once $T_P\mathcal{M}$ is defined, one equips it with coordinates by using the chart coordinates on $\mathcal{M}$ and standard coordinates on $\mathbb{R}^k$. In the case where $\mathcal{M}$ is an open subset of $\mathbb{R}^k$, this is rather trivial: Points of $\mathcal{M}$ are denoted X and coordinate systems are written $\{X^\alpha\}$. The same ideas extend to general manifolds by using local charts (U_i, φ_{U_i}) and transporting the above constructions via the coordinate maps $\varphi_{U_i} : U_i \to \mathbb{R}^k$.

Definition 4 (Cotangent bundle on the dual space)**.** *For a k-dimensional manifold $\mathcal{M}$ and $P \in \mathcal{M}$, the dual space at P is the vector space of all linear functionals on $T_P\mathcal{M}$. Elements of $T_P^*\mathcal{M}$ are covectors (or 1-forms). The disjoint union*

$$T^*\mathcal{M} = \bigsqcup_{P \in \mathcal{M}} T_P^*\mathcal{M} \tag{2.7}$$

is the cotangent bundle, equipped with the projection $\pi : T^*\mathcal{M} \to \mathcal{M}$, $\pi(P,\omega) = P$.

Definition 5 (Dual basis)**.** *The dual basis of* $T^*_P\mathcal{M}$ *is the collection*

$$\{dX^1|_P, \ldots, dX^k|_P\}, \quad \textit{defined by} \quad dX^\alpha\Big(\frac{\partial}{\partial X^\beta}\Big|_P\Big) = \delta^\alpha_\beta \tag{2.8}$$

Every covector $\omega \in T^*_P\mathcal{M}$ *therefore admits a unique expansion*

$$\omega = \sum_{\alpha=1}^{k} \omega_\alpha \, dX^\alpha\Big|_P \tag{2.9}$$

A tangent vector is a *direction with a base point*; a covector is, informally-put, a "measuring stick" that assigns a real number to such a directed object according to some measure. Their interaction is a *duality pairing*

$$\langle \omega, V_P \rangle \; = \; \omega(V_P) \; = \; \sum_{\alpha=1}^{k} \omega_\alpha \, V^\alpha \; \in \mathbb{R} \tag{2.10}$$

that is a scalar that depends only on the geometric objects at P, not on the chosen coordinates. Under a change of chart $X \mapsto \widetilde{X}$, the components V^α transform *contravariantly* (like column vectors), whereas the components ω_α transform *covariantly* (like row vectors), so that their pairing remains invariant.

Remark 2.3.1

In this thesis, contravariant vectors are referred to as "vectors", while covariant ones are referred to as "covectors". Vectors and covectors live in dual spaces attached to the same base point, and their pairing (annihilation) is a *real-valued* number. Because the tangent basis at P is $\{\partial/\partial X^\alpha|_P\}$, the canonical covectors $\{dX^\alpha|_P\}$ form the cotangent basis, often written as $[dX^1, \ldots, dX^k]$. These satisfy the Kronecker delta property above and are the building blocks for general differential 1-forms used throughout calculus on $\mathcal{M}$.

2.3.3. DIFFERENTIAL FORMS

Note that this subsection provides a ***very brief*** *primer into some fundamental operations of differential geometry. For a more thorough and complete explanations, with examples, of the concepts below, the reader is pointed to the following resources [Frankel, 2011] [Palha, 2013]. Nevertheless, emphasis in terms of descriptiveness is given to operations that are crucial to the novelties in this thesis.*

Differential forms provide a unified framework for analysis and integration on n-dimensional manifolds in a *coordinate-free* context, in contrast to multivariable calculus.

Definition 6. *A differential* k*-form on an* n*-dimensional manifold* $\mathcal{M}$ *is a multilinear, antisymmetric map* $\omega \colon V^k \to \mathbb{R}$. *In local coordinates* $(x^1, \ldots, x^n)$*, a* k*-form is written as* $\omega = \sum_{i_1<\cdots<i_k} f_{i_1\ldots i_k}(x)\, dx^{i_1} \wedge \cdots \wedge dx^{i_k}$ *where the functions* $f_{i_1\ldots i_k}$ *are smooth on* $\mathcal{M}$.

FUNDAMENTAL OPERATIONS

Definition 7 (Wedge product)**.** *The wedge product* $\wedge$ *combines differential forms in a multilinear, associative, and distributive manner. If* ω *is a* k*-form and* η *is an* ℓ*-form, then their product* $\omega \wedge \eta$ *is a* $(k+\ell)$*-form and satisfies antisymmetry* $\omega \wedge \eta = (-1)^{k\ell}\, \eta \wedge \omega$.

Definition 8 (Exterior derivative)**.** *The exterior derivative is linear operator that increases the degree of the form defined on a smooth manifold by one, or* $\mathrm{d} \colon \Lambda^k(\mathcal{M}) \to \Lambda^{k+1}(\mathcal{M})$

Remark 2.3.2

The operator d generalises differential operators from vector calculus. In $\mathbb{R}^3$, d for a 0-form represents ∇; for a 1-form, $\nabla\times$ ($Curl$ in $\mathbb{R}^3$ or Rot in $\mathbb{R}^2$); and for a 2-form, $\nabla\cdot$. A fundamental property of the exterior derivative is *nilpotency*: $\mathrm{d} \circ \mathrm{d} = 0$. This is equivalent to vector calculus identities such as $\nabla \times (\nabla f) = 0$ and $\nabla \cdot (\nabla \times A) = 0$.

Definition 9 (Generalised Stokes Theorem)**.** *Integration of an* $(k-1)$*-form* $\omega^{(k-1)}$ *on an* k*-dimensional oriented manifold* $\mathcal{M}$ *is well-defined and coordinate-independent via the generalised Stokes theorem. It relates the boundary of an* k*-dimensional manifold to the exterior derivative:*

$$\int_{\mathcal{M}} \mathrm{d}\omega^{(k-1)} = \int_{\partial\mathcal{M}} \omega^{(k-1)}. \tag{2.11}$$

Remark 2.3.3

Integration can be viewed as a duality pairing between differential forms and geometric objects called *chains*. A k-chain is a formal linear combination of oriented k-dimensional submanifolds (or simplices) with real coefficients. The space of k-chains, denoted $C_k(\mathcal{M})$, forms a vector space where addition and scalar multiplication are defined:

$$c_1 + c_2 = \sum_i a_i \mathcal{M}_i + \sum_j b_j \mathcal{N}_j, \quad \lambda c = \sum_i (\lambda a_i)\mathcal{M}_i. \tag{2.12}$$

Integration then defines a pairing between n-forms and n-chains:

$$\langle \cdot,\cdot \rangle : \Lambda^n(\mathcal{M}) \times C_n(\mathcal{M}) \to \mathbb{R}, \quad \langle \omega^{(n)}, \mathcal{M} \rangle = \int_{\mathcal{M}} \omega^{(n)}, \tag{2.13}$$

which is linear in both arguments.

Definition 10 (Inner product on k-forms)**.** *On an n-dimensional oriented Riemannian manifold $(\mathcal{M}, g)$, the metric g induces a symmetric, bilinear mapping and defines the inner product:*

$$(\cdot,\cdot) \colon \Lambda^k(\mathcal{M}) \times \Lambda^k(\mathcal{M}) \to \Lambda^0(\mathcal{M}). \tag{2.14}$$

For two k-forms $\alpha^{(k)}$ and $\beta^{(k)}$ with coordinate representations $\alpha_{i_1\dots i_k}$ and $\beta_{j_1\dots j_k}$, this inner product is given by contracting with the inverse metric tensor components g^{ij}:

$$\left(\alpha^{(k)}, \beta^{(k)}\right) = g^{i_1 j_1} \cdots g^{i_k j_k} \alpha_{i_1\dots i_k} \beta_{j_1\dots j_k}. \tag{2.15}$$

Definition 11 (Hodge star)**.** *The Hodge star operator $\star \colon \Lambda^k(\mathcal{M}) \to \Lambda^{n-k}(\mathcal{M})$ is the unique linear operator satisfying*

$$\alpha^{(k)} \wedge \star \beta^{(k)} = \left(\alpha^{(k)}, \beta^{(k)}\right) \omega^{(n)}, \tag{2.16}$$

for all $\alpha^{(k)}, \beta^{(k)} \in \Lambda^k(\mathcal{M})$, where $\omega^{(n)}$ is the standard volume form defined as $\omega^{(n)} := \sqrt{|\det(g_{ij})|}\,dx^1 \wedge \cdots \wedge dx^n$.

The Hodge $\star$ satisfies $\star\star\alpha^{(k)} = (-1)^{k(n-k)}\alpha^{(k)}$ and is metric-dependent, unlike the exterior derivative. It encodes the distinction between inner and outer orientations (Figure 2.1), playing a crucial role in mimetic discretisation methods by mapping between configuration and source spaces. The metric dependence of the Hodge star arises explicitly from its fundamental relationship with the inner product structure on differential forms. The explicit appearance of the metric tensor components in Equation (2.15) reveals why the Hodge star operator, which intertwines the inner product with the wedge product, must necessarily depend on the metric.

The volume form $\omega^{(n)}$ itself depends on the metric tensor's components (it involves $\sqrt{\det g}$ in local coordinates, which can be seen as an n-dimensional volume scaling), providing another perspective on the metric dependence appearing in the Hodge Star (note that $\star 1 = \omega^{(n)}$). To facilitate integration over manifolds, a global inner (L^2) product is constructed by integrating the local scalar-valued inner product over the entire manifold. This yields an n-form, which is precisely what can be integrated over the n-dimensional manifold $\mathcal{M}$:

$$\int_{\mathcal{M}} \left(\alpha^{(k)}, \beta^{(k)}\right) \omega^{(n)} = \int_{\mathcal{M}} \alpha^{(k)} \wedge \star \beta^{(k)} = (\alpha^{(k)}, \beta^{(k)})_{L^2(\mathcal{M})}. \tag{2.17}$$

Definition 12 (de Rham complex)**.** *A de Rham complex is a cochain complex of differential forms on a smooth manifold $\mathcal{M}$ related via the exterior derivative. For a smooth n-dimensional manifold $\mathcal{M}$ without boundary, the de Rham complex is*

$$\begin{tikzcd}
\mathbb{R} \arrow[r, tail] & \Lambda^0(\mathcal{M}) \arrow[r, "\mathrm{d}"] & \Lambda^1(\mathcal{M}) \arrow[r, "\mathrm{d}"] & \dots \arrow[r, "\mathrm{d}"] & \Lambda^n(\mathcal{M}) \arrow[r] & 0
\end{tikzcd} \tag{2.18}$$

Remark 2.3.4

For manifolds with boundary, the treatment is more involved as boundary conditions must be incorporated into the dual complex structure. The presentation here restricts to manifolds without boundary for simplicity.

When a metric is associated, a double de Rham complex can be constructed to relate primal and dual orientations via the Hodge star operator. For a smooth manifold $\mathcal{M}$ *without boundary*, the double complex in $\mathbb{R}^3$ takes the form:

$$\begin{tikzcd}
\mathbb{R} \arrow[r, tail] & \Lambda^0(\mathcal{M}) \arrow[r, "\nabla"] \arrow[d, leftrightarrow, "\star"'] & \Lambda^1(\mathcal{M}) \arrow[r, "\nabla\times"] \arrow[d, leftrightarrow, "\star"'] & \Lambda^2(\mathcal{M}) \arrow[r, "\nabla\cdot"] \arrow[d, leftrightarrow, "\star"'] & \Lambda^3(\mathcal{M}) \arrow[r] \arrow[d, leftrightarrow, "\star"'] & 0 \\
0 & \tilde{\Lambda}^3(\mathcal{M}) \arrow[l] & \tilde{\Lambda}^2(\mathcal{M}) \arrow[l, "\nabla\cdot"'] & \tilde{\Lambda}^1(\mathcal{M}) \arrow[l, "\nabla\times"'] & \tilde{\Lambda}^0(\mathcal{M}) \arrow[l, "\nabla"'] & \mathbb{R} \arrow[l, tail]
\end{tikzcd} \tag{2.19}$$

Example 2.3.1

Polynomial basis functions mimic Sobolev spaces in FEEC [Arnold et al., 2010]: In $\mathbb{R}^3$, 0-forms correspond to H^1-conforming elements, 1-forms to $H(\text{curl})$-conforming elements, 2-forms to $H(\text{div})$-conforming elements, and 3-forms to $L^2(\mathcal{M})$. Therefore, the FEEC double complex is

$$\begin{tikzcd}
\mathbb{R} \arrow[r, tail] & H^1(\mathcal{M}) \arrow[r, "\nabla"] \arrow[d, leftrightarrow, "\star"'] & H(\text{curl};\mathcal{M}) \arrow[r, "\nabla\times"] \arrow[d, leftrightarrow, "\star"'] & H(\text{div};\mathcal{M}) \arrow[r, "\nabla\cdot"] \arrow[d, leftrightarrow, "\star"'] & L^2(\mathcal{M}) \arrow[r] \arrow[d, leftrightarrow, "\star"'] & 0 \\
0 & \widetilde{H}^1(\mathcal{M}) \arrow[l] & \widetilde{H}(\text{curl};\mathcal{M}) \arrow[l, "\nabla\cdot"'] & \widetilde{H}(\text{div};\mathcal{M}) \arrow[l, "\nabla\times"'] & L^2(\mathcal{M}) \arrow[l, "\nabla"'] & \mathbb{R} \arrow[l, tail]
\end{tikzcd} \tag{2.20}$$

where the tilde notation $\widetilde{(\square)}$ denotes the dual orientation obtained via the Hodge star.

Remark 2.3.5

Extending the above operators to bundle-valued differential forms allows one to handle objects whose components each behave like forms but collectively transform as sections of a vector bundle. More precisely, such objects have two distinct "legs": a *form leg* (on the base manifold) and a *bundle-value leg*. Operations such as pullback and pushforward (see the following subsection) act only on the form leg, leaving the bundle-value leg untouched. [Kanso et al., 2007]

2.3.4. PULLBACKS OF FORMS

It is important to know how forms transform against one another given a mapping between two manifolds. Such transformations are either convenient, such as in finite element methods where computations may be performed on a reference element; or as part of the description of the kinematic behaviour, as how Hooke's Law requires the notion of comparing deformed media and its undeformed state to compute intrinsic forces. Let us begin by considering a general change of variables. Suppose we are given a transformation between two coordinate systems:

$$\begin{cases} u = u(x,y,v) \\ v = v(x,y,z) \\ w = w(x,y,z) \end{cases} \iff \begin{cases} x = x(u,v,w) \\ y = y(u,v,w) \\ z = z(u,v,w) \end{cases} \tag{2.21}$$

To understand how differential forms transform, consider a 1-form $\lambda^{(1)} = A\,dx + B\,dy + C\,dz$ expressed in (x,y,z) coordinates. When we transform to (u,v,w) coordinates, each differential dx, dy, and dz must be expressed in terms of du, dv, and dw using the chain rule. The complete transformation is given as:

$$\lambda^{(1)} = \left(A\frac{\partial x}{\partial u} + B\frac{\partial y}{\partial u} + C\frac{\partial z}{\partial u}\right)du + \left(A\frac{\partial x}{\partial v} + B\frac{\partial y}{\partial v} + C\frac{\partial z}{\partial v}\right)dv + \left(A\frac{\partial x}{\partial w} + B\frac{\partial y}{\partial w} + C\frac{\partial z}{\partial w}\right)dw. \tag{2.22}$$

The equation (2.22) indicates how coefficients (vector proxies) of a 1-form transform under the mapping $(x,y,z) \to (u,v,w)$. The transformation is governed by the Jacobian matrix of partial derivatives, which encodes how displacements as dual functionals in one coordinate system relate to those in another. Note that the coefficients A, B and C, are generally functions of (x,y,z) also need to be transformed in (u,v,w). While the explicit calculations above provide valuable insight, there exists a more systematic way to describe transformations of differential forms: the *pullback operator*. This operator formalises the idea that a differential form defined on a target manifold can be "pulled back" to the domain manifold via a smooth mapping.

Definition 13 (Pullback operator)**.** *Consider a manifold $\mathcal{M}$ of dimension m, a manifold $\mathcal{N}$ of dimension n, and a smooth mapping between them, $\varphi\colon \mathcal{M} \to \mathcal{N}$, such that local coordinates ξ^i in $\mathcal{M}$ are mapped onto local coordinates $\varphi(\xi^1,\ldots,\xi^m)$ in $\mathcal{N}$. Then the pullback, φ^*, of a k-form $\alpha^{(k)} \in \Lambda^k(\mathcal{N})$ (where $k \le m$) is a mapping: $\varphi^* : \Lambda^k(\mathcal{N}) \to \Lambda^k(\mathcal{M})$ defined by its action on tangent vectors:*

$$\varphi^*(\alpha^{(k)})(\vec{v}_1,\ldots,\vec{v}_k) = \alpha^{(k)}(\varphi_*(\vec{v}_1),\ldots,\varphi_*(\vec{v}_k)) \tag{2.23}$$

where $\varphi_*(\vec{v})$ denotes the pushforward of a vector $\vec{v}$ under the mapping φ. The pushforward is φ_* of a tangent vector $V \in T_p\mathcal{M}$ at point p is the linear map $\varphi_* : T_p\mathcal{M} \to T_{\varphi(p)}\mathcal{N}$, that maps tangent vectors on $\mathcal{M}$ to tangent vectors on $\mathcal{N}$.

In the context of this thesis, the pullback operator is nothing more than a coordinate-free approach to vector calculus' *change of variables*. The pullback operator is related to integration theory through the following formulation:

Definition 14 (Pullback integration)**.** *The integral of a differential k-form $a^{(k)}$ over a k-dimensional manifold $\mathcal{M}$ is defined as:*

$$\int_{\mathcal{M}} a^{(k)} = \int_{\mathcal{N}} \left(\varphi^{-1}\right)^{*} (a^{(k)}) \tag{2.24}$$

where $\varphi^{-1} : N \subset \mathbb{R}^k \to \mathcal{M}$ represents the inverse of the coordinate chart mapping from $\mathcal{M}$ to $\mathcal{N} \subset \mathbb{R}^k$.

This definition makes precise the notion that integration of forms is coordinate-independent. When we integrate over a manifold, we must first parametrise it using local coordinates, which amounts to "pulling back the form to some Euclidean domain where standard integration techniques apply.

Example 2.3.2

Consider the basic 2-form $\omega = dx \wedge dy$ on $\mathbb{R}^2$ and the polar coordinate transformation $\varphi : \mathbb{R}^2 \to \mathbb{R}^2$ given by:

$$\varphi(r,\theta) = (r\cos\theta, r\sin\theta) \tag{2.25}$$

We wish to compute the pullback $\varphi^*(dx \wedge dy)$ and show that it equals $r\,dr \wedge d\theta$. Let us begin by calculating the pullback explicitly. Under the transformation (2.25), we have:

$$\begin{aligned} x &= r\cos\theta \\ y &= r\sin\theta \end{aligned} \tag{2.26}$$

Taking differentials:

$$\begin{aligned} dx &= \cos\theta\,dr - r\sin\theta\,d\theta \\ dy &= \sin\theta\,dr + r\cos\theta\,d\theta \end{aligned} \tag{2.27}$$

Now we compute the pullback of the 2-form:

$$\begin{aligned} \varphi^*(dx \wedge dy) &= (\cos\theta\,dr - r\sin\theta\,d\theta) \wedge (\sin\theta\,dr + r\cos\theta\,d\theta) \\ &= r\cos^2\theta\,dr \wedge d\theta - r\sin^2\theta\,d\theta \wedge dr \\ &= r\cos^2\theta\,dr \wedge d\theta + r\sin^2\theta\,dr \wedge d\theta \\ &= r(\cos^2\theta + \sin^2\theta)\,dr \wedge d\theta \\ &= r\,dr \wedge d\theta \end{aligned} \tag{2.28}$$

We can verify this result by computing the Jacobian determinant of the transformation. The Jacobian matrix is:

$$J_\varphi = \begin{pmatrix} \frac{\partial x}{\partial r} & \frac{\partial x}{\partial \theta} \\ \frac{\partial y}{\partial r} & \frac{\partial y}{\partial \theta} \end{pmatrix} = \begin{pmatrix} \cos\theta & -r\sin\theta \\ \sin\theta & r\cos\theta \end{pmatrix} \tag{2.29}$$

Computing the determinant:

$$\det(J_\varphi) = r\cos^2\theta + r\sin^2\theta = r \tag{2.30}$$

Therefore, we confirm that:

$$\varphi^*(dx \wedge dy) = r\,dr \wedge d\theta = (\det J_\varphi)\,dr \wedge d\theta \tag{2.31}$$

as expected from the well-known change of variables from Cartesian to polar coordinates mapping formula in traditional multivariable vector calculus.

When we consider a mapping φ between manifolds and ask how integration behaves under this mapping, we obtain a fundamental relationship that captures the essence of the pullback operation. Specifically, if we integrate a form over the image $\varphi(\mathcal{M})$, this is equivalent to integrating the pulled-back form over the original domain $\mathcal{M}$:

$$\int_{\varphi(\mathcal{M})} a^{(k)} = \int_{\mathcal{M}} \varphi^* a^{(k)} \iff \langle a^{(k)}, \varphi(\mathcal{M})\rangle = \langle \varphi^* a^{(k)}, \mathcal{M}\rangle. \tag{2.32}$$

Remark 2.3.6

The pullback operator possesses several fundamental properties that make it an indispensable tool in geometry:

$$\varphi^*(a^{(k)} + b^{(l)}) = \varphi^*(a^{(k)}) + \varphi^*(b^{(l)}) \quad \text{(Linearity)} \tag{2.33}$$

$$\varphi^*(a^{(k)} \wedge b^{(l)}) = \varphi^*(a^{(k)}) \wedge \varphi^*(b^{(l)}) \quad \text{(Algebra homomorphism)} \tag{2.34}$$

$$(\varphi_2 \circ \varphi_1)^* = \varphi_1^* \circ \varphi_2^* \quad \text{(Composition)} \tag{2.35}$$

Properties (2.34) and (2.35) demonstrate that the wedge product is a canonical, coordinate-independent operation. The preservation of the wedge product under pullback (2.34) ensures that geometric relationships encoded in the exterior algebra are maintained under coordinate transformations. The composition property (2.35) shows that pullbacks compose in the "opposite" direction to mappings, which is characteristic of contravariant functors. Most importantly for our purposes, the pullback operator commutes with the exterior derivative: $\varphi^*\left(da^{(k)}\right) = d\left(\varphi^* a^{(k)}\right)$. The commutation property is essential as it establishes that the exterior derivative is a coordinate-free, intrinsic geometric operation. Regardless of how we transform our manifold, the fundamental differential relationships captured by d remain unchanged.

2.3.5. TREATING BUNDLE-VALUED FORMS

When discretizing PDEs, it is useful to consider not just scalar-valued differential forms but also vector-valued forms. If ω is a k-form on $\mathcal{M}$ and $\mathcal{E}$ is a vector bundle over $\mathcal{M}$, then an $\mathcal{E}$-valued k-form is a multilinear, antisymmetric map that assigns to each k-tuple of tangent vectors an element of the fibre $\mathcal{E}_p$, which is useful for the representation of physical quantities such as displacement fields, stress tensors in terms of differential geometry. The theory of fibre bundles comes essential for defining such mathematical objects. A *fibre bundle* is a space that locally resembles a product space but may have a different global topological structure. The relationship is encoded through a continuous, surjective map $\pi : \mathcal{E} \to \mathcal{M}$, called the *projection*, where $\mathcal{M}$ is the *base space* and the fibres are the preimages $\pi^{-1}(p)$ for $p \in \mathcal{M}$. A *section* of $\mathcal{E}$ is a map from the base space to $\mathcal{E}$ that assigns one element from each fibre, satisfying $\pi \circ s = \mathrm{Id}_{\mathcal{M}}$.

From a global perspective, one collects all tangent spaces $T_p\mathcal{M}$ into the *tangent bundle* $T\mathcal{M}$, and all cotangent spaces $T_p^*\mathcal{M}$ into the *cotangent bundle* $T^*\mathcal{M}$. A *vector bundle* is, in general, any smooth family of vector spaces (one for each point $p \in \mathcal{M}$) that "fit together" over $\mathcal{M}$. A section of a vector bundle picks out one vector from each fibre, so a classical vector field on $\mathcal{M}$ is precisely a section of $T\mathcal{M}$.

Example 2.3.3

In two-dimensional Cartesian space, any vector or covector-valued physical quantity has two components (one in the x-direction and another in the y-direction). Instead of treating these as separate scalar fields, a bundle-valued form stores both components together as a single mathematical entity, reflecting the intrinsic geometry. When discretising vector or covector fields in finite element methods one often places degrees of freedom on k-cells. Treating the field as a bundle-valued form naturally associates all vector components to the same mesh elements, simplifying both the assembly of system matrices and the enforcement of PDE constraints or boundary conditions.

Remark 2.3.7

In the case of a flat ambient space with no curvature, one has a one-to-one relation among all the tangent spaces of $\mathcal{M}$. The same also holds for the tangent spaces of $\mathcal{M}$ itself. A consequence of that is one can identify all the tangent spaces by a unique vector space making the vector bundles trivial. As a consequence, one can then consider differential forms with values in this single vector space, i.e. *unique* and *trivial*. However, doing so requires incorporating these maps between the different tangent spaces in the formulation, which could be complicated for curvilinear coordinates - which could be alleviated by using the more generic vector bundle structure. This thesis makes use of such *trivial* fibre bundles, i.e. a rank n vector bundle is trivial if and only if it has n linearly independent global sections [Rashad et al., 2023]. In the trivial case, the total space is isomorphic to the product of the base space and the fibre, and the projection is just the projection onto the first factor.

From the above remark in the trivialisation of $\mathcal{E}$, one can also define the previous metric-free differential geometry operations for vector-valued forms as a bundle. More specifically, by considering the fibre bundle as a set whose fibres represent smooth, linear maps that correspond to their scalar analogues. For the pullback operation this is given below, but it can be shown for the wedge product, as a tensorial Kronecker product $\otimes$ of forms; and the exterior derivative, but acting component-wise relative to any basis of the vector space.

Definition 15 (Pullback bundle)**.** *A pullback bundle or induced bundle is the fibre bundle that is induced by a map of its base space. Given a fibre bundle $\pi : \mathcal{E} \to \mathcal{M}$ and a continuous map $f : \mathcal{M} \to \mathcal{M}$, one can define a “pullback” of $\mathcal{E}$ by f as a bundle $f^*\mathcal{E}$ over $\mathcal{M}$. The fibre of $f^*\mathcal{E}$ over a point $p \in \mathcal{M}$ is just the fibre of $\mathcal{E}$ over $f(p)$. Thus $f^*\mathcal{E}$ is the disjoint union of all these fibres equipped with a suitable topology.*

Definition 16 (Pullback of vector-valued forms)**.** *The pullback of an $\mathcal{E}$-valued form on $\mathcal{M}$ by a smooth map $\varphi : \mathcal{M} \to \mathcal{M}$ is an $(\varphi^*\mathcal{E})$-valued form on $\mathcal{M}$, where $\varphi^*\mathcal{E}$ is the pullback bundle of $\mathcal{E}$ by φ. The formula is given just as in the ordinary* *case. For any* $\mathcal{E}$*-valued* p*-form* ω *on* $\mathcal{M}$*, the pullback* $\varphi^*\omega$ *is given by*

$$(\varphi^*\omega)_x(v_1,\dots,v_p) = \omega_{\varphi(x)}(\varphi_*(v_1),\dots,\varphi_*(v_p)) \tag{2.36}$$

where $x \in \mathcal{M}$ *and* $v_1,\dots,v_p \in T_x\mathcal{M}$*.*

Although the above 2.36 is draws similarities to the scalar-valued case 2.23 the operation here is more involved. In the context of bundle-valued forms, one could essentially pull back the form component (leaving the fibres untouched), pull back the fibre values (leaving the form component untouched), or perform both operations. The definition above corresponds to the first case: the action on the tangent vectors is handled by the pushforward φ_*, effectively pulling back the form component, while the fibre values are simply re-indexed to the pullback bundle $\varphi^*\mathcal{E}$.

2.4. ALGEBRAIC TOPOLOGY: TO DISCRETE COMPUTATION

The framework of differential geometry provides powerful tools for expressing physical laws in a coordinate-independent manner on smooth manifolds. In moving from continuous theory to practical numerical computations, we must discretise the underlying geometric structures. Algebraic topology provides the mathematical language for rigorously describing discrete approximations of continuous geometric objects while preserving their fundamental topological and algebraic properties. This section is purely meant to summarise the fact that the subject, in the context of MSEM is a discrete perspective of differential geometry. The reader is pointed to the following resources for a more rigourous set of definitions [Gerritsma, 2012] [Hatcher, 2002] [Arnold et al., 2010] [Hyman and Scovel, 2005].

The idea in using algebraic topological concepts is to partition differentiable manifolds into a collection of non-overlapping subspaces called *cells*, such that their union reconstructs the entire manifold under study. This partitioning yields a discrete representation of the manifold in terms of a finite number of simple building blocks: points (0-cells), line segments (1-cells), surface patches (2-cells), volumetric regions (3-cells), and their higher-dimensional analogues. A formal weighted sum of k-cells within such a partition is called a k*-chain*, and these chains serve as the discrete analogues of the geometric domains over which we integrate differential forms.

Several fundamental structures emerge from this cellular decomposition, but in MSEM there is a particular emphasis on quadrilaterals and their generalizations to higher dimensions (singular k-cubes) [Palha et al., 2014]. The algebraic topology framework also introduces the notion of *duality*: one can define objects dual to the original cells and construct a dual partition, known as the *dual complex*. Associated with these cellular structures is the *boundary operator*, which acts on chains to extract their boundaries. This operator serves as the dual to the coboundary operator, i.e. the discrete counterpart to the exterior derivative in differential geometry. These dual entities and operators play a key role in the discretisation of physical quantities, particularly in distinguishing between configuration and source variables as discussed earlier.

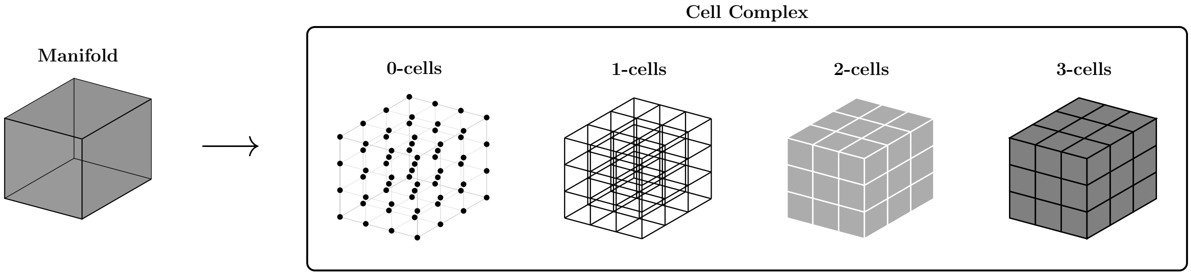

Figure 2.2: Sample $\mathbb{R}^3$ cell complex partitioned into a collection of points, lines segments, surfaces and volumes (k-cells). The union of all the cells tiles the manifold with compatible orientations [Palha, 2013]

After having defined a discrete representation of the manifold in terms of k-chains, we can assign values to the various spatial elements by defining the dual space of the chains, called the space of k*-cochains*. The duality pairing between chains and cochains provides a natural way to introduce discrete operations on cochains as formal adjoints of operations on chains. In this manner, operations on k-cochains naturally mimic the operations on k-forms discussed in the context of differential geometry. This is the foundation upon which mimetic discretisation methods are built, such that discrete analogues of differential operators preserve properties such as nilpotency of the exterior derivative and the structure of de Rham complexes, i.e. continuous physical laws [Frankel, 2011].

Remark 2.4.1

Throughout this thesis, it is assumed that the dimension of all manifolds is *finite*, i.e. $\dim(\mathcal{M}) = n$.

INCIDENCE MATRICES

While we do not extensively go through the definition used from algebraic topology [Hatcher, 2002], a notable one is outlined here for its emphasis in MSEM. On a cell complex, the continuous exterior derivative d is represented discretely by *incidence matrices*. These matrices represent the oriented adjacency between k-cells and $(k+1)$-cells, i.e. the discrete boundary operator.

Definition 17 (Incidence matrix)**.** *Let C_k be the vector space spanned by oriented k-cells of a finite cell complex. The boundary operator $\partial_{k+1} : C_{k+1} \to C_k$ maps each oriented $(k+1)$-cell to a formal sum of its oriented boundary k-cells. The matrix representation of ∂_{k+1} with respect to a chosen ordering of cells yields the incidence matrix $\mathbb{E}^{(k+1,k)} \in \mathbb{R}^{(N_{k+1}\times N_k)}$, where N_k denotes the number of k-cells. Its entries are*

$$\mathbb{E}^{(k+1,k)}_{ij} = \begin{cases} +1, & \textit{if the } j\textit{-th } k\textit{-cell is a face of the } i\textit{-th } (k+1)\textit{-cell with the same orientation} \\ -1, & \textit{if it is a face with opposite orientation} \\ 0, & \textit{else} \end{cases} \tag{2.37}$$

This incidence matrix acts on discrete k-cochains (lists of integral values on k-cells) to produce discrete $(k+1)$-cochains, mimicking the exterior derivative. This corresponds to the **coboundary operator** δ, which is the discrete analogue of the exterior derivative. It is related to the boundary operator ∂ by the discrete analogue of Stokes theorem:

$$\langle \alpha^{(k)}, \partial_{k+1} c_{k+1} \rangle = \langle \delta_k \alpha^{(k)}, c_{k+1} \rangle. \tag{2.38}$$

The topological identity that "the boundary of a boundary is zero" implies $\delta \circ \delta = 0$, captured by the algebraic relation $\mathbb{E}^{(k+2,k+1)}\mathbb{E}^{(k+1,k)} = 0$, $\forall k$ which encodes discrete versions of $\nabla \times (\nabla\varphi) = 0$ and $\nabla \cdot (\nabla \times \mathbf{u}) = 0$.

2.5. MIMETIC SPECTRAL DISCRETISATION

In MSEM, a domain $\Omega \in \mathbb{R}^d$ is discretised into a mesh subdivided into primal cells (representing the physical geometry) and dual cells. In $\mathbb{R}^2$, the primal mesh has points, lines, and surfaces corresponding to 0-, 1- and 2-cells. The dual mesh interchanges these roles so that each primal k-cell corresponds to a dual $(d-k)$-cell. Degrees of freedom for scalar fields (0-forms) live in primal vertices, while integral values of vector fields (1-forms) live along edges and fluxes of 2-forms live on faces. Dual degrees of freedom correspondingly live on dual cells [Gerritsma, 2012].

Definition 18 (Reduction operator)**.** *For each degree $p \in \{0,\dots,d\}$ let $\{C^{(p)}_i\}$ denote the oriented p-cells of the mesh. The* reduction operator *R maps a smooth p-form $\alpha^{(p)} \in \Omega$ to a p-cochain through $(R\,\alpha^{(p)})_i = \int_{C^{(p)}_i} \alpha^{(p)}$, assigning to each p-cell the integral of the form over that cell. It satisfies the commutation property $R\,\mathrm{d} = \delta R$, where δ is the discrete coboundary represented by incidence matrices.*

Definition 19 (Reconstruction operator)**.** *Let $\{\phi^{(p)}_i\}$ be a chosen basis for discrete p-forms. The* reconstruction operator *I takes a p-cochain $c = (c_i)$ to an approximate p-form by $I(c) = \sum_i c_i\,\phi^{(p)}_i$. It is a left inverse of R in the sense that $R \circ I = \mathrm{Identity}$ on p-cochains, and to ensure compatibility with differentiation it is required that $d\,I = I\,\delta$. Together these properties imply that $I \circ R$ approximates the identity on sufficiently smooth forms.*

2.5.1. MIMETIC BASIS FUNCTIONS

Tensor-product Gauss-Lobatto-Legendre (GLL) nodes $\{\xi_0,\dots,\xi_N\} \in [-1,1]$ serve as collocation (integration) points for the spectral elements in this thesis. These are used to construct the scalar and vector form bases: nodal and edge bases, respectively.

Definition 20 (Nodal basis)**.** *The nodal (Lagrange) basis functions $h_i(\xi)$, $i = 0,\dots,N$, are the unique polynomials of degree N satisfying $h_i(\xi_j) = \delta_{ij}$. They can be written explicitly as*

$$h_i(\xi) = \prod_{\substack{0\le j\le N \\ j\ne i}} \frac{\xi-\xi_j}{\xi_i-\xi_j} \tag{2.39}$$

and reconstruct a scalar field from its nodal values Φ_i via $\Phi_h(\xi) = \sum_{i=0}^{N} \Phi_i h_i(\xi)$, where Φ_i denote 0-form degrees of freedom.

Definition 21 (Edge basis)**.** *The edge basis functions $e_i(\xi)$, $i = 1,\dots,N$, represent line-integral quantities and satisfy $\int_{\xi_{j-1}}^{\xi_j} e_i(\xi)\,d\xi = \delta_{ij}$. They are constructed from the nodal polynomials as,*

$$e_i(\xi) = -\sum_{k=0}^{i-1} \frac{dh_k}{d\xi} \tag{2.40}$$

yielding polynomials of degree $(N-1)$ associated with 1-form degrees of freedom [Gerritsma, 2011].

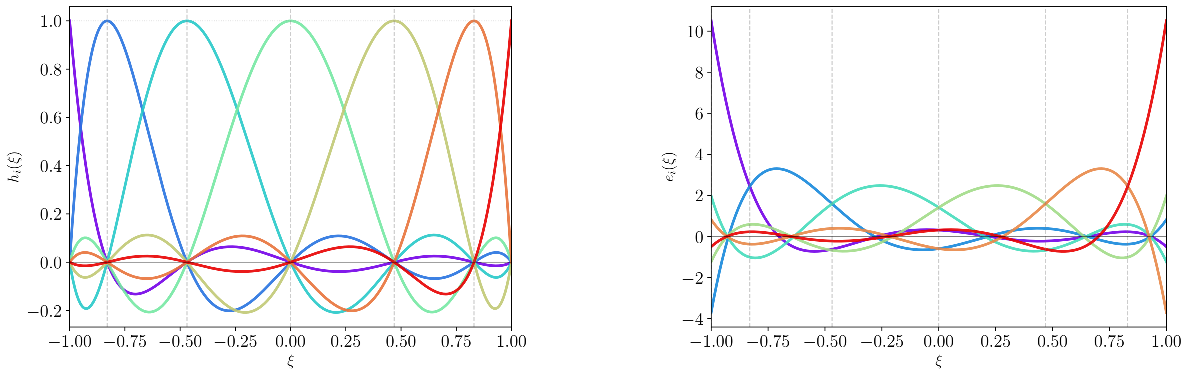

(a) Nodal polynomial basis

(b) Edge polynomial basis

Figure 2.3: 1D basis functions for $N = 6$

2.5.2. MULTI-DIMENSIONAL BASES

These one-dimensional bases can be used as building blocks when extend to higher dimensions by a tensor product. In d dimensions a k-form basis is built by selecting k factors of edge polynomials and $(d-k)$ factors of nodal polynomials. In any case, these tensor-product bases maintain the pointwise and integral Kronecker delta properties from their 1D building blocks, such that the expansion coefficients represent nodal values, edge fluxes, face fluxes, or volume integrals. Hence, the discrete degrees of freedom match physical quantities, making this construction mimetic, or compatible.

Example 2.5.1

For instance, a discrete 0-form in 2D has one component

$$\Psi_h^{(0)}(\xi,\eta) = \sum_{i=0}^{N}\sum_{j=0}^{N} \Gamma_{i,j}\,[h_i(\xi) \otimes h_j(\eta)] \tag{2.41}$$

A discrete 1-form in 2D has two components

$$\Psi_h^{(1,\xi)}(\xi,\eta) = \sum_{i=1}^{N}\sum_{j=0}^{N} \Psi_{i,j}^{(\xi)}\,[e_i(\xi) \otimes h_j(\eta)] \tag{2.42}$$

$$\Psi_h^{(1,\eta)}(\xi,\eta) = \sum_{i=0}^{N}\sum_{j=1}^{N} \Psi_{i,j}^{(\eta)}\,[h_i(\xi) \otimes e_j(\eta)] \tag{2.43}$$

Each coefficient represents the integral of the field along the corresponding mesh edge.

2.5.3. DISCRETE HODGE

The Hodge $\star$ operator on a Riemannian manifold relates k-forms to $(n-k)$-forms by combining metric and orientation. In the discrete setting, a weighted mass matrix $\mathbb{M}^{(k)}$ plays the role of the Hodge star applied to degrees of freedom.

Definition 22 (Discrete Hodge operator). *Let* $\{\psi_i^{(k)}\}_i$ *be a basis for discrete* k*-forms and* $\{\widetilde{\psi}_j^{(n-k)}\}_j$ *its dual basis defined via inversion of the mass matrix. The discrete Hodge operator* $\star_h$ *is the mapping on cochains given by*

$$\star_h : \alpha_h^{(k)} = \sum_i \alpha_i \psi_i^{(k)} \longmapsto \beta_h^{(n-k)} = \sum_j \beta_j \widetilde{\psi}_j^{(n-k)} \tag{2.44}$$

where the cochain components satisfy $\beta = \mathbb{M}^{(k)}\alpha$ *with* $\mathbb{M}_{ij}^{(k)} = \int_\Omega \psi_i^{(k)} \wedge \star\psi_j^{(k)}$*, and* $\tilde{\psi} = \psi\mathbb{M}^{-1}$*.*

The discrete Hodge is metric-dependent and changes both the degree and orientation type of a cochain, and they are generally built from the polynomial bases as seen before. These matrices map coefficients of inner-oriented discrete k-cochains to coefficients of outer-oriented $(n-k)$-cochains via $\hat{\beta}_h = \mathbb{H}^{(k)}\hat{\alpha}_h$, generalising $\beta = \mathbb{M}^{(k)}\alpha$. In mimetic spectral element methods the weighting w is often chosen so that $\mathbb{H}^{(k)}$ coincides with the mass matrix, but the flexibility to incorporate material or geometric factors is one of the strengths of the discrete Hodge operator. Using the discrete Hodge, one may formulate discrete weak forms of partial differential equations (note that this is not strictly defined to be a Galerkin projection). Given a linear, first-order differential operator L acting on a $k-1$-form $\omega^{(k-1)}$, the weak form seeks $\omega_h^{(k)}$ in a finite space such that

$$\int_\Omega L\left[\omega_h^{(k-1)}\right] \wedge \star_h \beta_h^{(k)} = 0, \quad \forall \text{ test } k\text{-forms } \beta_h^{(k)} \tag{2.45}$$

Substituting expansions in primal and dual bases and assembling the resulting integrals leads to algebraic systems involving incidence matrices and weighted mass matrices.

2.5.4. DUAL BASIS FUNCTIONS

In mimetic and spectral element formulations, constructing *dual basis functions* is essential for defining discrete *dual* operators. While primal bases $\Psi^{(k)}$ represent k-forms on the primal grid, their dual counterparts $\widetilde{\Psi}^{(n-k)}$ are defined such that they are bi-orthogonal to the primal basis with respect to the L^2 inner product. This bi-orthogonality is achieved through a transformation involving the mass matrix, via the discrete Hodge operator [Jain et al., 2020b].

Definition 23 (Dual basis transform)**.** *Given a primal basis* $\Psi^{(k)}$*, the corresponding dual basis is obtained as* $\widetilde{\Psi}^{(n-k)} = \Psi^{(k)}[\mathbb{M}^{(k)}]^{-1}$*, where* $\mathbb{M}^{(k)}$ *denotes the* k*-form mass matrix, defined through the* L^2 *inner product* $\mathbb{M}_{ij}^{(k)} = \int_\Omega \Psi_i^{(k)} \wedge \star \Psi_j^{(k)}$.

The *dual nodal basis functions* $\widetilde{h}_i(\xi)$ are associated with the nodes of the dual grid and are dual to the primal edge functions $e_i(\xi)$ defined on the edges of the primal grid. In one dimension, these functions are related through $\widetilde{h}(\xi) = e(\xi)[\mathbb{M}^{(1)}]^{-1}$, where the edge-based mass matrix is given by

$$\mathbb{M}_{ij}^{(1)} = \int_{\xi_{i-1}}^{\xi_i} e_i(\xi) e_j(\xi)\, d\xi, \qquad i = 1, 2, \ldots, N \tag{2.46}$$

Similarly, the *dual edge basis functions* $\widetilde{e}_i(\xi)$ are defined on the edges of the dual grid and are dual to the primal nodal functions $h_i(\xi)$. They are expressed as $\widetilde{e}(\xi) = h(\xi)[\mathbb{M}^{(0)}]^{-1}$, with the nodal mass matrix defined by

$$\mathbb{M}_{ij}^{(0)} = \int_{\xi_{i-1}}^{\xi_i} h_i(\xi) h_j(\xi)\, d\xi, \qquad i = 0, 1, \ldots, N \tag{2.47}$$

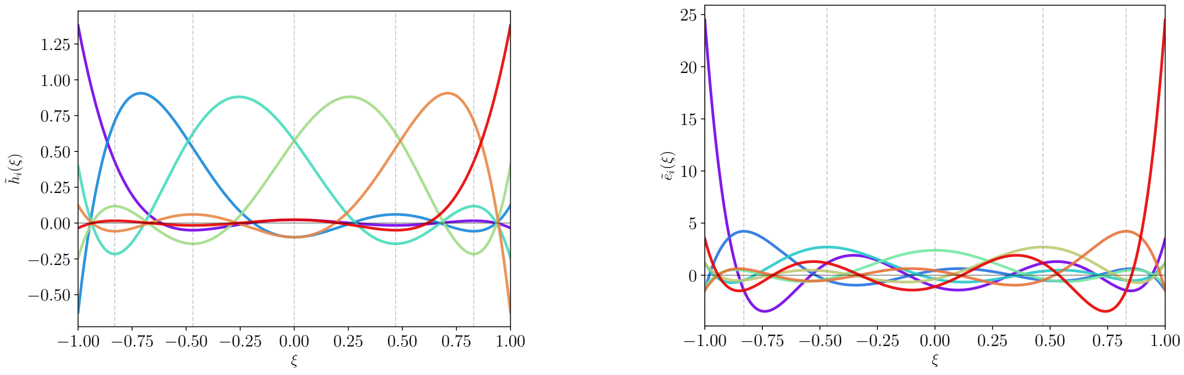

(a) Dual nodal polynomial basis

(b) Dual edge polynomial basis

Figure 2.5: Dual of the 1D basis functions for $N = 6$. Note that we utilise the notation $\widetilde{\square}$ to indicate functions in the dual space

Remark 2.5.1

The above dual bases are unweighted. However in this work, the introduction of discrete pushforward and pullback maps introduce a weighting on the basis functions. To see how such *weighted* dual basis functions are drawn up, refer to Section 4.5.

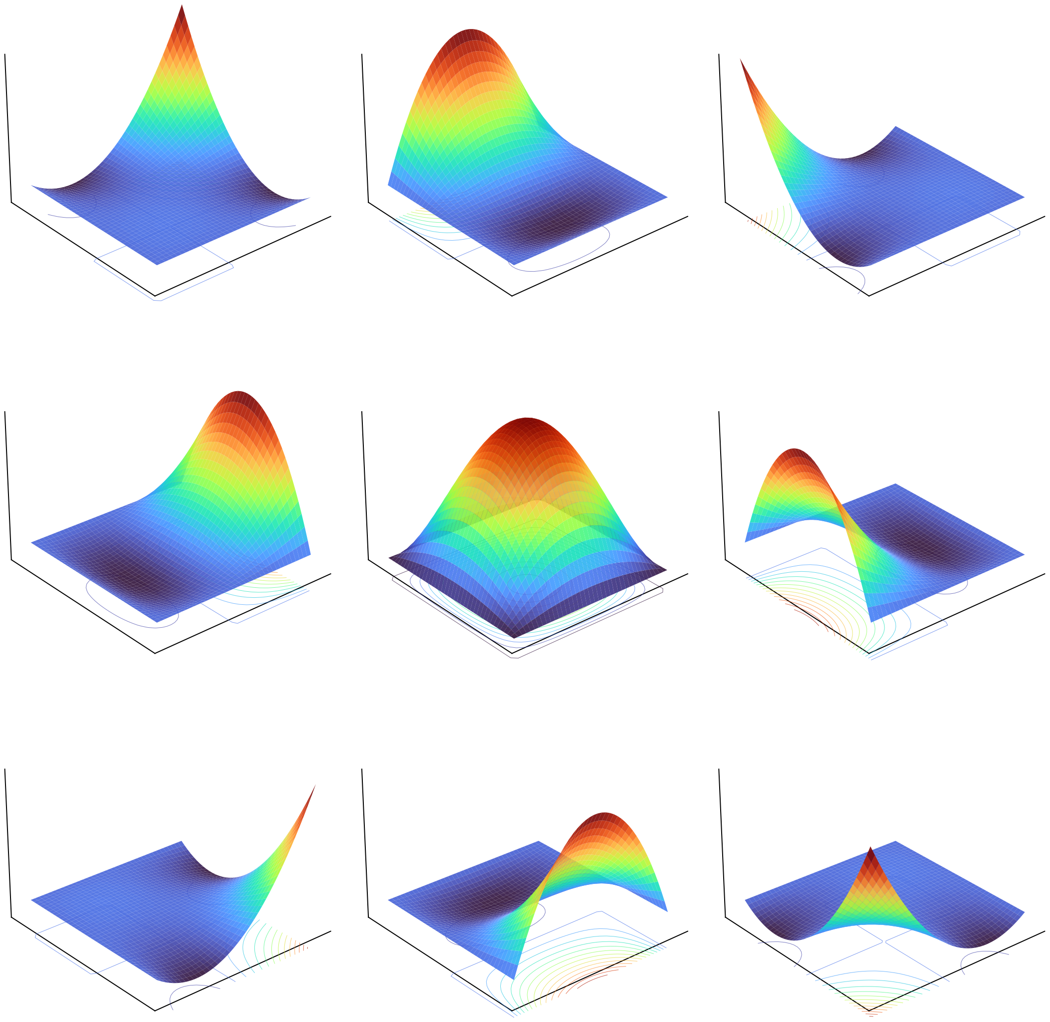

(a) 0-form basis from (2.41)

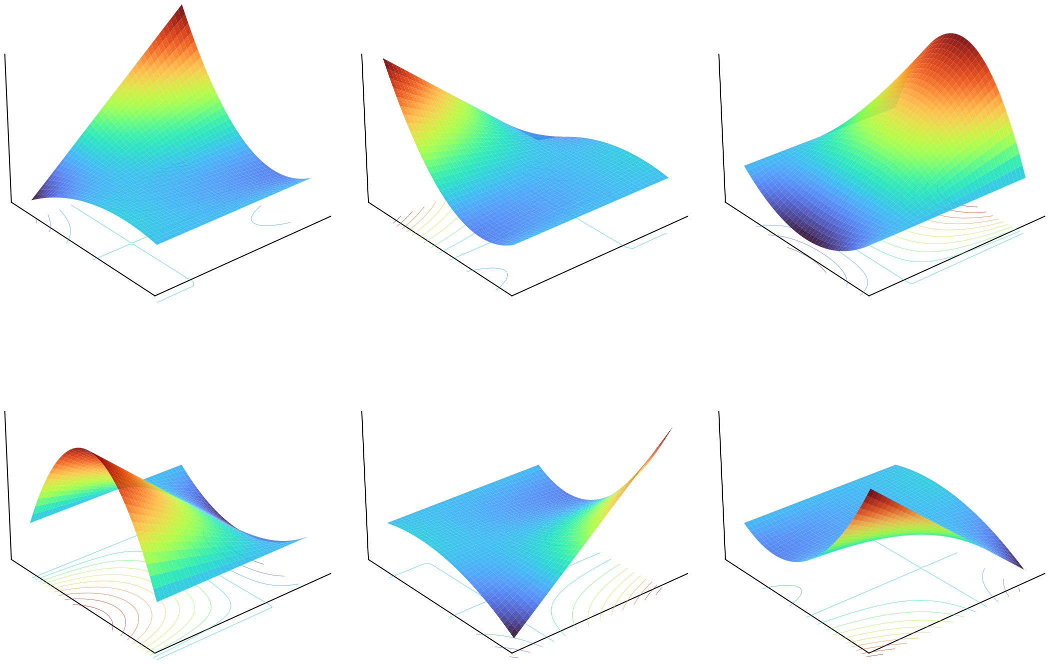

(b) 1-form basis from (2.42)

Figure 2.4: Sample 2D tensor-product basis functions for $N = 2$

3

CONTINUUM MECHANICS FORMULATION

This chapter establishes the continuum mechanics framework for non-linear hyperelasticity, emphasizing connections to differential geometry developed in Section 2.3. We adopt a Lagrangian description wherein material points are tracked from a reference configuration through their deformation in space and time. The presentation follows the geometric viewpoint of Marsden & Hughes [Marsden et al., 1984], recognising configurations as smooth manifolds and deformation as smooth mappings (flowmap) that induce natural transformations of geometric and physical quantities. An introduction to motion and configurations in given in Section 3.1, followed by the various variables used in their definitions (Sections 3.2 and 3.3). Rationale for finite-strain, hyperelasticity formulations are given in Section 3.4. Lastly, *one* interpretation on the geometry of elasticity is given in Section 3.5, with the continuous Lagrangian equation in Section 3.6.

3.1. CONFIGURATIONS AND KINEMATICS

First it its important to discuss how to generally describe bodies undergoing some motion such that induced (finite) strains and/or rotations are also large enough to invalidate assumptions inherent in linear strain theory. In such a case, the undeformed and deformed configurations of the continuum are quite different.

3.1.1. MATERIAL AND SPATIAL DESCRIPTIONS

Consider a continuum body $\mathcal{B}$ undergoing deformation in three-dimensional Euclidean space $\mathbb{R}^3$. Unlike discrete mechanical systems, continuum bodies consist of a continuous distribution of matter, requiring a careful mathematical description of how material points move through space and how their relative positions change under deformation [Reddy, 2013].

Definition 24 (Configurations)**.** *A continuum body $\mathcal{B}$ occupies different regions in $\mathbb{R}^3$ as it deforms over time. The* ***reference configuration*** *$\Omega_0 \subset \mathbb{R}^3$ is a fixed, known domain serving as the baseline for measuring deformation, where each material point (particle) is identified by its position $\mathbf{X} \in \Omega_0$. The* ***current configuration*** *(or deformed configuration) $\Omega_t \subset \mathbb{R}^3$ is the region occupied by the body at time t, where the material point originally at $\mathbf{X}$ is now located at spatial position $\mathbf{x} \in \Omega_t$.*

The distinction between material coordinates $\mathbf{X}$ and spatial coordinates $\mathbf{x}$ is fundamental. Material coordinates serve as time-independent labels identifying which particle we are tracking, analogous to names for individuals. Spatial coordinates identify where in space we are observing at a given instant. This dual description gives rise to two complementary viewpoints: the Lagrangian (material) description expresses field quantities as $\phi(\mathbf{X},t)$, following specific material particles through their motion, where the material time derivative $\dot{\phi} = \partial\phi/\partial t|_{\mathbf{X}}$ measures the rate of change experienced by a particle; while the Eulerian (spatial) description expresses field quantities as $\Pi(\mathbf{x},t)$, observing what happens at fixed spatial locations, where the material time derivative requires the chain rule $d\phi/dt = \partial\phi/\partial t|_{\mathbf{x}} + \mathbf{v}\cdot\nabla\phi$ to account for both local changes and convection. For solid mechanics, the Lagrangian description is preferred because material points undergo bounded displacements, boundary conditions are naturally specified on material surfaces, and constitutive models relate stress to material strain measures [Zienkiewicz et al., 2006].

3.1.2. FLOWMAP: MATERIAL COORDINATES

Definition 25 (Flowmap)**.** *The motion of the body is described by a smooth, invertible mapping $\boldsymbol{\varphi} : \Omega_0 \times [0,T] \to \mathbb{R}^3$ with $\mathbf{x} = \boldsymbol{\varphi}(\mathbf{X},t)$, assigning to each material point $\mathbf{X}$ and time t its current spatial position $\mathbf{x}$. The mapping must satisfy smoothness ($\boldsymbol{\varphi} \in C^2(\Omega_0 \times [0,T])$ at least), invertibility ($\boldsymbol{\varphi}(\cdot,t) : \Omega_0 \to \Omega_t$ is bijective for each t), and orientation preservation ($\det(\nabla_0\boldsymbol{\varphi}) > 0$ everywhere).*

The initial condition typically specifies $\boldsymbol{\varphi}(\mathbf{X},0)=\mathbf{X}$ when the current configuration and an **initial configuration** Ω_{t_0} coincide. When the current configuration and initial configuration do not coincide, the initial condition is instead specified by $\boldsymbol{\varphi}(\mathbf{X},t_0)=\boldsymbol{\varphi}_0(\mathbf{X})$, where $\boldsymbol{\varphi}_0$ is a known mapping from the reference configuration to an arbitrary initial configuration at time $t_0>0$. The displacement field $\mathbf{u}(\mathbf{X},t)=\boldsymbol{\varphi}(\mathbf{X},t)-\mathbf{X}$ measures how far each particle has moved from its reference position. This is illustrated in Figure 3.1. For a fixed particle $\mathbf{X}$, the trajectory $t\mapsto\boldsymbol{\varphi}(\mathbf{X},t)$ traces its path through space, with velocity and acceleration obtained by differentiation: $\mathbf{v}(\mathbf{X},t)=\partial\boldsymbol{\varphi}/\partial t|_{\mathbf{X}}=\dot{\boldsymbol{\varphi}}$ and $\mathbf{a}(\mathbf{X},t)=\partial^2\boldsymbol{\varphi}/\partial t^2|_{\mathbf{X}}=\ddot{\boldsymbol{\varphi}}$.

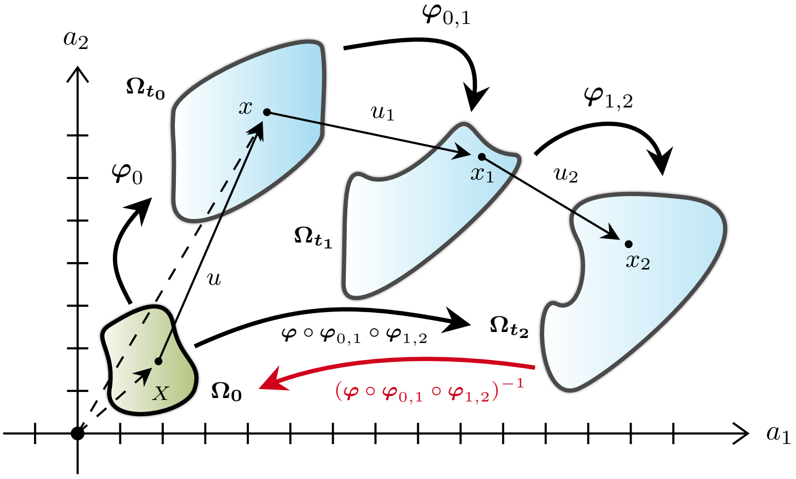

Figure 3.1: Sketch of the relation between different material configurations, such as in a reference, initial, and current state, for a body $\mathcal{B}$ (i.e. they can be used for maps in space and/or time). The flowmap $\boldsymbol{\varphi}$ accordingly acts to form a sequence map, as well as an associated inverse. A displacement can also be used to describe differences in the maps.

3.1.3. DEFORMATION GRADIENT

Definition 26 (Deformation gradient)**.** *The deformation gradient tensor quantifies local deformation:* $\boldsymbol{F}(\mathbf{X},t)=\nabla_0\boldsymbol{\varphi}=\partial\boldsymbol{\varphi}/\partial\mathbf{X}$*, with components* $F_{iI}=\partial x_i/\partial X_I$ *(spatial index* i*, material index* I*). Equivalently,* $\boldsymbol{F}=\mathbf{I}+\nabla_0\mathbf{u}$.

The deformation gradient is a two-point tensor, mapping material tangent covectors to spatial tangent covectors via $d\mathbf{x}=\boldsymbol{F}\cdot d\mathbf{X}$. This relation states that if two material points are initially separated by a covector $d\mathbf{X}$, after deformation they are separated by $d\mathbf{x}=\boldsymbol{F}\cdot d\mathbf{X}$. The deformation gradient thus encodes local stretching, rotation, and shearing of material line elements. The Jacobian determinant $J=\det\boldsymbol{F}$ relates volume elements via $dV=J\,dV_0$, and the condition $J>0$ ensures orientation preservation, preventing self-intersections or volume collapse. Mass conservation for a material element gives $\rho_0\,dV_0=\rho\,dV$, implying $\rho=\rho_0/J$, where $\rho_0(\mathbf{X})$ is the reference density and $\rho(\mathbf{x},t)$ is the current density.

Remark 3.1.1

When the physical domain differs from the computational reference domain (e.g., Cook's membrane geometry versus the reference square $[-1,1]^2$), an additional geometric transformation is required. The stress tensor $\mathbf{P}_{\Omega_0}$, computed in the reference configuration Ω_0, must be pulled back to the computational domain via the mapping $\boldsymbol{\varphi}_0:[-1,1]^2\to\Omega_0$ with deformation gradient $\boldsymbol{F}_0=\nabla_\xi\boldsymbol{\varphi}_0$. This yields the computational stress:

$$\mathbf{P}_{\text{curr}}=|\det\boldsymbol{F}_0|\,\mathbf{P}_{\Omega_0}\cdot\boldsymbol{F}_0^{-T}\tag{3.1}$$

where $|\det\boldsymbol{F}_0|$ accounts for the volume scaling between domains and $\boldsymbol{F}_0^{-T}$ transforms the stress covector components from reference to physical/current coordinates.

3.1.4. A DIFFERENTIAL GEOMETRY PERSPECTIVE

From the differential geometry viewpoint introduced in Section 2.3, the flowmap $\boldsymbol{\varphi}$ is a smooth diffeomorphism between manifolds Ω_0 and Ω_t (viewed as submanifolds of $\mathbb{R}^3$), which induces natural linear transformations between tangent spaces, cotangent spaces, and tensor bundles [Marsden et al., 1984].

Remark 3.1.2

The deformation gradient $\boldsymbol{F} = \boldsymbol{\varphi}_*$ is precisely the *pushforward map* (also called the tangent map or differential): $\boldsymbol{\varphi}_* : T^*_{\mathbf{X}}\Omega_0 \to T^*_{\mathbf{x}}\Omega_t$ with $d\mathbf{x} = \boldsymbol{\varphi}_*(d\mathbf{X}) = \boldsymbol{F}\cdot d\mathbf{X}$. The pushforward is a linear isomorphism between cotangent spaces at corresponding points, with inverse $\boldsymbol{F}^{-1} = (\boldsymbol{\varphi}_*)^{-1}$.

The pullback operation $\boldsymbol{\varphi}^*$ acts in the opposite direction, transforming differential forms from the current to the reference configuration. For cotangent vectors (1-forms), the pullback preserves the natural pairing with tangent vectors. If $\alpha \in T^*_{\mathbf{x}}\Omega_t$ is a spatial covector, the pulled-back covector satisfies $(\boldsymbol{\varphi}^*\alpha)_{\mathbf{X}}(d\mathbf{X}) = \alpha_{\mathbf{x}}(\boldsymbol{\varphi}_* d\mathbf{X}) = \alpha_{\mathbf{x}}\, d\mathbf{x}$. The pullback extends to differential forms of all degrees, and the transformation of volume forms is particularly important: $\boldsymbol{\varphi}^*(dx_1 \wedge dx_2 \wedge dx_3) = J\,(dX_1 \wedge dX_2 \wedge dX_3)$, recovering the familiar relation $dV = J\,dV_0$ from the geometric viewpoint. Oriented surface elements transform according to Nanson's formula, which can be derived from the requirement that the volume element formed by three line elements transform consistently: $\mathbf{n}\,d\Gamma = J\boldsymbol{F}^{-T}\cdot \mathbf{n}_0\,d\Gamma_0$, where $\mathbf{n}_0$ and $\mathbf{n}$ are outward unit normals in the reference and current configurations. This formula is useful for transforming surface tractions and deriving relationships between stress measures.

3.2. MEASURES OF DEFORMATION

The deformation gradient $\boldsymbol{F}$ contains information about both rotation and stretching. To isolate pure deformation from rigid body motions, we construct strain measures that vanish for all rigid translations and rotations (also follows from the polar decomposition of $\boldsymbol{F} = \boldsymbol{R}\boldsymbol{U}$ where $\boldsymbol{R}$ is a rotation matrix and $\boldsymbol{U}$ is the right, symmetric Cauchy stretch tensor).

3.2.1. RIGHT CAUCHY-GREEN TENSOR

Definition 27 (Right Cauchy-Green deformation tensor)**.** *The right Cauchy-Green tensor is defined as* $\boldsymbol{C} = \boldsymbol{F}^T\cdot\boldsymbol{F}$*, a symmetric, positive-definite material tensor with all indices referring to the reference configuration.*

The geometric significance of $\boldsymbol{C}$ is that it measures the change in squared length of material line elements: $\|d\mathbf{x}\|^2 = d\mathbf{x}\cdot d\mathbf{x} = (\boldsymbol{F}\cdot d\mathbf{X})\cdot(\boldsymbol{F}\cdot d\mathbf{X}) = d\mathbf{X}\cdot\boldsymbol{C}\cdot d\mathbf{X}$. Thus, $\boldsymbol{C}$ acts as a Riemannian metric on the reference configuration induced by the deformation, with component form $\|d\mathbf{x}\|^2 = C_{ij}\,dX_i\,dX_j$. C^{-1} is then is the pullback of the metric is spatial coordinates to the material coordinates. For a rigid body motion $\boldsymbol{\varphi}(\mathbf{X},t) = \mathbf{a}(t) + \mathbf{Q}(t)\cdot\mathbf{X}$ (where $\mathbf{Q}$ is a rotation matrix), we have $\boldsymbol{F} = \mathbf{Q}$ and thus $\boldsymbol{C} = \mathbf{Q}^T\cdot\mathbf{Q} = \mathbf{I}$, and conversely $\boldsymbol{C} = \mathbf{I}$ implies rigid motion. This shows that $\boldsymbol{C}$ filters out rotations, depending only on stretching and shearing. The right Cauchy-Green tensor also determines changes in angles between material fibres. For two initially orthogonal line elements $d\mathbf{X}^{(1)}$ and $d\mathbf{X}^{(2)}$, the angle Θ between their deformed images satisfies

$$\cos\Theta = \left(d\mathbf{X}^{(1)}\cdot\boldsymbol{C}\cdot d\mathbf{X}^{(2)}\right)\left(\sqrt{d\mathbf{X}^{(1)}\cdot\boldsymbol{C}\cdot d\mathbf{X}^{(1)}}\sqrt{d\mathbf{X}^{(2)}\cdot\boldsymbol{C}\cdot d\mathbf{X}^{(2)}}\right)^{-1} \tag{3.2}$$

Expressing $\boldsymbol{C}$ in terms of displacement yields $\boldsymbol{C} = (\mathbf{I} + \nabla_0\mathbf{u})^T\cdot(\mathbf{I} + \nabla_0\mathbf{u}) = \mathbf{I} + \nabla_0\mathbf{u} + (\nabla_0\mathbf{u})^T + (\nabla_0\mathbf{u})^T\cdot\nabla_0\mathbf{u}$, illustrating the non-linearity in the deformation gradient.

3.2.2. GREEN-LAGRANGE STRAIN TENSOR

Definition 28 (Green-Lagrange strain tensor)**.** *The Green-Lagrange strain tensor is* $\boldsymbol{E} = \frac{1}{2}(\boldsymbol{C} - \mathbf{I}) = \frac{1}{2}(\boldsymbol{F}^T\cdot\boldsymbol{F} - \mathbf{I})$*, or in terms of displacement,* $\boldsymbol{E} = \frac{1}{2}\left[\nabla_0\mathbf{u} + (\nabla_0\mathbf{u})^T + (\nabla_0\mathbf{u})^T\cdot\nabla_0\mathbf{u}\right]$.

The factor of 1/2 is chosen so that $\boldsymbol{E}$ reduces to the classical covector-valued strain tensor for small deformations. The Green-Lagrange strain vanishes for all rigid body motions ($\boldsymbol{E} = \mathbf{0} \Leftrightarrow \boldsymbol{C} = \mathbf{I}$), making it an ideal measure of pure deformation [Reddy, 2013]. The change in squared length relates directly to $\boldsymbol{E}$ via $\|d\mathbf{x}\|^2 - \|d\mathbf{X}\|^2 = 2\,d\mathbf{X}\cdot\boldsymbol{E}\cdot d\mathbf{X}$. For a material fibre initially in direction $\mathbf{M}$ (unit vector), the stretch ratio $\lambda = \|d\mathbf{x}\|/\|d\mathbf{X}\|$ satisfies $\lambda = \sqrt{1 + 2\mathbf{M}\cdot\boldsymbol{E}\cdot\mathbf{M}}$. The structure of $\boldsymbol{E}$ reveals the distinction between linear and non-linear theories: the linear part $\frac{1}{2}[\nabla_0\mathbf{u} + (\nabla_0\mathbf{u})^T]$ is the symmetric deformation gradient representing covector-valued strain, while the quadratic term $\frac{1}{2}(\nabla_0\mathbf{u})^T\cdot\nabla_0\mathbf{u}$ captures geometric non-linearity and becomes significant when $\|\nabla_0\mathbf{u}\| \not\ll 1$. When deformation gradients are small $\|\nabla_0\mathbf{u}\| \ll 1$, the quadratic term can be neglected to give $\boldsymbol{E} \approx \boldsymbol{\varepsilon} = \frac{1}{2}[\nabla_0\mathbf{u} + (\nabla_0\mathbf{u})^T]$ (covector-valued strain), recovering linear elasticity where the distinction between reference and current configurations vanishes and governing equations simplify dramatically.

Example 3.2.1: Uniaxial extension

Consider uniform extension in the X_1-direction with $x_1 = \lambda X_1$, $x_2 = X_2$, $x_3 = X_3$ for stretch λ. Then $\boldsymbol{F} = \operatorname{diag}(\lambda, 1, 1)$, $\boldsymbol{C} = \operatorname{diag}(\lambda^2, 1, 1)$, and $E_{11} = (\lambda^2 - 1)/2$. For small elongation $\lambda = 1 + \epsilon$ with $\epsilon \ll 1$, we have $E_{11} = [(1+\epsilon)^2 - 1]/2 = \epsilon + \epsilon^2/2 \approx \epsilon$, recovering linear strain. For large elongation $\lambda = 2$ (100% extension), we get $E_{11} = (4-1)/2 = 1.5$, whereas linear theory gives $\varepsilon_{11} = 1$. The 50% difference illustrates the necessity of geometric non-linearity.

Example 3.2.2: Simple shear

For simple shear $x_1 = X_1 + \gamma X_2$, $x_2 = X_2$, $x_3 = X_3$, the deformation gradient is $\boldsymbol{F} = \begin{bmatrix} 1 & \gamma & 0 \\ 0 & 1 & 0 \\ 0 & 0 & 1 \end{bmatrix}$ and the Green-Lagrange strain is $\boldsymbol{E} = \begin{bmatrix} 0 & \gamma/2 & 0 \\ \gamma/2 & \gamma^2/2 & 0 \\ 0 & 0 & 0 \end{bmatrix}$. For small shear, $E_{12} = \gamma/2$ dominates, but for large shear, the non-linear normal strain $E_{22} = \gamma^2/2$ becomes significant, coupling shear and extension in a purely non-linear effect absent in infinitesimal-strain theory.

Example 3.2.3: Rigid rotation

For rotation about X_3 by angle θ, the deformation gradient is $\boldsymbol{F} = \begin{bmatrix} \cos\theta & -\sin\theta & 0 \\ \sin\theta & \cos\theta & 0 \\ 0 & 0 & 1 \end{bmatrix}$, giving $\boldsymbol{C} = \mathbf{I}$ and $\boldsymbol{E} = \mathbf{0}$, correctly showing zero strain for any θ. In contrast, covector-valued strain $\boldsymbol{\varepsilon} \neq \mathbf{0}$ unless θ is very small.

3.3. STRESS MEASURES

Multiple stress measures arise when formulating equilibrium equations in different configurations, because areas in the reference configuration differ from areas in the current configuration in both magnitude and orientation [Marsden et al., 1984]. This necessitates the definitions of different stress tensors depending on which configuration is used for forces and areas (see Figure 3.2).

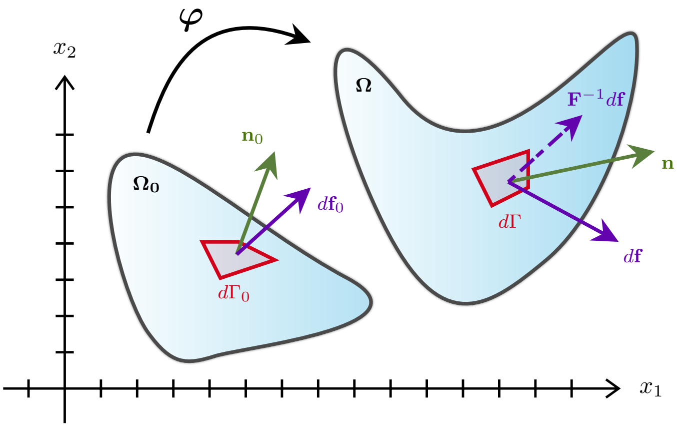

Figure 3.2: Schematic of stress measure quantities. A material surface element $d\Gamma_0$ on Ω_0 with normal $\mathbf{n}_0$ in the reference configuration deforms to $d\Gamma$ on Ω with normal $\mathbf{n}$ in the current configuration. Tractions $\mathbf{t}_0$ and $\mathbf{t}$ result in forces $d\mathbf{f}_0$ and $d\mathbf{f}$. The deformation gradient $\boldsymbol{F}$ and Jacobian $J = \det \boldsymbol{F}$ govern the transformation.

3.3.1. Cauchy Stress Tensor

Definition 29 (Cauchy stress tensor $\boldsymbol{\sigma}$)**.** *The physical stress in the current configuration relates traction to surface normal via* $\mathbf{t} = \boldsymbol{\sigma}\cdot\mathbf{n}$ *and* $d\mathbf{f} = \boldsymbol{\sigma}\cdot\mathbf{n}\,d\Gamma$. *The Cauchy stress is a symmetric spatial tensor (*$\boldsymbol{\sigma} = \boldsymbol{\sigma}^T$*), with symmetry following from balance of angular momentum.*

The Cauchy stress is the natural measure of stress, hence what is actually experienced by the material and measured in experiments. This is what is used to indicate phenomena like failure, damage, plasticity, and other physics-oriented observations. Its diagonal components $\sigma_{11}, \sigma_{22}, \sigma_{33}$ represent normal stresses (positive for tension, negative for compression), while off-diagonal components $\sigma_{12}, \sigma_{13}, \sigma_{23}$ represent shear stresses. However, for Lagrangian formulations where equations are derived in the reference configuration, working directly with $\boldsymbol{\sigma}$ is inconvenient because the geometry of the current configuration is unknown (it's part of the solution), motivating the introduction of stress measures that relate quantities between configurations.

3.3.2. Piola-Kirchhoff Stress Tensors

Definition 30 (First Piola-Kirchhoff stress $\boldsymbol{P}$)**.** *A two-point tensor relating current force to reference area via* $d\mathbf{f} = \boldsymbol{P}\cdot\mathbf{n}_0\,d\Gamma_0$. *Using Nanson's formula* $\mathbf{n}\,d\Gamma = J\boldsymbol{F}^{-T}\cdot\mathbf{n}_0\,d\Gamma_0$, *we find* $\boldsymbol{P} = J\,\boldsymbol{\sigma}\cdot\boldsymbol{F}^{-T}$ *and* $\boldsymbol{\sigma} = J^{-1}\boldsymbol{P}\cdot\boldsymbol{F}^T$.

The first PK stress $\boldsymbol{P}$ has one spatial index (force direction) and one material index (surface orientation), making it a two-point tensor that is generally non-symmetric because it relates different coordinate systems. The name "Piola transformation" refers to the relation $\boldsymbol{P} = J\boldsymbol{\sigma}\cdot\boldsymbol{F}^{-T}$ accounting for area change and normal rotation. The equilibrium equations in the reference configuration involve $\nabla_0\cdot\boldsymbol{P}$, making $\boldsymbol{P}$ natural for variational formulations in the total Lagrangian framework, and moreover $\boldsymbol{P}$ is energy-conjugate to $\boldsymbol{F}$ with stress power per unit reference volume given by $\mathcal{P} = \boldsymbol{P} : \dot{\boldsymbol{F}}$.

Definition 31 (Second Piola-Kirchhoff stress $\boldsymbol{S}$)**.** *A symmetric material tensor obtained by pulling back both force and area:* $d\mathbf{f}_0 = \boldsymbol{F}^{-1}\cdot d\boldsymbol{f} = \boldsymbol{S}^T\cdot\mathbf{n}_0\,d\Gamma_0$, *giving* $\boldsymbol{S} = \boldsymbol{F}^{-1}\cdot\boldsymbol{P} = J\boldsymbol{F}^{-1}\cdot\boldsymbol{\sigma}\cdot\boldsymbol{F}^{-T}$ *and* $\boldsymbol{\sigma} = J^{-1}\boldsymbol{F}\cdot\boldsymbol{S}\cdot\boldsymbol{F}^T$.

The second PK stress $\boldsymbol{S}$ is a purely material tensor (all indices refer to the reference configuration) and is symmetric ($\boldsymbol{S} = \boldsymbol{S}^T$), with this symmetry inherited from $\boldsymbol{\sigma}$ and reducing independent components from nine to six. Crucially, $\boldsymbol{S}$ is objective (frame-indifferent): under superposed rigid rotations, its components remain unchanged, making it ideal for constitutive modeling. The second PK stress is energy-conjugate to the Green-Lagrange strain via $\mathcal{P} = \boldsymbol{S} : \dot{\boldsymbol{E}}$, and this work-conjugacy is fundamental for hyperelastic constitutive models.

Remark 3.3.1

From the differential-geometric perspective, stress measures arise naturally from pullback/pushforward operations. Geometrically, the Cauchy stress $\boldsymbol{\sigma}$ is a covector-valued surface form; its usual representation in $T_{\mathbf{x}}\Omega_t \otimes T_{\mathbf{x}}\Omega_t$ comes only after identifying surfaces with vectors via the metric, and therefore should not be interpreted as acting on a direct product of tangent vectors. The first Piola-Kirchhoff stress $\boldsymbol{P}$ is the pullback of the area-form part of $\boldsymbol{\sigma}$ to the reference configuration, leaving the force-valued leg spatial (symbolically written as $T_{\mathbf{x}}\Omega_t \otimes T^*_{\mathbf{X}}\Omega_0$ to indicate this mixed character). The second Piola–Kirchhoff stress $\boldsymbol{S}$ is the full pullback to material space. The relations $\boldsymbol{P} = \boldsymbol{F}\cdot\boldsymbol{S}$ and $\boldsymbol{\sigma} = J^{-1}\boldsymbol{F}\cdot\boldsymbol{S}\cdot\boldsymbol{F}^T$ follow from applying pushforward and pullback to the form-leg only, as emphasised in [Kanso et al., 2007].

Table 3.1: Properties of stress tensors. Notice how each stress measure serves a specific purpose: $\boldsymbol{\sigma}$ for physical interpretation, $\boldsymbol{P}$ for variational formulations, and $\boldsymbol{S}$ for constitutive modelling.

Stress	Configuration	Symmetric	Objective	Conjugate to
$\boldsymbol{\sigma}$	Spatial	Yes	Yes	d
$\boldsymbol{P}$	Two-point	No	No	$\boldsymbol{F}$
$\boldsymbol{S}$	Material	Yes	Yes	$\boldsymbol{E}$

3.4. Hyperelastic Constitutive Relations

Having established kinematic (strain) and kinetic (stress) measures, we now address the constitutive relation-the material-specific law connecting stress to deformation - without which the balance laws are underdetermined.

3.4.1. HYPERELASTICITY

Definition 32 (Hyperelastic material)**.** *A material is hyperelastic if there exists a strain energy density function* $W(\boldsymbol{E})$ *or* $W(\boldsymbol{C})$ *such that stress derives from a potential:* $\boldsymbol{S} = \partial W/\partial \boldsymbol{E} = 2\partial W/\partial \boldsymbol{C}$. *The total deformation energy is* $E_{\text{def}} = \int_{\Omega_0} W(\mathbf{X}, \boldsymbol{C})\, dV_0$, *where W may depend on position* $\mathbf{X}$ *for inhomogeneous materials [Fu and Ogden, 2001].*

The factor of 2 in $\boldsymbol{S} = 2\partial W/\partial \boldsymbol{C}$ arises from the chain rule via $\boldsymbol{E} = \frac{1}{2}(\boldsymbol{C} - \mathbf{I})$. Hyperelasticity ensures several important properties: thermodynamic consistency through the rate of energy storage equaling stress power ($\dot{W} = \boldsymbol{S} : \dot{\boldsymbol{E}}$), path-independence where stress depends only on current deformation and not on history, conservative behaviour where work done over closed deformation paths vanishes (no dissipation), and automatic symmetry of stress since $\boldsymbol{S}$ derives from the scalar W, and the fact that $\boldsymbol{E}$ and $\boldsymbol{C}$ are symmetric by construction.. The choice of W characterizes the material, with different functional forms describing rubber (neo-Hookean), soft tissues (Fung), foams (Ogden), and other materials. Naturally, the challenge in constitutive modelling is defining W such that it best approximates physical behaviour while remaining mathematically tractable and thermodynamically admissible.

3.4.2. ISOTROPIC HYPERELASTICITY

Definition 33 (Material isotropy)**.** *A material is isotropic if its response is independent of material orientation:* $W(\boldsymbol{C}) = W(\mathbf{Q}^T \cdot \boldsymbol{C} \cdot \mathbf{Q})$ *for all* $\mathbf{Q} \in \mathrm{SO}(3)$.

By the Rivlin-Ericksen representation theorem, isotropic W depends only on the principal invariants of $\boldsymbol{C}$:

$$\begin{gathered} I_1(\boldsymbol{C}) = \operatorname{tr}(\boldsymbol{C}) = \lambda_1^2 + \lambda_2^2 + \lambda_3^2 \qquad I_2(\boldsymbol{C}) = \frac{1}{2}\left[(\operatorname{tr}\boldsymbol{C})^2 - \operatorname{tr}(\boldsymbol{C}^2)\right] = \lambda_1^2\lambda_2^2 + \lambda_2^2\lambda_3^2 + \lambda_3^2\lambda_1^2 \\ I_3(\boldsymbol{C}) = \det(\boldsymbol{C}) = J^2 = \lambda_1^2\lambda_2^2\lambda_3^2 \end{gathered} \tag{3.3}$$

where $\lambda_1, \lambda_2, \lambda_3$ are principal stretches (eigenvalues of $\mathbf{U}$ in the polar decomposition $\boldsymbol{F} = \mathbf{R} \cdot \mathbf{U}$, $\mathbf{U}^2 = \boldsymbol{C}$). Thus $W(\boldsymbol{C}) = \widehat{W}(I_1, I_2, I_3)$, and stress is computed via chain rule

$$\boldsymbol{S} = 2\left(\frac{\partial W}{\partial I_1}\frac{\partial I_1}{\partial \boldsymbol{C}} + \frac{\partial W}{\partial I_2}\frac{\partial I_2}{\partial \boldsymbol{C}} + \frac{\partial W}{\partial I_3}\frac{\partial I_3}{\partial \boldsymbol{C}}\right) \tag{3.4}$$

Using the derivatives $\partial I_1/\partial \boldsymbol{C} = \mathbf{I}$, $\partial I_2/\partial \boldsymbol{C} = I_1\mathbf{I} - \boldsymbol{C}$, and $\partial I_3/\partial \boldsymbol{C} = I_3\boldsymbol{C}^{-1}$, we obtain

$$\boldsymbol{S} = 2\left(\frac{\partial W}{\partial I_1}\mathbf{I} + \frac{\partial W}{\partial I_2}(I_1\mathbf{I} - \boldsymbol{C}) + \frac{\partial W}{\partial I_3} I_3 \boldsymbol{C}^{-1}\right) \tag{3.5}$$

This formulation reduces constitutive modelling from specifying a function of six components of $\boldsymbol{C}$ to specifying a scalar function of three invariants and thus greatly simplifies constructing $\boldsymbol{S}$ via some strain energy density function $\boldsymbol{W}$ (which may be material physics-dependent).

Remark 3.4.1: Linearization and Connection to Linear Elasticity

For small deformations $\|\nabla_0 \mathbf{u}\| \ll 1$, hyperelastic materials reduce to linear elasticity through Taylor expansion of $W(\boldsymbol{E})$ about $\boldsymbol{E} = \mathbf{0}$: $W(\boldsymbol{E}) = W(\mathbf{0}) + \frac{\partial W}{\partial \boldsymbol{E}}|_{\boldsymbol{E}=\mathbf{0}} : \boldsymbol{E} + \frac{1}{2}\boldsymbol{E} : \frac{\partial^2 W}{\partial \boldsymbol{E}\partial \boldsymbol{E}}|_{\boldsymbol{E}=\mathbf{0}} : \boldsymbol{E} + O(\|\boldsymbol{E}\|^3)$. Assuming the reference configuration is stress-free so that $\boldsymbol{S}(\mathbf{0}) = \partial W/\partial \boldsymbol{E}|_{\boldsymbol{E}=\mathbf{0}} = \mathbf{0}$, and choosing $W(\mathbf{0}) = 0$, we obtain $W(\boldsymbol{E}) \approx \frac{1}{2}\boldsymbol{E} : \mathbb{C} : \boldsymbol{E}$ and $\boldsymbol{S} = \mathbb{C} : \boldsymbol{E}$, where $\mathbb{C}$ is the fourth-order elasticity tensor. For isotropic materials, $\mathbb{C}_{IJKL} = \lambda\delta_{IJ}\delta_{KL} + \mu(\delta_{IK}\delta_{JL} + \delta_{IL}\delta_{JK})$, giving Hooke's law $\boldsymbol{S} = \lambda \operatorname{tr}(\boldsymbol{E})\mathbf{I} + 2\mu\boldsymbol{E}$. The Lamé parameters λ, μ relate to Young's modulus E and Poisson's ratio ν via $\mu = E/[2(1+\nu)]$ and $\lambda = E\nu/[(1+\nu)(1-2\nu)]$. The corresponding strain energy is $W(\boldsymbol{E}) = \frac{\lambda}{2}[\operatorname{tr}(\boldsymbol{E})]^2 + \mu \operatorname{tr}(\boldsymbol{E}^2)$, i.e. linear elasticity is the first-order approximation to hyperelasticity near the undeformed state.

3.4.3. SAINT VENANT-KIRCHHOFF MODEL

Definition 34 (Saint Venant-Kirchhoff model)**.** *The simplest hyperelastic extension of linear elasticity uses the quadratic energy function* $W(\boldsymbol{E}) = \frac{\lambda}{2}[\operatorname{tr}(\boldsymbol{E})]^2 + \mu \operatorname{tr}(\boldsymbol{E}^2)$, *giving the constitutive relation* $\boldsymbol{S} = \partial W/\partial \boldsymbol{E} = \lambda \operatorname{tr}(\boldsymbol{E})\mathbf{I} + 2\mu\boldsymbol{E} = \mathbb{C} : \boldsymbol{E}$.

The Saint Venant-Kirchhoff (SVK) model retains Hooke's linear stress-strain relation but uses the full non-linear Green-Lagrange strain including the quadratic term $(\nabla_0\mathbf{u})^T \cdot \nabla_0\mathbf{u}$, thus capturing geometric non-linearity (finite rotations, large displacements) while maintaining material linearity. Advantages include using material Lamé parameters λ, μ (or E, ν) from linear elasticity, reducing to linear theory for small deformations, computational efficiency, and handling finite rotations exactly. Limitations include non-physical behaviour under large compression where the quadratic W is not bounded from below and can become negative, lack of polyconvexity potentially causing non-existence of solutions for extreme loads, and less accuracy for very large stretches since real materials typically stiffen while SVK does not [Bernd Sautter et al., 2022]. Despite these limitations, SVK is widely used for moderate deformations in structural mechanics, such as large deflections of beams/plates/shells [Khaniki et al., 2023], buckling analysis, and flexible multibody dynamics.

Example 3.4.1: SVK versus geometrically linear elasticity

For 100% uniaxial extension ($\lambda = 2$), the SVK model gives $E_{11} = 1.5$ and stress $S_{11} = (2\lambda + 2\mu)E_{11} = (2\lambda + 2\mu)(1.5)$, versus linear theory with $\varepsilon_{11} = 1.0$ and stress $\sigma_{11}^{\text{lin}} = (2\lambda + 2\mu)(1.0)$. The 50% difference in strain translates to 50% error in stress prediction, demonstrating the necessity of geometric non-linearity.

Remark 3.4.2

For applications requiring very large strains or strong material non-linearity, more sophisticated models should be used, such as Neo-Hookean with $W = \frac{\mu}{2}(I_1 - 3)$, Mooney-Rivlin with $W = C_1(I_1 - 3) + C_2(I_2 - 3)$, or Ogden models with strain-stiffening [Ogden, 1973] [Rivlin, 1948]. These can be readily incorporated into the MSEM framework by changing W while retaining the overall formulation.

3.4.4. Plane Strain Formulation for Two-Dimensional Problems

While the framework developed above is formulated in three-dimensional space, many practical problems can be effectively modelled in two dimensions under appropriate assumptions. For the numerical implementation of hyperelastic MSEM, we restrict attention to two-dimensional problems under the *plane strain* assumption [Zienkiewicz et al., 2006].

Definition 35 (Plane strain)**.** *A deformation is in plane strain if the out-of-plane displacement component vanishes ($u_3 = 0$) and all in-plane quantities are independent of the out-of-plane coordinate ($\partial(\cdot)/\partial X_3 = 0$). This assumption is valid for bodies with one dimension much larger than the other two (e.g., long cylinders, dams, retaining walls) when loading and geometry are uniform in the long direction.*

Under plane strain, the flowmap reduces to $\mathbf{x} = \boldsymbol{\varphi}(\mathbf{X}, t)$ with $x_1 = \varphi^1(X_1, X_2, t)$, $x_2 = \varphi^2(X_1, X_2, t)$, and $x_3 = X_3$. The deformation gradient becomes

$$\boldsymbol{F} = \begin{bmatrix} \frac{\partial x_1}{\partial X_1} & \frac{\partial x_1}{\partial X_2} & 0 \\ \frac{\partial x_2}{\partial X_1} & \frac{\partial x_2}{\partial X_2} & 0 \\ 0 & 0 & 1 \end{bmatrix} = \begin{bmatrix} F_{11} & F_{12} & 0 \\ F_{21} & F_{22} & 0 \\ 0 & 0 & 1 \end{bmatrix} \tag{3.6}$$

with Jacobian $J = \det \boldsymbol{F} = F_{11}F_{22} - F_{12}F_{21}$. The Green-Lagrange strain tensor similarly reduces to

$$\boldsymbol{E} = \begin{bmatrix} E_{11} & E_{12} & 0 \\ E_{12} & E_{22} & 0 \\ 0 & 0 & 0 \end{bmatrix} \tag{3.7}$$

where the in-plane components are computed from the in-plane displacement gradients via $E_{IJ} = \frac{1}{2}\left[\frac{\partial u_I}{\partial X_J} + \frac{\partial u_J}{\partial X_I} + \frac{\partial u_K}{\partial X_I}\frac{\partial u_K}{\partial X_J}\right]$ for $I, J \in \{1, 2\}$, with the summation over K restricted to in-plane indices. For the SVK constitutive model in plane strain, the strain energy density becomes

$$W(\boldsymbol{E}) = \frac{\lambda}{2}[\operatorname{tr}(\boldsymbol{E})]^2 + \mu \operatorname{tr}(\boldsymbol{E}^2) = \frac{\lambda}{2}(E_{11} + E_{22})^2 + \mu(E_{11}^2 + E_{22}^2 + 2E_{12}^2) \tag{3.8}$$

and the corresponding second Piola-Kirchhoff stress has non-zero in-plane components

$$S_{11} = \lambda(E_{11} + E_{22}) + 2\mu E_{11}, \quad S_{22} = \lambda(E_{11} + E_{22}) + 2\mu E_{22}, \quad S_{12} = 2\mu E_{12} \tag{3.9}$$

The out-of-plane stress component $S_{33} = \lambda(E_{11} + E_{22})$ is non-zero but does not enter the in-plane equilibrium equations. The strain tensor - in Voigt notation - is represented as a vector $\mathbf{E} = (E_{11}, E_{22}, 2E_{12})^T \in \mathbb{R}^3$, where the factor of 2 in the shear component is the engineering shear strain convention. The constitutive relation then takes the matrix form $\boldsymbol{S} = \mathbf{C}\mathbf{E}$, where $\mathbf{C} \in \mathbb{R}^{3\times3}$ is the plane strain elasticity matrix

$$\mathbf{C} = \frac{E}{1 - \nu^2}\begin{bmatrix} 1 & \nu & 0 \\ \nu & 1 & 0 \\ 0 & 0 & \frac{1-\nu}{2} \end{bmatrix} \tag{3.10}$$

expressed in terms of Young's modulus $E = 4\mu(\lambda + \mu)/(\lambda + 2\mu)$ and Poisson's ratio $\nu = \lambda/(2(\lambda + \mu))$. The stored energy can be written in a more convenient form $\rho_0 W(\mathbf{E}) = \mathbf{E}^T\mathbf{C}\mathbf{E}$.

Remark 3.4.3

The plane strain assumption differs from plane stress (appropriate for thin plates), where out-of-plane stress vanishes rather than out-of-plane strain. The choice between these assumptions depends on the geometry and loading of the physical problem. Plane strain is appropriate when the third dimension is constrained or when the body is very long in one direction with uniform cross-section and loading. In plane stress, $\sigma_{33} = \sigma_{13} = \sigma_{23} = 0$ for the out-of-plane direction (i.e. axis "3"). It can be intuitively put as on a free surface, a local state of plane stress holds, since this is exactly the boundary condition.

3.5. GEOMETRIC STRUCTURE OF ELASTICITY

The elasticity complex above possesses a rich geometric interpretation that connects naturally to the framework of differential forms developed in Chapter 2. This section opens the connection to geometry as in [Marsden et al., 1984] and developments in structure-preserving discretisation [Kanso et al., 2007] [Angoshtari and Yavari, 2013] [Yavari, 2008] [Marsden et al., 2001] [Rashad et al., 2023].

3.5.1. STRESS, A COVECTOR-VALUED TWO-FORM

In the space-time formulation employed in this work, the first Piola-Kirchhoff stress $\mathbf{P}$ is naturally described as a covector-valued 2-form in space-time-a 1-form in space and a 1-form in time-belonging to the dual space $\tilde{\Lambda}^{(2)}(\mathcal{M})$, where $\mathcal{M}$ is the three-dimensional space-time manifold (two spatial dimensions plus one temporal dimension).

Definition 36 (Stress form)**.** *The stress form is an element of* $T_x^*\mathcal{S} \otimes \Lambda^2(S)$*, where* $T_x^*\mathcal{S}$ *is the cotangent bundle (dual space) and* $\Lambda^2(S)$ *is the space of 2-forms. For two-dimensional plane strain, a general stress form has the local representation:*

$$\mathbf{t} = dx^a \otimes \mathbf{t}_a, \tag{3.11}$$

where $\mathbf{t}_a$ *are 2-forms in space-time. In the spatial (Eulerian) description, the stress form* $\mathbf{t}$ *is related to the Cauchy stress tensor* $\boldsymbol{\sigma}$ *through*

$$\mathbf{t} = \star_2 \boldsymbol{\sigma}, \tag{3.12}$$

where $\star_2$ *denotes that the Hodge star operator acts on the second "leg" (the area-form part) of the stress tensor, transforming it into a 2-form while leaving the covector (force direction) unchanged.*

For our Lagrangian formulation, however, we work directly with the first Piola-Kirchhoff stress $\mathbf{P}$, which already possesses the structure of a covector-valued 2-form on the reference configuration [Kanso et al., 2007]. This tensor naturally lives in the dual space $\tilde{\Lambda}^{(2)}(\mathcal{M}_0)$, relating forces in the current configuration to oriented surface elements in the reference configuration via $d\mathbf{f} = \mathbf{P} \cdot \mathbf{n}_0 \, dA_0$.

Remark 3.5.1

The sign convention for recovering the Cauchy stress from the stress form, $\boldsymbol{\sigma} = -\star_2 \mathbf{t}$, arises from the orientation of the space-time manifold and ensures consistency with the standard definition of traction forces as $\mathbf{t}(\mathbf{x}, t; \mathbf{n}) = \boldsymbol{\sigma}(\mathbf{x}, t) \cdot \mathbf{n}$.

The geometric formulation of stress naturally expresses the work done by internal forces. Consider a material body occupying a space-time region $\mathcal{M} = \Omega_0 \times [0, T]$. The stress, upon pairing with the deformation gradient, provides a form that is ready to be integrated over a space-time region.

Definition 37 (Stress power)**.** *For a deformation gradient* $\mathbf{F} \in \Lambda^{(1)}(\mathcal{M})$ *(a primal 1-form in space) and stress* $\mathbf{P} \in \tilde{\Lambda}^{(2)}(\mathcal{M})$ *(a dual 1-form in space and 1-form in time), the work done by stress over an oriented space-time region* $\mathcal{R} \subset \mathcal{M}$ *is:*

$$W^{\mathbf{P}} = \int_{\mathcal{R}} \langle \mathbf{P}, \mathbf{F} \rangle \tag{3.13}$$

where the angle brackets $\langle \cdot, \cdot \rangle$ *denote the pairing between the primal 1-form in space and the dual 1-form in space (contained in* $\mathbf{P}$*), producing a 3-form that integrates naturally over the space-time region* $\mathcal{R}$*.*

In traditional notation, this recovers the expression:

$$W^{\mathbf{P}} = \int_{\mathcal{R}} \langle \mathbf{P}, \mathbf{F} \rangle = \int_0^T \int_{\Omega_0} \mathbf{P} : \mathbf{F} \, dA \, dt \tag{3.14}$$

where $\mathbf{P} : \mathbf{F}$ denotes the double contraction of the first Piola-Kirchhoff stress tensor with the deformation gradient.

The advantage of the covector-valued 2-form perspective is that it naturally incorporates orientation. Changing the orientation of a spatial curve (part of the boundary of Ω_0) automatically changes the sign of the integrated quantity, which is the physical behaviour we expect from stress [Kanso et al., 2007].

The momentum field, like stress, naturally lives in the dual space as a covector-valued form. In local coordinates (ξ,η,τ) on our space-time manifold, the momentum 2-form has the representation:

$$\boldsymbol{\pi}^{(2)} = \left(dx \otimes \pi_x^{(2)}(\xi,\eta,\tau) + dy \otimes \pi_y^{(2)}(\xi,\eta,\tau)\right) d\xi \wedge d\eta, \tag{3.15}$$

where $\pi_x^{(2)}$ and $\pi_y^{(2)}$ are the components of momentum density as 2-forms in space (and 0-forms in time), and (x,y) denote spatial coordinates in the current configuration. The differentials dx and dy indicate that the momentum values lie in the spatial cotangent space, while $d\xi \wedge d\eta$ shows that the form itself is expressed in reference coordinates. It is integrated over spatial regions to give total momentum, and it pairs with velocity (a primal 1-form in time) to produce twice the kinetic energy density.

3.5.2. Piola Transformation as a Pullback

Recall from Subsection 3.3.2 that the first Piola-Kirchhoff stress $\mathbf{P}$ and Cauchy stress $\boldsymbol{\sigma}$ are related through the Piola transformation:

$$J\boldsymbol{\sigma} = \mathbf{P}\boldsymbol{F}^T \tag{3.16}$$

This relation has a geometric interpretation in terms of stress-forms. We can define the material stress form $\mathbf{p}$ analogously to $\mathbf{t}$:

$$\mathbf{p} = \star_2 \mathbf{P} \tag{3.17}$$

where now $\mathbf{p} \in T^*_{\mathbf{X}}\Omega_0 \otimes \Lambda^2(\mathcal{M}_0)$ lives on the reference configuration space-time manifold $\mathcal{M}_0 = \Omega_0 \times [0,T]$. The Piola transformation (3.16), when written in terms of the stress-forms $\mathbf{t}$ and $\mathbf{p}$, reads as:

$$\mathbf{p} = \varphi^{*(2)}\mathbf{t} \tag{3.18}$$

where $\varphi^{*(2)}$ is the pullback operation acting on the 2-form (area) part of the stress form, leaving the covector (force) part unchanged.

Remark 3.5.2

The geometric interpretation is now transparent: $\mathbf{p}$ is **the pullback of the area-form part of t** that does nothing to the covector-valued part. This is precisely the content of the Piola transformation, which transforms surface areas from the current to reference configuration via φ^* while keeping force directions in the current (spatial) configuration.

To see this explicitly, note that for a surface element dA in Ω_0 with normal $\mathbf{N}$, Nanson's formula gives:

$$\mathbf{n}\, d\Gamma = J\boldsymbol{F}^{-T} \cdot \mathbf{N}\, dA, \tag{3.19}$$

which in the language of differential forms is the statement that:

$$\varphi^*\left(\star dx^b\right) = J\left(\boldsymbol{F}^{-1}\right)_B^b \star dX^B. \tag{3.20}$$

3.5.3. Towards MSEM

In the MSEM framework developed in Chapter 2, configuration variables live in primal spaces while force-like quantities live in dual spaces. This distinction becomes particularly clear in the geometric stress formulation:

- The flowmap $\boldsymbol{\varphi} \in \Lambda^{(0)}(\mathcal{M})$ is a primal, vector-valued 0-form.
- The velocity $\mathbf{V} \in \Lambda^{(1)}(\mathcal{M})$ is a primal, vector-valued 1-form in time.
- The deformation gradient $\boldsymbol{F} \in \Lambda^{(1)}(\mathcal{M})$ is a primal, vector-valued 1-form in space.
- The momentum $\boldsymbol{\pi} \in \widetilde{\Lambda}^{(2)}(\mathcal{M})$ is a dual, covector-valued 2-form in space and a 0-form in time.
- The stress $\mathbf{P} \in \widetilde{\Lambda}^{(2)}(\mathcal{M})$ as a dual, covector-valued 1-form in space and 1-form in time.

The discrete Hodge operator connects between these primal and dual representations through the weighted mass matrices $\mathbb{M}^{(k)}$. In the **continuous** setting, the Hodge star $\star_2 : T^*\mathcal{S} \otimes T^*\mathcal{S} \to T^*\mathcal{S} \otimes \widetilde{\Lambda}^{(2)}(\mathcal{M})$ transforms the Cauchy stress tensor to create the stress form $\mathbf{t} = \star_2\boldsymbol{\sigma}$ in the spatial description. However, in our Lagrangian formulation, we work directly with the first Piola-Kirchhoff stress $\mathbf{P}$, which *already* naturally lives in the dual space $\widetilde{\Lambda}^{(2)}(\mathcal{M}_0)$ as a covector-valued 2-form on the reference configuration. This choice eliminates the need to explicitly apply $\star_2$ to create the stress form-$\mathbf{P}$ is inherently the appropriate object for our weak formulation. In the **discrete** setting, the Hodge operator appears as precomputed tensors that implement the pairing between primal basis functions $\Psi^{(k)}$ (representing flowmap derivatives) and dual basis functions $\widetilde{\Psi}^{(3-k)}$:

$$\mathbb{H}_{ij}^{(k)} = \int_{\mathcal{M}} \Psi_i^{(k)} \wedge \star \Psi_j^{(k)} \tag{3.21}$$

where $\star : \Lambda^{(k)}(\mathcal{M}) \to \widetilde{\Lambda}^{(3-k)}(\mathcal{M})$ is the three-dimensional space-time Hodge star mapping primal k-forms to dual $(3-k)$-forms. At each space-time quadrature point, the stress components P_{ij} are contracted with precomputed Hodge tensors. This contraction implements the discrete analogue of:

$$\int_{\mathcal{M}} \mathbf{P} : \nabla(\delta\boldsymbol{\varphi})\, dV\, dt = \int_{\mathcal{M}} \langle \mathrm{d}(\delta\boldsymbol{\varphi}), \mathbf{P} \rangle \tag{3.22}$$

where $\mathrm{d}(\delta\boldsymbol{\varphi}) \in \Lambda^{(1)}(\mathcal{M})$ is the spatial exterior derivative (a primal 1-form) and the stress is represented through $\mathbf{P} \in \widetilde{\Lambda}^{(2)}(\mathcal{M})$.

The discrete exterior derivative, the coboundary operator, acts on dual stress variables. The discrete Hodge operation links these through the mass matrices and precomputed bases for the Hodges, ensuring that conservation laws follow from the mimetic discretisation.

3.6. LAGRANGIAN VARIATIONAL FORMULATION FOR HYPERELASTICITY

The equations governing hyperelastic dynamics are derived through Hamilton's principle. This requires finding the configuration for which the action integral, formulated from the Lagrangian representing the system's kinetic and strain energy, is stationary. This variational approach (outlied in detail in [Demoures and Gay-Balmaz, 2022][Demoures et al., 2013]) provides a natural framework for structure-preserving discretisation methods such as MSEM [Mahadev, 2025]. The Lagrangian density of a hyperelastic body evaluated on a configuration map $\boldsymbol{\varphi}(t, \mathbf{X})$ is

$$\mathcal{L}(\boldsymbol{\varphi}, \dot{\boldsymbol{\varphi}}, \nabla_0\boldsymbol{\varphi}) = L(\boldsymbol{\varphi}, \dot{\boldsymbol{\varphi}}, \nabla_0\boldsymbol{\varphi})\, dV_0\, dt = \left[\frac{1}{2}\rho_0 \langle \dot{\boldsymbol{\varphi}}, \dot{\boldsymbol{\varphi}} \rangle - \rho_0 W(\boldsymbol{C}) - \rho_0 \Pi(\boldsymbol{\varphi})\right] dV_0\, dt \tag{3.23}$$

where $\rho_0(\mathbf{X})$ is the reference density, $W(\boldsymbol{C})$ is the strain energy density function (constitutive model) depending on the right Cauchy-Green tensor $\boldsymbol{C} = \boldsymbol{F}^T \cdot \boldsymbol{F}$, and $\Pi(\boldsymbol{\varphi})$ represents potential energy contributions such as body forces or gravitational potential (these forces are not considered in this thesis, but the terms are mentioned for sake of completeness). The dependence on the material coordinates $\mathbf{X}$ and time t is implicit.

Hamilton's principle states that the action integral is stationary:

$$\delta \int_0^T \int_{\Omega_0} L(\boldsymbol{\varphi}, \dot{\boldsymbol{\varphi}}, \nabla_0\boldsymbol{\varphi})\, dV_0\, dt = 0 \tag{3.24}$$

for variations $\delta\boldsymbol{\varphi}$ of the body configuration map with $\delta\boldsymbol{\varphi} = \mathbf{0}$ at $t = 0, T$. Applying the Euler-Lagrange equations from variational calculus yields

$$\frac{d}{dt}\frac{\partial L}{\partial \dot{\boldsymbol{\varphi}}} - \frac{\partial L}{\partial \boldsymbol{\varphi}} = -\nabla_0 \cdot \frac{\partial L}{\partial \boldsymbol{F}} \tag{3.25}$$

together with the natural boundary conditions

$$\frac{\partial L}{\partial \boldsymbol{F}^a_I} n_I \delta\varphi^a = 0 \quad \text{on } \partial\Omega_0 \tag{3.26}$$

for the allowed variations $\delta\boldsymbol{\varphi}$ at the boundary, where $\boldsymbol{F} = \nabla_0\boldsymbol{\varphi}$ is the deformation gradient.

For the Lagrangian density above, we compute

$$\frac{\partial L}{\partial \boldsymbol{F}^a_I} = -2\rho_0 \boldsymbol{F}^a_J \frac{\partial W}{\partial C_{JI}} = -\boldsymbol{F}^a_J S^{JI}, \quad \text{i.e.} \quad \frac{\partial L}{\partial \boldsymbol{F}} = -\boldsymbol{F} \cdot \boldsymbol{S} \tag{3.27}$$

where $\boldsymbol{S} = 2\partial W / \partial \boldsymbol{C}$ is the second Piola-Kirchhoff stress tensor derived from the strain energy function. The Euler-Lagrange equations (3.25) then give the equations of motion for a hyperelastic body as

$$\rho_0 \ddot{\boldsymbol{\varphi}} = \nabla_0 \cdot (\boldsymbol{F} \cdot \boldsymbol{S}) - \rho_0 \frac{\partial \Pi}{\partial \boldsymbol{\varphi}} \tag{3.28}$$

Recognizing that $\boldsymbol{P} = \boldsymbol{F} \cdot \boldsymbol{S}$ is the first Piola-Kirchhoff stress and introducing the canonical momentum $\boldsymbol{\pi} = \partial L / \partial \dot{\boldsymbol{\varphi}} = \rho_0 \dot{\boldsymbol{\varphi}}$, equation (3.28) can be recast in the conservation form:

$$\frac{\partial \boldsymbol{\pi}}{\partial t} = \nabla_0 \cdot \boldsymbol{P} + \mathbf{f}_0 \tag{3.29}$$

where $\mathbf{f}_0 = -\rho_0 \partial\Pi / \partial\boldsymbol{\varphi}$ represents body forces per unit reference volume. This formulation naturally separates inertial effects (left-hand side) from internal elastic forces and external loads (right-hand side), providing the foundation for the space-time weak formulation employed in the MSEM discretisation described in subsequent sections.

Remark 3.6.1

The variational structure ensures that conservation laws follow from Noether's theorem: invariance of the Lagrangian under time translations yields energy conservation, spatial translations yield linear momentum conservation, and rotations yield angular momentum conservation. The MSEM discretisation preserves these symmetries at the discrete level through the mimetic properties of its operators.

4

DISCRETE VARIATIONAL FORMULATION

The following chapter provides a concrete discrete framework for the implementation of the multi-symplectic, Lagrangian hyperelastic with a MSEM discretisation procedure. The strong form of the partial differential equation system is given firstly in Section 4.1, with the chosen orientation of variables for discretisation in Section 4.2. The discrete weak formulation is given in Section 4.3, and its assembly into a system of equations with boundary conditions (Section 4.4). A generalisation to multiple spatially-connected elements is noted in Subsection 4.4.5. Discrete, linear mappings (pushforward and pullbacks, as previously remarked throughout Chapter 3) are described in Section 4.5. A thorough derivation of the continuous and discrete forms of linear momentum, angular momentum, energy, and mass are given in Section 4.6.

4.1. STRONG FORM

In the previous chapter, we derived the strong form of the hyperelastic problem and its governing equations. Neglecting the gravitational potential term, the resulting strong form in the spatial configuration (as denoted by gradient ∇_0) is:

$$\rho_0 \ddot{\boldsymbol{\varphi}} + \nabla_0 \cdot (\boldsymbol{P}) = \boldsymbol{0} \tag{4.1}$$

where $\boldsymbol{\varphi}$ is the flow map, ρ_0 is the reference density (assumed constant in this thesis), $\boldsymbol{P}$ is the first Piola-Kirchhoff stress tensor, and $\boldsymbol{F} = \nabla_0 \boldsymbol{\varphi}$ is the deformation gradient with Jacobian $J = \det(\boldsymbol{F})$. The above equation can be rewritten to classify and separate the system into *Balance*, *Constitutive*, and *Definition* equations as follows:

$$\begin{cases} \dfrac{\partial \boldsymbol{\pi}}{\partial t} - \nabla_0 \cdot (\boldsymbol{P}) = \boldsymbol{0} & \textit{Balance Equation} \\ \boldsymbol{\pi} = \rho_0 \dfrac{\partial \boldsymbol{\varphi}}{\partial t} & \textit{Constitutive Equation} \\ \boldsymbol{P} = \boldsymbol{F} \cdot \boldsymbol{S}(\boldsymbol{C}) & \textit{Constitutive Equation} \\ \boldsymbol{S} = 2 \frac{\partial W}{\partial \boldsymbol{C}} & \textit{Definition Equation} \\ \boldsymbol{F} = \nabla_0 \boldsymbol{\varphi} & \textit{Definition Equation} \end{cases} \tag{4.2}$$

Recall that the *Constitutive* equations are also where the approximations ($\star$-involved quantities) occur. Here, $\boldsymbol{\pi}$ is the linear momentum density, $\boldsymbol{P}$ is the first Piola-Kirchhoff stress tensor, and $\boldsymbol{S}(\boldsymbol{C})$ is the second Piola-Kirchhoff stress tensor derived from the strain energy function $W(\boldsymbol{C})$ via $\boldsymbol{S} = 2\partial W/\partial \boldsymbol{C}$, where $\boldsymbol{C} = \boldsymbol{F}^T \cdot \boldsymbol{F}$ is the right Cauchy-Green deformation tensor. These four sets of equations respectively represent the local form of momentum balance, the constitutive relationship between momentum $\boldsymbol{\pi}$ and velocity $\dot{\boldsymbol{\varphi}}$, the constitutive relationship for stress $\boldsymbol{P}$ (made generalisable through the strain energy function) [Demoures and Gay-Balmaz, 2022], and the definition of the deformation gradient.

4.2. DISCRETE VARIABLE REPRESENTATION

The discrete variables are associated with specific geometric entities on the primal and dual grids as summarized in Table 4.1, where N denotes the polynomial degree in space and N_t in time. The overbar notation $(\bar{\cdot})$ indicates discrete degrees of freedom (integral quantities), reconstructed using appropriate basis functions.

Each physical quantity is expanded using tensor-product basis functions appropriate to its geometric association. Let $h_i(\xi)$ denote nodal (Lagrange) basis functions, $e_i(\xi)$ edge basis functions, and $\widetilde{e}_i(\xi), \widetilde{h}_i(\xi)$ their dual counterparts,

Table 4.1: Geometric association of physical variables on the primal and dual grids in $\mathbb{R}^3$. "DoFs" refer to *Degrees of Freedom*

Integral Quantities / DOFs	**Geometry**	**Grid**	**Number of DoFs per Element**
$\bar{\boldsymbol{\varphi}}$	Nodes	Primal	$(N_t+1)(N+1)^2$
$\bar{\boldsymbol{F}}$	Spatial Edges	Primal	$2(N_t+1)N(N+1)$
$\bar{\boldsymbol{V}}$	Temporal Edges	Primal	$N_t(N+1)^2$
$\bar{\boldsymbol{\pi}}$	Spatial Faces	Dual	$N_t(N+1)^2$
$\bar{\boldsymbol{P}}$	Spatio-Temporal Faces	Dual	$2(N_t+1)N(N+1)$

as introduced in Section 2.5). The spatial reference coordinates are $(\xi,\eta)\in[-1,1]^2$ and temporal reference coordinate is $\tau\in[-1,1]$ [Mahadev, 2025].

Flow Map $\boldsymbol{\varphi}\in\Lambda^{(0)}(\mathcal{M})$: Associated with primal nodes, expanded as

$$\varphi^h_\alpha(\xi,\eta,\tau)=\sum_{i=0}^{N}\sum_{j=0}^{N}\sum_{k=0}^{N_t}\bar{\varphi}_{\alpha,ijk}\,h_i(\xi)h_j(\eta)h_k(\tau),\quad \alpha\in\{x,y\}. \tag{4.3}$$

Deformation Gradient $\boldsymbol{F}\in\Lambda^{(1)}(\mathcal{M})$: Associated with primal spatial edges, expanded as

$$F^h_{\alpha\beta}(\xi,\eta,\tau)=\sum_{i,j,k}\bar{F}_{\alpha\beta,ijk}\,\psi_{\alpha\beta,i}(\xi)\psi_{\alpha\beta,j}(\eta)h_k(\tau),\quad \alpha,\beta\in\{x,y\}, \tag{4.4}$$

where $\psi_{\alpha\beta,i}=e_i$ if the component differentiates in that direction, else h_i (with summation from 1 to N for edges, 0 to N for nodes).

Velocity $\boldsymbol{V}\in\Lambda^{(1)}(\mathcal{M})$: Associated with primal temporal edges, expanded as

$$V^h_\alpha(\xi,\eta,\tau)=\sum_{i=0}^{N}\sum_{j=0}^{N}\sum_{k=1}^{N_t}\bar{V}_{\alpha,ijk}\,h_i(\xi)h_j(\eta)e_k(\tau),\quad \alpha\in\{x,y\}. \tag{4.5}$$

Momentum $\boldsymbol{\pi}\in\widetilde{\Lambda}^{(2)}(\mathcal{M})$: Associated with dual spatial surfaces, expanded as

$$\pi^h_\alpha(\xi,\eta,\tau)=\sum_{i=1}^{N}\sum_{j=1}^{N}\sum_{k=0}^{N_t}\bar{\pi}_{\alpha,ijk}\,\widetilde{e}_i(\xi)\widetilde{e}_j(\eta)\widetilde{h}_k(\tau),\quad \alpha\in\{x,y\}. \tag{4.6}$$

First Piola-Kirchhoff Stress $\boldsymbol{P}\in\widetilde{\Lambda}^{(2)}(\mathcal{M})$: Associated with dual spatio-temporal surfaces, expanded as

$$P^h_{\alpha\beta}(\xi,\eta,\tau)=\sum_{i,j,k}\bar{P}_{\alpha\beta,ijk}\,\widetilde{\psi}_{\alpha\beta,i}(\xi)\widetilde{\psi}_{\alpha\beta,j}(\eta)\widetilde{e}_k(\tau),\quad \alpha,\beta\in\{x,y\}, \tag{4.7}$$

where $\widetilde{\psi}_{\alpha\beta,i}=\widetilde{h}_i$ if the stress component is perpendicular to that direction, else $\widetilde{e}_i$ (with appropriate summation ranges).

Remark 4.2.1

The summation indices in the discrete expansions reflect the geometric association: edge basis functions e_i have indices from 1 to N (corresponding to N edges between $N+1$ nodes), while nodal basis functions h_i have indices from 0 to N (corresponding to $N+1$ nodes). The dual basis functions $\widetilde{e}_i, \widetilde{h}_i$ follow the same conventions but are orthogonal to their primal counterparts with respect to the L^2 inner product weighted by the discrete Hodge operator.
For the $\mathbb{R}^3$ grid, basis functions are constructed at Gauss-Lobatto-Legendre (GLL) collocation points $\xi = \xi_0, \ldots, \xi_{N+1}$, $\eta = \eta_0, \ldots, \eta_{N+1}$, $\tau = \tau_0, \ldots, \tau_{N_t+1}$ using tensor products of one-dimensional basis functions:

Primal Nodal Basis. $\boldsymbol{\Psi}_0 = h(\xi)\otimes h(\eta)\otimes h(\tau)$ belongs to $\Lambda_h^{(0)}(\mathcal{B}\times T)\subset H^1(\mathcal{B}\times T)$, with index expansion $\boldsymbol{\Psi}_0 = h_i(\xi)h_j(\eta)h_k(\tau)$ for $i,j = 0,\ldots,N$, $k = 0,\ldots,N_t$.

Primal Edge Basis. The edge basis belongs to $\Lambda_h^{(1)}(\mathcal{B}\times T)\subset H(\text{curl};\mathcal{B}\times T)$:

$$\boldsymbol{\Psi}_1 = \begin{bmatrix} e(\xi)\otimes h(\eta)\otimes h(\tau) & 0 & 0 \\ 0 & h(\xi)\otimes e(\eta)\otimes h(\tau) & 0 \\ 0 & 0 & h(\xi)\otimes h(\eta)\otimes e(\tau) \end{bmatrix}, \tag{4.8}$$

yielding $\boldsymbol{\Psi}_1^{\xi} = e_i(\xi)h_j(\eta)h_k(\tau)$ for $i = 1,\ldots,N$, $j = 0,\ldots,N$, $k = 0,\ldots,N_t$ (and analogously for η and τ directions with appropriate index ranges).

Dual Surface Basis. The dual surface basis belongs to $\widetilde{\Lambda}_h^{(2)}(\mathcal{B}\times T)\subset \widetilde{H}(\text{grad};\mathcal{B}\times T)$:

$$\widetilde{\boldsymbol{\Psi}}_2 = \begin{bmatrix} \widetilde{h}(\xi)\otimes \widetilde{e}(\eta)\otimes \widetilde{e}(\tau) & 0 & 0 \\ 0 & \widetilde{e}(\xi)\otimes \widetilde{h}(\eta)\otimes \widetilde{e}(\tau) & 0 \\ 0 & 0 & \widetilde{e}(\xi)\otimes \widetilde{e}(\eta)\otimes \widetilde{h}(\tau) \end{bmatrix} \tag{4.9}$$

with components $\widetilde{\boldsymbol{\Psi}}_2^{\xi} = \widetilde{h}_i(\xi)\widetilde{e}_j(\eta)\widetilde{e}_k(\tau)$ (and similarly for other directions, following the pattern: nodal basis perpendicular to the surface, edge basis parallel to it).

4.3. WEAK FORMULATION

On a continuous domain, the momentum balance equation for hyperelastic materials, in terms of differential bundle forms, is

$$\mathrm{d}_t\boldsymbol{\pi}^{(2)} - \mathrm{d}\boldsymbol{P}^{(2)} = 0, \tag{4.10}$$

where d_t and d denote temporal and spatial components of the exterior derivative acting as divergence operators. Here, $\boldsymbol{\pi}^{(2)} \in \widetilde{\Lambda}^{(2)}(\mathcal{M})$ is the momentum 2-form and $\boldsymbol{P}^{(2)} \in \widetilde{\Lambda}^{(2)}(\mathcal{M})$ is the first Piola-Kirchhoff stress 2-form.

Testing the strong form with the test form $\eta^{(0)} \in \Lambda^{(0)}(\mathcal{M})$ (Hodge dual of an arbitrary test form $\star\eta^{(3)} \in \widetilde{\Lambda}^{(3)}(\mathcal{M})$) and integrating over $\mathcal{M} = \Omega_0 \times [0,T]$ yields:

$$\int_{\mathcal{M}} \mathrm{d}_t\boldsymbol{\pi}^{(2)} \wedge \eta^{(0)} - \int_{\mathcal{M}} \mathrm{d}\boldsymbol{P}^{(2)} \wedge \eta^{(0)} = 0, \quad \forall\,\eta^{(0)} \in \Lambda^{(0)}(\mathcal{M}) \tag{4.11}$$

4.3.1. DISCRETE WEAK FORMULATION

In the discrete setting, choosing test function $\eta^{(0)} \in H^1(\Omega_0 \times T)$ and applying integration by parts with the divergence theorem gives:

$$-\int_{\mathcal{M}\times T} \boldsymbol{\pi}\cdot \mathrm{d}\eta^{(0)} + \int_{\partial[\mathcal{M}\times T]} (\boldsymbol{\pi}\cdot\mathbf{n}_t)\,\eta^{(0)} + \int_{\mathcal{M}\times T} \boldsymbol{P}\,\nabla_0\eta^{(0)} = 0, \tag{4.12}$$

where $\mathbf{n}_t$ is the outward temporal normal. Integration by parts transfers derivatives to test functions, yielding the weak form in inner product notation:

$$-\left\langle \boldsymbol{\pi}, \mathrm{d}_t\eta^{(0)} \right\rangle_{\mathcal{M}\times T} + \left\langle \boldsymbol{\pi}\cdot\mathbf{n}_t, \eta^{(0)} \right\rangle_{\partial[\mathcal{M}\times T]} + \left\langle \boldsymbol{P}, \nabla_0\eta^{(0)} \right\rangle_{\mathcal{M}\times T} = 0. \tag{4.13}$$

4.3.2. DISCRETE MOMENTUM-VELOCITY CONSTITUTIVE RELATION

The momentum-velocity constitutive relation is tested with $\widetilde{\mathbf{v}} \in (H^1 \times L^2; \Omega_0 \times T)$ (a mixed function space, with H^1 in space and L^2 in time):

$$\int_{\mathcal{M}} \boldsymbol{\pi}\cdot\widetilde{\mathbf{v}}\,d\mathcal{M} - \int_{\mathcal{M}} \rho_0 \frac{\partial\boldsymbol{\varphi}}{\partial t}\cdot\widetilde{\mathbf{v}}\,d\mathcal{M} = 0, \tag{4.14}$$

which discretizes component-wise to:

$$\bar{\boldsymbol{\pi}}_\alpha = \mathbb{H}_{\rho_0}\mathbb{E}_t^{(1,0)}\bar{\boldsymbol{\varphi}}_\alpha, \quad \alpha \in \{x,y\} \tag{4.15}$$

where $\mathbb{H}_{\rho_0}$ is the (constant) density-weighted Hodge matrix mapping primal temporal edge DOFs (velocity) to dual spatial surface DOFs (momentum).

4.3.3. DISCRETE MATERIAL LAW

Substituting discrete expansions and using orthogonality of primal/dual basis functions, the discrete momentum balance for arbitrary test functions $\tilde{\boldsymbol{\phi}}_\alpha$ ($\alpha \in \{x,y\}$) involves the full tensor structure of the stress operator. Unlike scalar-valued forms, the hyperelastic formulation requires contracting *all* components of the stress tensor $\boldsymbol{P}$, resulting in both diagonal and off-diagonal coupling terms.

For the x-momentum equation:

$$\begin{aligned}\mathbb{E}_t^{(1,0)^T}\bar{\boldsymbol{\pi}}_x + \mathbb{N}_\pi\bar{\boldsymbol{\pi}}_x &+ \left(\mathbb{E}_x^{(1,0)^T}\mathbb{H}_{11}^{xy}\mathbb{E}_y^{(1,0)} - \mathbb{E}_y^{(1,0)^T}\mathbb{H}_{11}^{yx}\mathbb{E}_x^{(1,0)}\right)\bar{\boldsymbol{\varphi}}_x \\ &+ \left(\mathbb{E}_x^{(1,0)^T}\mathbb{H}_{12}^{xy}\mathbb{E}_y^{(1,0)} - \mathbb{E}_y^{(1,0)^T}\mathbb{H}_{12}^{yx}\mathbb{E}_x^{(1,0)}\right)\bar{\boldsymbol{\varphi}}_y = 0.\end{aligned} \tag{4.16}$$

For the y-momentum equation:

$$\begin{aligned}\mathbb{E}_t^{(1,0)^T}\bar{\boldsymbol{\pi}}_y + \mathbb{N}_\pi\bar{\boldsymbol{\pi}}_y &+ \left(\mathbb{E}_x^{(1,0)^T}\mathbb{H}_{12}^{xy}\mathbb{E}_y^{(1,0)} - \mathbb{E}_y^{(1,0)^T}\mathbb{H}_{12}^{yx}\mathbb{E}_x^{(1,0)}\right)\bar{\boldsymbol{\varphi}}_x \\ &+ \left(\mathbb{E}_x^{(1,0)^T}\mathbb{H}_{22}^{xy}\mathbb{E}_y^{(1,0)} - \mathbb{E}_y^{(1,0)^T}\mathbb{H}_{22}^{yx}\mathbb{E}_x^{(1,0)}\right)\bar{\boldsymbol{\varphi}}_y = 0.\end{aligned} \tag{4.17}$$

where $\mathbb{N}_\pi$ is the connectivity matrix mapping temporal boundary DOFs (trace matrix), and $\mathbb{H}_{ij}^{xy}$ are the components of the tensor-valued stress Hodge operator. Each momentum equation contains four terms: two diagonal terms ($\mathbb{H}_{11}$ for x-equation, $\mathbb{H}_{22}$ for y-equation) coupling each flow component to itself, and two off-diagonal terms ($\mathbb{H}_{12}$) providing cross-coupling between x and y components through the stress tensor structure. Defining stress operators for compact notation:

$$\mathbb{D}^{xx} = -\mathbb{E}_x^{(1,0)^T}\mathbb{H}_{12}^{xy}\mathbb{E}_y^{(1,0)} + \mathbb{E}_y^{(1,0)^T}\mathbb{H}_{12}^{yx}\mathbb{E}_x^{(1,0)}, \qquad \mathbb{D}^{xy} = \mathbb{E}_x^{(1,0)^T}\mathbb{H}_{11}^{xy}\mathbb{E}_y^{(1,0)} - \mathbb{E}_y^{(1,0)^T}\mathbb{H}_{11}^{yx}\mathbb{E}_x^{(1,0)}, \tag{4.18}$$

$$\mathbb{D}^{yx} = -\mathbb{E}_x^{(1,0)^T}\mathbb{H}_{22}^{xy}\mathbb{E}_y^{(1,0)} + \mathbb{E}_y^{(1,0)^T}\mathbb{H}_{22}^{yx}\mathbb{E}_x^{(1,0)}, \qquad \mathbb{D}^{yy} = \mathbb{E}_x^{(1,0)^T}\mathbb{H}_{12}^{xy}\mathbb{E}_y^{(1,0)} - \mathbb{E}_y^{(1,0)^T}\mathbb{H}_{12}^{yx}\mathbb{E}_x^{(1,0)}, \tag{4.19}$$

the final system can be written more compactly as:

$$\mathbb{E}_t^{(1,0)^T}\bar{\boldsymbol{\pi}}_x + \mathbb{N}_\pi\bar{\boldsymbol{\pi}}_x - \mathbb{D}^{xy}\bar{\boldsymbol{\varphi}}_x - \mathbb{D}^{xx}\bar{\boldsymbol{\varphi}}_y = 0, \qquad \mathbb{E}_t^{(1,0)^T}\bar{\boldsymbol{\pi}}_y + \mathbb{N}_\pi\bar{\boldsymbol{\pi}}_y - \mathbb{D}^{yy}\bar{\boldsymbol{\varphi}}_y - \mathbb{D}^{yx}\bar{\boldsymbol{\varphi}}_x = 0. \tag{4.20}$$

4.3.4. TENSOR-VALUED STRESS HODGE OPERATOR

For hyperelastic materials, the first Piola-Kirchhoff stress $\boldsymbol{P}$ is computed directly from the deformation gradient via:

$$\boldsymbol{P} = \boldsymbol{F}\cdot\boldsymbol{S}(\boldsymbol{C}), \quad \boldsymbol{C} = \boldsymbol{F}^T\cdot\boldsymbol{F}, \quad \boldsymbol{S} = 2\frac{\partial W}{\partial \boldsymbol{C}}. \tag{4.21}$$

where $\boldsymbol{S}$ is the second Piola-Kirchhoff stress derived from the strain energy function $W(\boldsymbol{C})$. Again, when physical geometry differs from computational domain, a pullback transformation is applied:

$$\boldsymbol{P} = |\det\boldsymbol{F}_0|\,\mathbf{P}_{\Omega_0}\cdot\boldsymbol{F}_0^{-T}, \tag{4.22}$$

and $\boldsymbol{F}_0^{-T}$ transforms the stress components from reference configuration back to the physical configuration, and $|\det\boldsymbol{F}_0|$ accounts for volume scaling. The stress-weighted Hodge operator is a tensor-valued operator encompassing the stress state at integration points. To account for its bundle-valued nature, each component of $\boldsymbol{P}$ is contracted with basis function products:

$$\mathbb{H}_{ij}^{xy} = \int_{\mathcal{M}} P_{ij}\left[\boldsymbol{\Psi}^\xi\right]^T\boldsymbol{\Psi}^\eta\, d\mathcal{M}, \tag{4.23}$$

with a similar construction for $\mathbb{H}_{ij}^{yx}$ (swapping ξ and η basis functions). Here, P_{ij} denotes the (i,j) component of the stress tensor, and the integration is performed over all space-time quadrature points. The stress tensor $\boldsymbol{P}$ depends non-linearly on the flow map degrees of freedom $\bar{\boldsymbol{\varphi}}$ through the deformation gradient, necessitating iterative solution methods. This formulation thus directly uses the first Piola-Kirchhoff stress $\boldsymbol{P}$, avoiding intermediate Cauchy stress computation. The discrete operators $\mathbb{D}^{xx}, \mathbb{D}^{xy}, \mathbb{D}^{yx}, \mathbb{D}^{yy}$ encode non-linear material response, capturing the full tensorial nature of the hyperelastic constitutive relation.

Remark 4.3.1: Computational Cost and Non-Linearity

The evaluation of the tensor-valued stress Hodge operators $\mathbb{H}^{xy}_{ij}$ and $\mathbb{H}^{yx}_{ij}$ constitutes the primary computational expense in the hyperelastic formulation and is the source of non-linearity in the discrete system. At each sub-iteration, these operators must be recomputed by evaluating $\boldsymbol{P}$ at all space-time quadrature points, requiring the calculation of deformation gradients $\boldsymbol{F}$ from current flow map degrees of freedom, computation of the right Cauchy-Green tensor $\boldsymbol{C} = \boldsymbol{F}^T\boldsymbol{F}$, evaluation of the strain energy derivative $\partial W/\partial \boldsymbol{C}$ for the specific material model, and assembly of the first Piola-Kirchhoff stress via (4.21). For high-order spectral elements with $(p+1)^2$ spatial quadrature points per element and n_t temporal quadrature points, this requires $\mathcal{O}(n_e(p+1)^2 n_t)$ stress evaluations per iteration, where n_e is the number of spatial elements. The non-linearity arises because $\boldsymbol{P}$ depends on $\bar{\boldsymbol{\varphi}}$ through the composition $\boldsymbol{P}(\boldsymbol{F}(\bar{\boldsymbol{\varphi}}))$, making the discrete operators $\mathbb{D}^{\alpha\beta}$ configuration-dependent. This configuration-dependence necessitates iterative solution strategies and reassembly of the Jacobian matrix at *each* iteration, distinguishing from linear elasticity where the stress operators can be precomputed.

4.4. Boundary Conditions and System Assembly

4.4.1. Initial Conditions and Temporal Coupling

The discrete system derived in Section 4.3 must be augmented to handle initial conditions and temporal continuity between successive "time-slabs", i.e. spatial domains extruded in the time direction. As a result, the system being solved can be noted as a "time slab", whereby coupling between the slabs allow for variational integration in local space-time. At the initial time $t = t_0$, both the flow map $\boldsymbol{\varphi}(\mathbf{X}, t_0) = \mathbf{X}$ and the initial momentum $\boldsymbol{\pi}(\mathbf{X}, t_0) = \boldsymbol{\pi}_0(\mathbf{X})$ are prescribed. The initial momentum enters the system by moving the corresponding degrees of freedom to the right-hand side. Let $\bar{\boldsymbol{\pi}}^{(0)}_\alpha$ denote the initial momentum in direction $\alpha \in \{x, y\}$ at time t_0. The columns of the system matrix corresponding to these known values are extracted and multiplied by $\bar{\boldsymbol{\pi}}^{(0)}_\alpha$, then moved to the right-hand side. The modified right-hand side becomes:

$$\mathbf{f} = \mathbf{f}_0 - \sum_{\alpha\in\{x,y\}} \mathbb{A}^{\text{ic}}_\alpha \bar{\boldsymbol{\pi}}^{(0)}_\alpha, \tag{4.24}$$

where $\mathbb{A}^{\text{ic}}_\alpha$ denotes the column block of the original system matrix associated with initial momentum in direction α, and $\mathbf{f}_0$ represents other forcing terms (such as traction). The initial flow map $\boldsymbol{\varphi}(\mathbf{X}, t_0) = \mathbf{X}$ is prescribed by directly setting the corresponding entries in the right-hand side. For each spatial node with reference coordinates (X_i, Y_i), we impose:

$$\mathbf{f}^{(i,0)}_{\varphi_x} = X_i \qquad \mathbf{f}^{(i,0)}_{\varphi_y} = Y_i \tag{4.25}$$

where the superscript $(i,0)$ indicates node i at time level t_0.

Time-Slab Continuity

The space-time discretisation treats each temporal interval $[t_s, t_{s+1}]$ as an independent spectral element. To maintain continuity of the solution across time slabs, Lagrange multipliers $\boldsymbol{\mu}$ enforce matching conditions between the final state of slab s and the initial state of slab $s+1$. Let $\boldsymbol{\varphi}^{(s,N_t)}$ denote the flow map at the final temporal node of slab s, and $\boldsymbol{\varphi}^{(s+1,0)}$ the flow map at the initial node of slab $s+1$. The continuity constraint in weak form is:

$$\int_{\Omega_0} \boldsymbol{\mu} \cdot \left[\boldsymbol{\varphi}^{(s,N_t)} - \boldsymbol{\varphi}^{(s+1,0)}\right] dV_0 = 0 \tag{4.26}$$

In the discrete setting, this introduces purely topological connectivity matrices $\mathbb{N}^{\text{start}}_\varphi$ and $\mathbb{N}^{\text{end}}_\varphi$ that couple the flow map degrees of freedom at temporal boundaries. The augmented system includes rows enforcing:

$$\mathbb{N}^{\text{start}}_\varphi \bar{\boldsymbol{\varphi}}^{(s+1)}_\alpha = \mathbb{N}^{\text{end}}_\varphi \bar{\boldsymbol{\varphi}}^{(s)}_\alpha, \quad \alpha \in \{x, y\} \tag{4.27}$$

Similarly, momentum continuity is enforced via:

$$\mathbb{N}^{\text{start}}_\pi \bar{\boldsymbol{\pi}}^{(s+1)}_\alpha = \mathbb{N}^{\text{end}}_\pi \bar{\boldsymbol{\pi}}^{(s)}_\alpha, \quad \alpha \in \{x, y\} \tag{4.28}$$

4.4.2. Spatial Boundary Conditions

Spatial boundary conditions are imposed on the domain boundary $\partial\Omega_0$, which is partitioned into strongly prescribed (essential) and natural boundaries: $\partial\Omega_0 = \Gamma_D \cup \Gamma_N$ with $\Gamma_D \cap \Gamma_N = \emptyset$.

Natural Boundary Conditions

On the natural boundary Γ_N, prescribed tractions $\mathbf{t}_N = \boldsymbol{P} \cdot \mathbf{n}$ enter the weak form as:

$$\int_{\Gamma_N \times [0,T]} \mathbf{t}_N \cdot \widetilde{\boldsymbol{\phi}}\, d(\partial\mathcal{M}) \tag{4.29}$$

This contribution is added directly to the right-hand side. The discrete traction force at boundary nodes is computed via quadrature:

$$\mathbf{F}_N = \int_{\Gamma_N \times [0,T]} \mathbf{t}_N \, d(\partial\mathcal{M}) \approx \sum_{q \in \mathcal{Q}_N} \mathbf{t}_N(\mathbf{X}_q, t_q)\omega_q \tag{4.30}$$

where $\mathcal{Q}_N$ denotes the set of quadrature points on Γ_N, and ω_q are the corresponding weights including both spatial and temporal measures. The traction force $\mathbf{F}_N$ is distributed to the flow map equation rows corresponding to boundary nodes:

$$\mathbf{f}_{\bar{\boldsymbol{\varphi}}} \leftarrow \mathbf{f}_{\bar{\boldsymbol{\varphi}}} + \mathbf{F}_N \tag{4.31}$$

STRONGLY-PRESCRIBED BOUNDARY CONDITIONS VIA LAGRANGE MULTIPLIERS

On the strongly-prescribed boundary Γ_D, the flow map is prescribed as $\boldsymbol{\varphi}|_{\Gamma_D} = \boldsymbol{\varphi}_D$. Rather than eliminating constrained degrees of freedom, we enforce this condition weakly using Lagrange multipliers $\boldsymbol{\lambda}$. This approach preserves the system structure and allows computation of reaction forces. The constrained weak form augments equation (4.13) with:

$$\int_{\Gamma_D \times [0,T]} \boldsymbol{\lambda} \cdot (\boldsymbol{\varphi} - \boldsymbol{\varphi}_D) \, d(\partial\mathcal{M}) = 0. \tag{4.32}$$

Let Γ_D consist of n_D spatial nodes. For each direction $\alpha \in \{x, y\}$ and each time level $k = 1, \ldots, N_t$ (excluding the initial time $k = 0$ which is already prescribed), we enforce:

$$\bar{\boldsymbol{\varphi}}_{\alpha}^{(i,k)} = \bar{\boldsymbol{\varphi}}_{\alpha,D}^{(i,k)}, \quad \forall i \in \Gamma_D \tag{4.33}$$

In implementation, the prescribed values on Γ_D are often held fixed relative to their initial configuration. For example, to fix the west boundary ($\xi = -1$), we require $\bar{\boldsymbol{\varphi}}_{\alpha}^{(i,k)} = \bar{\boldsymbol{\varphi}}_{\alpha}^{(i,0)}$ for all $k > 0$ and all i on the west edge.The discrete constraint matrix $\mathbb{B} \in \mathbb{R}^{n_\lambda \times n_u}$ encodes these conditions, where $n_\lambda = 2n_D(N_t - 1)$ is the number of Lagrange multipliers (two directions, n_D nodes, $N_t - 1$ time levels after initial time), and n_u is the dimension of the reduced system after moving initial conditions to the right-hand side. The constraint takes the form:

$$\mathbb{B}\mathbf{u} = \mathbf{g}, \tag{4.34}$$

where $\mathbf{u}$ contains the primary unknowns and $\mathbf{g}$ specifies the constraint values. For the common case of homogeneous strongly-prescribed conditions (no displacement from initial position), we have:

$$\bar{\boldsymbol{\varphi}}_{\alpha}^{(i,k)} - \bar{\boldsymbol{\varphi}}_{\alpha}^{(i,0)} = 0, \quad \forall i \in \Gamma_D, k = 1, \ldots, N_t \tag{4.35}$$

which gives $\mathbf{g} = \mathbf{0}$.

4.4.3. BOUNDARY AUGMENTED SADDLE-POINT SYSTEM

Incorporating spatial strongly-prescribed constraints via Lagrange multipliers yields the saddle-point system:

$$\begin{bmatrix} \mathbb{A} & \mathbb{B}^T \\ \mathbb{B} & \mathbf{0} \end{bmatrix} \begin{bmatrix} \mathbf{u} \\ \boldsymbol{\lambda} \end{bmatrix} = \begin{bmatrix} \mathbf{f} \\ \mathbf{g} \end{bmatrix} \tag{4.36}$$

where $\mathbb{A} \in \mathbb{R}^{n_u \times n_u}$ is the base system matrix (after removing initial condition columns), $\mathbf{u} \in \mathbb{R}^{n_u}$ contains the primary unknowns $[\bar{\boldsymbol{\pi}}_x, \bar{\boldsymbol{\pi}}_y, \bar{\boldsymbol{\varphi}}_x, \bar{\boldsymbol{\varphi}}_y]^T$, and $\boldsymbol{\lambda} \in \mathbb{R}^{n_\lambda}$ (n_λ as the number of primal degrees of freedom to be constrained) contains the Lagrange multipliers enforcing strong boundary conditions. The base system matrix $\mathbb{A}$ has the block structure:

$$\mathbb{A} = \begin{bmatrix} \mathbb{H}_{\rho_0}^{-1} & \mathbf{0} & -\mathbb{E}_t^{(1,0)} & \mathbf{0} \\ \mathbf{0} & \mathbb{H}_{\rho_0}^{-1} & \mathbf{0} & -\mathbb{E}_t^{(1,0)} \\ \mathbb{E}_t^{(1,0)^T} & \mathbf{0} & \mathbb{D}^{xx} & \mathbb{D}^{xy} \\ \mathbf{0} & \mathbb{E}_t^{(1,0)^T} & \mathbb{D}^{yx} & \mathbb{D}^{yy} \end{bmatrix} \tag{4.37}$$

corresponding to the discrete weak forms from equations (4.15) and (4.16)-(4.17). The right-hand side $\mathbf{f}$ includes contributions from initial conditions (4.24), initial flow map (4.25), and natural boundary tractions (4.31).

4.4.4. COMPLETE SYSTEM MATRIX STRUCTURE

For a single time slab with temporal coupling and spatial strongly-prescribed constraints, the system before removing initial condition columns takes the form:

$$\begin{bmatrix} \mathbb{H}_{\rho 0}^{-1} & \mathbf{0} & -\mathbb{E}_t^{(1,0)} & \mathbf{0} & \mathbf{0} & \mathbf{0} & \mathbf{0} & \mathbf{0} \\ \mathbf{0} & \mathbb{H}_{\rho 0}^{-1} & \mathbf{0} & -\mathbb{E}_t^{(1,0)} & \mathbf{0} & \mathbf{0} & \mathbf{0} & \mathbf{0} \\ \mathbb{E}_t^{(1,0)^T} & \mathbf{0} & \mathbb{D}^{xx} & \mathbb{D}^{xy} & \mathbf{0} & \mathbb{N}_\pi^0 & \mathbf{0} & \mathbb{N}_\pi^f \\ \mathbf{0} & \mathbb{E}_t^{(1,0)^T} & \mathbb{D}^{yx} & \mathbb{D}^{yy} & \mathbb{N}_\pi^0 & \mathbf{0} & \mathbb{N}_\pi^f & \mathbf{0} \\ \mathbf{0} & \mathbf{0} & \mathbb{N}_\varphi & \mathbf{0} & \mathbf{0} & \mathbf{0} & \mathbf{0} & \mathbf{0} \\ \mathbf{0} & \mathbf{0} & \mathbf{0} & \mathbb{N}_\varphi & \mathbf{0} & \mathbf{0} & \mathbf{0} & \mathbf{0} \end{bmatrix} \begin{bmatrix} \bar{\boldsymbol{\pi}}_x \\ \bar{\boldsymbol{\pi}}_y \\ \bar{\boldsymbol{\varphi}}_x \\ \bar{\boldsymbol{\varphi}}_y \\ \bar{\boldsymbol{\pi}}_x^0 \\ \bar{\boldsymbol{\pi}}_x^f \\ \bar{\boldsymbol{\pi}}_y^0 \\ \bar{\boldsymbol{\pi}}_y^f \end{bmatrix} = \begin{bmatrix} \mathbf{0} \\ \mathbf{0} \\ \mathbf{0} \\ \mathbf{0} \\ \bar{\boldsymbol{\varphi}}_x^0 \\ \bar{\boldsymbol{\varphi}}_y^0 \end{bmatrix} \tag{4.38}$$

where $\bar{\boldsymbol{\pi}}_\alpha \in \mathbb{R}^{n_\text{mom}}$ are the momentum edge degrees of freedom, $\bar{\boldsymbol{\varphi}}_\alpha \in \mathbb{R}^{n_\text{flow}}$ are the flow map nodal degrees of freedom, $\bar{\boldsymbol{\pi}}_\alpha^0, \bar{\boldsymbol{\pi}}_\alpha^f \in \mathbb{R}^{n_\text{space}}$ represent initial and final momentum states, and $\bar{\boldsymbol{\varphi}}_\alpha^0 \in \mathbb{R}^{n_\text{space}}$ contains the flow map values from the previous time slab. The operator $\mathbb{N}_\varphi \in \mathbb{R}^{n_\text{space} \times n_\text{flow}}$ extracts the initial temporal slice of the flow map, while $\mathbb{N}_\pi^0, \mathbb{N}_\pi^f \in \mathbb{R}^{n_\text{flow} \times n_\text{space}}$ embed initial and final momentum values into the flowmap equation rows.

The columns corresponding to $\bar{\boldsymbol{\pi}}_\alpha^0$ are eliminated by moving their contributions to the right-hand side, yielding the condensed system:

$$\begin{bmatrix} \mathbb{H}_{\rho 0}^{-1} & \mathbf{0} & -\mathbb{E}_t^{(1,0)} & \mathbf{0} & \mathbf{0} & \mathbf{0} \\ \mathbf{0} & \mathbb{H}_{\rho 0}^{-1} & \mathbf{0} & -\mathbb{E}_t^{(1,0)} & \mathbf{0} & \mathbf{0} \\ \mathbb{E}_t^{(1,0)^T} & \mathbf{0} & \mathbb{D}^{xx} & \mathbb{D}^{xy} & \mathbb{N}_\pi^f & \mathbf{0} \\ \mathbf{0} & \mathbb{E}_t^{(1,0)^T} & \mathbb{D}^{yx} & \mathbb{D}^{yy} & \mathbf{0} & \mathbb{N}_\pi^f \\ \mathbf{0} & \mathbf{0} & \mathbb{N}_\varphi & \mathbf{0} & \mathbf{0} & \mathbf{0} \\ \mathbf{0} & \mathbf{0} & \mathbf{0} & \mathbb{N}_\varphi & \mathbf{0} & \mathbf{0} \end{bmatrix} \begin{bmatrix} \bar{\boldsymbol{\pi}}_x \\ \bar{\boldsymbol{\pi}}_y \\ \bar{\boldsymbol{\varphi}}_x \\ \bar{\boldsymbol{\varphi}}_y \\ \bar{\boldsymbol{\pi}}_x^f \\ \bar{\boldsymbol{\pi}}_y^f \end{bmatrix} = \begin{bmatrix} \mathbf{0} \\ \mathbf{0} \\ -\mathbb{N}_\pi^0 \bar{\boldsymbol{\pi}}_x^0 + \mathbf{F}_{\text{trac},x} \\ -\mathbb{N}_\pi^0 \bar{\boldsymbol{\pi}}_y^0 + \mathbf{F}_{\text{trac},y} \\ \bar{\boldsymbol{\varphi}}_x^0 \\ \bar{\boldsymbol{\varphi}}_y^0 \end{bmatrix} \tag{4.39}$$

where $\mathbf{F}_{\text{trac},\alpha} \in \mathbb{R}^{n_\text{flow}}$ contains the integrated traction forces applied to the boundary.

For example, to incorporate spatial strongly-prescribed boundary conditions on the western boundary, this system is augmented with Lagrange multipliers via a saddle-point formulation. The constraint matrices $\mathbb{B}_x, \mathbb{B}_y \in \mathbb{R}^{n_\text{constraints} \times n_\text{flow}}$ enforce that the flow map at constrained nodes remains fixed across temporal slices within the slab. For n_time temporal nodes and n_west constrained spatial nodes, there are $n_\text{constraints} = (n_\text{time} - 1) \times n_\text{west}$ constraints per direction. The constraints enforce:

$$\mathbb{B}_\alpha \bar{\boldsymbol{\varphi}}_\alpha = \mathbf{0} \quad \Leftrightarrow \quad \bar{\varphi}_{\alpha,i}^k - \bar{\varphi}_{\alpha,i}^0 = 0 \quad \forall i \in \mathcal{I}_\text{west}, \quad k = 1, \ldots, n_\text{time} - 1 \tag{4.40}$$

where $\mathcal{I}_\text{west}$ denotes the set of west boundary node indices. The augmented saddle-point system becomes:

$$\begin{bmatrix} \mathbb{H}_{\rho 0}^{-1} & \mathbf{0} & -\mathbb{E}_t^{(1,0)} & \mathbf{0} & \mathbf{0} & \mathbf{0} & \mathbf{0} & \mathbf{0} \\ \mathbf{0} & \mathbb{H}_{\rho 0}^{-1} & \mathbf{0} & -\mathbb{E}_t^{(1,0)} & \mathbf{0} & \mathbf{0} & \mathbf{0} & \mathbf{0} \\ \mathbb{E}_t^{(1,0)^T} & \mathbf{0} & \mathbb{D}^{xx} & \mathbb{D}^{xy} & \mathbb{N}_\pi^f & \mathbf{0} & \mathbb{B}_x^T & \mathbf{0} \\ \mathbf{0} & \mathbb{E}_t^{(1,0)^T} & \mathbb{D}^{yx} & \mathbb{D}^{yy} & \mathbf{0} & \mathbb{N}_\pi^f & \mathbf{0} & \mathbb{B}_y^T \\ \mathbf{0} & \mathbf{0} & \mathbb{N}_\varphi & \mathbf{0} & \mathbf{0} & \mathbf{0} & \mathbf{0} & \mathbf{0} \\ \mathbf{0} & \mathbf{0} & \mathbf{0} & \mathbb{N}_\varphi & \mathbf{0} & \mathbf{0} & \mathbf{0} & \mathbf{0} \\ \mathbf{0} & \mathbf{0} & \mathbb{B}_x & \mathbf{0} & \mathbf{0} & \mathbf{0} & \mathbf{0} & \mathbf{0} \\ \mathbf{0} & \mathbf{0} & \mathbf{0} & \mathbb{B}_y & \mathbf{0} & \mathbf{0} & \mathbf{0} & \mathbf{0} \end{bmatrix} \begin{bmatrix} \bar{\boldsymbol{\pi}}_x \\ \bar{\boldsymbol{\pi}}_y \\ \bar{\boldsymbol{\varphi}}_x \\ \bar{\boldsymbol{\varphi}}_y \\ \bar{\boldsymbol{\pi}}_x^f \\ \bar{\boldsymbol{\pi}}_y^f \\ \boldsymbol{\lambda}_x \\ \boldsymbol{\lambda}_y \end{bmatrix} = \begin{bmatrix} \mathbf{0} \\ \mathbf{0} \\ -\mathbb{N}_\pi^0 \bar{\boldsymbol{\pi}}_x^0 + \mathbf{F}_{\text{trac},x} \\ -\mathbb{N}_\pi^0 \bar{\boldsymbol{\pi}}_y^0 + \mathbf{F}_{\text{trac},y} \\ \bar{\boldsymbol{\varphi}}_x^0 \\ \bar{\boldsymbol{\varphi}}_y^0 \\ \mathbf{0} \\ \mathbf{0} \end{bmatrix} \tag{4.41}$$

where $\boldsymbol{\lambda}_x, \boldsymbol{\lambda}_y \in \mathbb{R}^{n_\text{constraints}}$ are the Lagrange multipliers enforcing spatial fixity. The zero vectors on the right-hand side of the constraint equations enforce homogeneous strongly-prescribed conditions. The Lagrange multipliers $\boldsymbol{\lambda}_\alpha$ represent the reaction forces at spatially constrained boundaries required to maintain fixity. Upon solving (4.41), these multipliers provide diagnostic information about the force distribution at boundaries. This complete system is solved using direct factorization methods at each non-linear iteration step, with the stress-divergence operators $\mathbb{D}^{\alpha\beta}$ updated based on the current deformation state as described in Section 4.3. Table 4.2 also gives an overview of some notable properties that are important for numerical implementation.

Table 4.2: Properties of operators in the discrete system (4.41). Linear indicates that the operator does not need to be updated each inner iteration.
* : So as long the material constitutive equation can be assumed to not depend on local density, e.g. as relevant in porous media modelling.

Operator	Structure	Nature
$\mathbb{H}_{\rho_0}^{-1}$	Dense	Linear*
$\mathbb{E}_t^{(1,0)}$	Sparse	Linear
$\mathbb{D}^{xx}, \mathbb{D}^{xy}, \mathbb{D}^{yx}, \mathbb{D}^{yy}$	Dense	Non-linear
$\mathbb{N}_\pi^f, \mathbb{N}_\pi^0$	Sparse	Linear
$\mathbb{N}_\varphi$	Sparse	Linear
$\mathbb{B}_x, \mathbb{B}_y$	Sparse	Linear

4.4.5. SPATIAL HYBRIDIZATION FOR MULTI-ELEMENT DOMAINS

The formulation presented thus far describes the discrete system for a single spectral element in space coupled with a temporal discretisation. For problems defined on domains that cannot be efficiently represented by a single element, the spatial domain Ω_0 must be decomposed into multiple non-overlapping spectral elements $\Omega_0 = \bigcup_{e=1}^{n_\text{elem}} \Omega_0^e$. The resulting multi-element discretisation requires enforcing continuity of the flow map and momentum across inter-element boundaries,

INTERFACE CONTINUITY VIA LAGRANGE MULTIPLIERS

At inter-element boundaries, the flow map degrees of freedom from adjacent elements must be constrained for continuity of the solution. Consider two adjacent elements $\Omega_0^{(e)}$ and $\Omega_0^{(e')}$ sharing a common interface $\Gamma_\text{int}^{(e,e')}$. Let $\mathcal{I}_\text{int}^{(e,e')}$ denote the set of node indices on this interface. For each shared node $i \in \mathcal{I}_\text{int}^{(e,e')}$, the flow map degrees of freedom from both elements must coincide. This continuity constraint is enforced weakly via interface Lagrange multipliers $\boldsymbol{\mu}_{\text{int},\alpha}^{(e,e')}$. In discrete form, the interface continuity matrices $\mathbb{C}_\alpha^{(e,e')} \in \mathbb{R}^{n_\text{int} \times n_\text{flow}}$ enforce:

$$\mathbb{C}_\alpha^{(e)} \bar{\boldsymbol{\varphi}}_\alpha^{(e)} - \mathbb{C}_\alpha^{(e')} \bar{\boldsymbol{\varphi}}_\alpha^{(e')} = \mathbf{0}, \quad \alpha \in \{x, y\} \tag{4.42}$$

where $\mathbb{C}_\alpha^{(e)}$ extracts the interface degrees of freedom from element e, $\bar{\boldsymbol{\varphi}}_\alpha^{(e)} \in \mathbb{R}^{n_\text{flow}}$ are the flow map nodal degrees of freedom for element e, and $n_\text{int} = |\mathcal{I}_\text{int}^{(e,e')}| \times n_\text{time}$ accounts for all temporal slices within the space-time slab. The interface Lagrange multipliers $\boldsymbol{\mu}_{\text{int},\alpha}$ represent the traction forces transmitted across element boundaries, ensuring force equilibrium at interfaces.

HYBRID GLOBAL SYSTEM

For a domain decomposed into n_elem spatial elements, the global system takes a block-diagonal structure augmented with interface constraints:

$$\begin{bmatrix} \mathbb{A}^{(1)} & 0 & \cdots & 0 & \mathbb{C}_x^{(1)^T} & \mathbb{C}_y^{(1)^T} \\ 0 & \mathbb{A}^{(2)} & \ddots & 0 & \mathbb{C}_x^{(2)^T} & \mathbb{C}_y^{(2)^T} \\ \vdots & \ddots & \ddots & 0 & \vdots & \vdots \\ 0 & \cdots & 0 & \mathbb{A}^{(n_\text{elem})} & \mathbb{C}_x^{(n_\text{elem})^T} & \mathbb{C}_y^{(n_\text{elem})^T} \\ \mathbb{C}_x^{(1)} & \mathbb{C}_x^{(2)} & \cdots & \mathbb{C}_x^{(n_\text{elem})} & \mathbf{0} & \mathbf{0} \\ \mathbb{C}_y^{(1)} & \mathbb{C}_y^{(2)} & \cdots & \mathbb{C}_y^{(n_\text{elem})} & \mathbf{0} & \mathbf{0} \end{bmatrix} \begin{bmatrix} \mathbf{u}^{(1)} \\ \mathbf{u}^{(2)} \\ \vdots \\ \mathbf{u}^{(n_\text{elem})} \\ \boldsymbol{\mu}_{\text{int},\varphi_x} \\ \boldsymbol{\mu}_{\text{int},\varphi_y} \end{bmatrix} = \begin{bmatrix} \mathbf{f}^{(1)} \\ \mathbf{f}^{(2)} \\ \vdots \\ \mathbf{f}^{(n_\text{elem})} \\ \mathbf{0} \\ \mathbf{0} \end{bmatrix} \tag{4.43}$$

where $\mathbb{A}^{(e)}$ is the element-level system matrix from (4.41) for element e, $\mathbf{u}^{(e)}$ contains all unknowns for that element (momentum $\bar{\boldsymbol{\pi}}_\alpha^{(e)}$, flow map $\bar{\boldsymbol{\varphi}}_\alpha^{(e)}$, and local boundary Lagrange multipliers for spatial strong boundary conditions), $\mathbb{C}_\alpha^{(e)}$ extracts interface flow map degrees of freedom from element e, and $\boldsymbol{\mu}_{\text{int},\varphi_\alpha}$ are the interface Lagrange multipliers enforcing continuity of the flow map. The right-hand side vectors $\mathbf{f}^{(e)}$ include element-specific forcing terms and initial conditions as described in (4.24). The zero blocks in the constraint rows enforce homogeneous interface continuity conditions similar to (4.27).

Remark 4.4.1: Static Condensation

The block structure of (4.43) can be exploited via a Schur complement reduction, based on non-overlapping domain decomposition. The element-level matrices $\mathbb{A}^{(e)}$ can be factored independently, and the global interface problem involving only $\boldsymbol{\mu}_{\text{int}}$ can be formed by eliminating interior degrees of freedom. This yields a reduced system:

$$\mathbb{S}\boldsymbol{\mu}_{\text{int}} = \mathbf{g} \qquad (= 0, \text{ in this case}) \tag{4.44}$$

where $\mathbb{S}$ is the Schur complement matrix and $\boldsymbol{\mu}_{\text{int}} = [\boldsymbol{\mu}^T_{\text{int},\varphi_x}, \boldsymbol{\mu}^T_{\text{int},\varphi_y}, \boldsymbol{\mu}^T_{\text{int},\pi_x}, \boldsymbol{\mu}^T_{\text{int},\pi_y}]^T$ collects all interface multipliers. Once the interface constraints are computed, the local element solutions are recovered via independent linear solves. This approach is particularly advantageous for parallel implementations, as the Schur complement method decouples the local element problems, with communication required only at interface degrees of freedom.

4.5. DISCRETE MAPPINGS & TRANSFORMATIONS

Discrete operations for the transformation of forms between configuration spaces also need to be defined. Mappings are also used in order to calculate physical "stretches and stresses" which are useful in defining the deformation gradient in terms of an initial configuration that may be not be in static equilibrium even amidst zero external forcing or imposed boundaries, or purely for post-processing in figuring whether the domain is undergoing failure for instance.

4.5.1. PULLBACK OF CONFIGURATION VARIABLES

The mimetic spectral element method operates on some computational domain $\hat{\Omega} = [-1,1]^2$ with coordinates (ξ,η). A mapping $\boldsymbol{\varphi}_0 : \hat{\Omega} \to \Omega_0$ transforms to the physical reference configuration:

$$\boldsymbol{\varphi}_0(\xi,\eta) = \begin{bmatrix} X(\xi,\eta) \\ Y(\xi,\eta) \end{bmatrix} \qquad \boldsymbol{F}_0 = \nabla_\xi \boldsymbol{\varphi}_0 = \begin{bmatrix} \dfrac{\partial X}{\partial \xi} & \dfrac{\partial X}{\partial \eta} \\ \dfrac{\partial Y}{\partial \xi} & \dfrac{\partial Y}{\partial \eta} \end{bmatrix} \qquad J_0 = \det(\boldsymbol{F}_0) \tag{4.45}$$

The Jacobian determinant J_0 scales volume elements: $dV_0 = J_0\, d\xi d\eta$. The inverse mapping transforms gradients:

$$\nabla_0 = \boldsymbol{F}_0^{-T} \nabla_\xi \qquad \boldsymbol{F}_0^{-1} = \frac{1}{J_0} \begin{bmatrix} \dfrac{\partial Y}{\partial \eta} & -\dfrac{\partial X}{\partial \eta} \\ -\dfrac{\partial Y}{\partial \xi} & \dfrac{\partial X}{\partial \xi} \end{bmatrix} \tag{4.46}$$

The material deformation gradient $\boldsymbol{F} = \nabla_0 \boldsymbol{\varphi}$ is computed from computational coordinates via the chain rule, $\boldsymbol{F} = (\nabla_\xi \boldsymbol{\varphi}) \cdot \boldsymbol{F}_0^{-1}$. For the identity initial configuration $\boldsymbol{\varphi}(\mathbf{X}, t_0) = \mathbf{X}$, this yields $\boldsymbol{F}(t_0) = \mathbf{I}$.

Example 4.5.1

Cook's membrane is a tapered trapezoid with corners $(0,0)$, $(48,44)$, $(0,44)$, $(48,60)$. The bilinear mapping from $[-1,1]^2$ is:

$$X(\xi,\eta) = 24(1+\xi)(1+\eta), \quad Y(\xi,\eta) = 37 + 15\eta + 4\xi + 4\xi\eta. \tag{4.47}$$

The deformation gradient, Jacobian, and inverse are:

$$\boldsymbol{F}_0 = \begin{bmatrix} 24(1+\eta) & 24(1+\xi) \\ 4(1+\eta) & 15+4\xi \end{bmatrix} \qquad J_0 = 264(1+\eta) \qquad \boldsymbol{F}_0^{-1} = \begin{bmatrix} \dfrac{15+4\xi}{264(1+\eta)} & -\dfrac{24(1+\xi)}{264(1+\eta)} \\ -\dfrac{1}{66} & \dfrac{1}{11} \end{bmatrix} \tag{4.48}$$

In the discrete implementation, the flow map gradient with respect to (ξ,η) is expanded using edge and nodal basis functions:

$$\nabla_\xi \boldsymbol{\varphi}^h = \begin{bmatrix} \sum_{i=1}^N \sum_{j=0}^N (\varphi_{x,ij} - \varphi_{x,i-1,j}) e_i(\xi) h_j(\eta) & \sum_{i=0}^N \sum_{j=1}^N (\varphi_{x,ij} - \varphi_{x,i,j-1}) h_i(\xi) e_j(\eta) \\ \sum_{i=1}^N \sum_{j=0}^N (\varphi_{y,ij} - \varphi_{y,i-1,j}) e_i(\xi) h_j(\eta) & \sum_{i=0}^N \sum_{j=1}^N (\varphi_{y,ij} - \varphi_{y,i,j-1}) h_i(\xi) e_j(\eta) \end{bmatrix} \tag{4.49}$$

Then $\boldsymbol{F}^h = (\nabla_\xi \boldsymbol{\varphi}^h) \cdot \boldsymbol{F}_0^{-1}$ is evaluated at GLL quadrature points for integration.

4.5.2. Pullback of Discrete Stress

The first Piola-Kirchhoff stress $\boldsymbol{P} \in \widetilde{\Lambda}^{(2)}(\mathcal{M})$ is pulled back to the computational domain:

$$\boldsymbol{P}_{\text{comp}} = J_0 \boldsymbol{F}_0^{-1} \cdot \boldsymbol{P}, \quad \text{so that} \quad \int_{\Omega_0} \boldsymbol{P} : \nabla_0 \tilde{\boldsymbol{\phi}}\, dV_0 = \int_{\hat{\Omega}} \boldsymbol{P}_{\text{comp}} : \nabla_\xi \tilde{\boldsymbol{\phi}}\, d\xi d\eta \tag{4.50}$$

Componentwise, the pullback is:

$$(P_{\text{comp}})_{11} = J_0 \left[(\boldsymbol{F}_0^{-1})_{11} P_{11} + (\boldsymbol{F}_0^{-1})_{12} P_{21} \right], \qquad (P_{\text{comp}})_{12} = J_0 \left[(\boldsymbol{F}_0^{-1})_{11} P_{12} + (\boldsymbol{F}_0^{-1})_{12} P_{22} \right], \tag{4.51}$$

$$(P_{\text{comp}})_{21} = J_0 \left[(\boldsymbol{F}_0^{-1})_{21} P_{11} + (\boldsymbol{F}_0^{-1})_{22} P_{21} \right], \qquad (P_{\text{comp}})_{22} = J_0 \left[(\boldsymbol{F}_0^{-1})_{21} P_{12} + (\boldsymbol{F}_0^{-1})_{22} P_{22} \right]. \tag{4.52}$$

The metric tensor $\mathbf{g}_0 = \boldsymbol{F}_0^T \boldsymbol{F}_0$ with $\det(\mathbf{g}_0) = J_0^2$ acts as an additional weighting on the discrete Hodge matrices. The stress-weighted Hodge operators from (4.23) now integrate the pullback stress $(P_{\text{comp}})_{ij}$ over the computational domain. The transformation to physical gradients is included in this pullback, so the discrete operators $\mathbb{D}^{ij}$ from (4.18)-(4.19) correctly represent physical divergences in Ω_0.

4.5.3. Pushforward of Deformation Gradient

At each non-linear iteration, the material deformation gradient is updated using the current flow map solution. The discrete flow map degrees of freedom $\bar{\boldsymbol{\varphi}}_x, \bar{\boldsymbol{\varphi}}_y$ are differentiated using the incidence matrices $\mathbb{E}_x^{(1,0)}, \mathbb{E}_y^{(1,0)}$ to obtain gradients in computational coordinates:

$$\nabla_\xi \bar{\boldsymbol{\varphi}}_x = \begin{bmatrix} \mathbb{E}_x^{(1,0)} \bar{\boldsymbol{\varphi}}_x \\ \mathbb{E}_y^{(1,0)} \bar{\boldsymbol{\varphi}}_x \end{bmatrix}, \qquad \nabla_\xi \bar{\boldsymbol{\varphi}}_y = \begin{bmatrix} \mathbb{E}_x^{(1,0)} \bar{\boldsymbol{\varphi}}_y \\ \mathbb{E}_y^{(1,0)} \bar{\boldsymbol{\varphi}}_y \end{bmatrix}. \tag{4.53}$$

These are then reconstructed at quadrature points using the edge basis functions $\boldsymbol{\Psi}_1^\xi, \boldsymbol{\Psi}_1^\eta$. A chain rule transforms these to physical coordinates:

$$F_{11} = \left(\frac{\partial \varphi_x}{\partial \xi} \right) (\boldsymbol{F}_0^{-1})_{11} + \left(\frac{\partial \varphi_x}{\partial \eta} \right) (\boldsymbol{F}_0^{-1})_{21}, \qquad F_{12} = \left(\frac{\partial \varphi_x}{\partial \xi} \right) (\boldsymbol{F}_0^{-1})_{12} + \left(\frac{\partial \varphi_x}{\partial \eta} \right) (\boldsymbol{F}_0^{-1})_{22} \tag{4.54}$$

$$F_{21} = \left(\frac{\partial \varphi_y}{\partial \xi} \right) (\boldsymbol{F}_0^{-1})_{11} + \left(\frac{\partial \varphi_y}{\partial \eta} \right) (\boldsymbol{F}_0^{-1})_{21}, \qquad F_{22} = \left(\frac{\partial \varphi_y}{\partial \xi} \right) (\boldsymbol{F}_0^{-1})_{12} + \left(\frac{\partial \varphi_y}{\partial \eta} \right) (\boldsymbol{F}_0^{-1})_{22} \tag{4.55}$$

From $\boldsymbol{F}$, the right Cauchy-Green tensor $\boldsymbol{C} = \boldsymbol{F}^T \boldsymbol{F}$ and Green-Lagrange strain $\boldsymbol{E} = \frac{1}{2}(\boldsymbol{C} - \mathbf{I})$ are computed. The second Piola-Kirchhoff stress $\boldsymbol{S}$ is then evaluated from the constitutive relation, and the first Piola-Kirchhoff stress is $\boldsymbol{P} = \boldsymbol{F} \cdot \boldsymbol{S}$. The pullbacks (4.51) and (4.52) yield $\boldsymbol{P}_{\text{comp}}$, which enters the stress-weighted Hodge operators for the next iteration.

4.5.4. Pushforward of Cauchy Stress in Physical Coordinates

For a more physical stress output, the Cauchy stress $\boldsymbol{\sigma}$ can be computed in the current (physical) configuration. The Cauchy stress relates to the first Piola-Kirchhoff stress via:

$$\boldsymbol{\sigma} = \frac{1}{J} \boldsymbol{P} \cdot \boldsymbol{F}^T = \frac{1}{J} \boldsymbol{F} \cdot \boldsymbol{S} \cdot \boldsymbol{F}^T \tag{4.56}$$

where $J = \det(\boldsymbol{F})$ is the Jacobian determinant of the material deformation gradient. This requires transforming the deformation gradient back to physical reference coordinates using (4.54)-(4.55) at visualisation points. Once $\boldsymbol{F}$ is known in physical coordinates, the second Piola-Kirchhoff stress is computed from the strain energy, then:

$$\sigma_{11} = \frac{1}{J} \left[F_{11}(S_{11} F_{11} + S_{12} F_{21}) + F_{12}(S_{12} F_{11} + S_{22} F_{21}) \right] \tag{4.57}$$

$$\sigma_{12} = \frac{1}{J} \left[F_{11}(S_{11} F_{12} + S_{12} F_{22}) + F_{12}(S_{12} F_{12} + S_{22} F_{22}) \right] \tag{4.58}$$

$$\sigma_{22} = \frac{1}{J} \left[F_{21}(S_{11} F_{21} + S_{12} F_{22}) + F_{22}(S_{12} F_{21} + S_{22} F_{22}) \right] \tag{4.59}$$

Remark 4.5.1

Note that $\sigma_{21} = \sigma_{12}$ due to symmetry of $\boldsymbol{S}$. This transformation from reference to current configuration is necessary only for post-processing; the variational formulation and discrete operators work entirely in the reference configuration using the pullback stress $\boldsymbol{P}_{\text{comp}}$.

4.6. DISCRETE SYMMETRIES AND CONSERVATION PROPERTIES

The mimetic spectral element method preserves the variational structure of the continuous problem at the discrete level. This preservation is that Noether's theorem applies to the discrete system: symmetries of the discrete action correspond to discrete conservation laws. For non-dissipative hyperelastic materials, the Lagrangian density depends on the deformation map $\boldsymbol{\varphi}(\mathbf{X},t)$, its time derivative $\dot{\boldsymbol{\varphi}}$, and its spatial gradient $\nabla_0\boldsymbol{\varphi}$, often through the deformation gradient $\boldsymbol{F} = \nabla_0\boldsymbol{\varphi}$. The stored energy function $W(\boldsymbol{F})$ and kinetic energy combine to define the Lagrangian:

$$\mathcal{L}(\boldsymbol{\varphi}, \dot{\boldsymbol{\varphi}}, \nabla_0\boldsymbol{\varphi}) = \frac{1}{2}\rho_0|\dot{\boldsymbol{\varphi}}|^2 - W(\nabla_0\boldsymbol{\varphi}) \tag{4.60}$$

The action functional over the space-time domain $\mathcal{M} = \Omega_0 \times [0,T]$ is:

$$\mathcal{A}[\boldsymbol{\varphi}] = \int_0^T \int_{\Omega_0} \mathcal{L}(\boldsymbol{\varphi}, \dot{\boldsymbol{\varphi}}, \nabla_0\boldsymbol{\varphi})\, dV_0\, dt \tag{4.61}$$

This section covers the continuous and discrete treatment of conservation laws for the differentiable Noether symmetries present in the variational structure of a locally space-time spectral mimetic element. Moreover, if it can be shown that the local problem is conservative, then the global problem follows suit.

4.6.1. CONSERVATION OF LINEAR MOMENTUM

CONTINUOUS FORM

To check that *total* linear momentum is conserved, a test function representing a rigid-body *translation* of the flow map is chosen. Let $\widehat{\boldsymbol{\phi}} \in H^1(\Omega_0 \times [0,T])$ be a constant vector field:

$$\widehat{\boldsymbol{\phi}}(\mathbf{X},t) = \boldsymbol{c} \tag{4.62}$$

where $\boldsymbol{c} \in \mathbb{R}^2$ is a constant test vector (e.g., $\boldsymbol{c} = (1,0)^T$ or $(0,1)^T$ in 2D). Substituting $\widehat{\boldsymbol{\phi}} = \boldsymbol{c}$ into the weak form (4.13) with traction contributions leads to:

$$\begin{aligned} -\int_{\Omega_0\times[0,T]} \boldsymbol{\pi}\cdot\frac{\partial \boldsymbol{c}}{\partial t}\, dV_0\, dt + \int_{\Omega_0\times\partial[0,T]} (\boldsymbol{\pi}\cdot\mathbf{n}_t)\cdot\boldsymbol{c}\, dS + \int_{\Omega_0\times[0,T]} \boldsymbol{P} : \nabla_0\boldsymbol{c}\, dV_0\, dt \\ - \int_{\Gamma_N\times[0,T]} \mathbf{t}_N\cdot\boldsymbol{c}\, dA\, dt = 0 \end{aligned} \tag{4.63}$$

where $\mathbf{t}_N$ represents prescribed tractions on the natural boundary Γ_N. Because $\boldsymbol{c}$ is constant in space-time, we have $\nabla_0\boldsymbol{c} = \mathbf{0}$ and $\partial\boldsymbol{c}/\partial t = 0$, so the first and third terms (time derivative and stress) vanish, leaving:

$$\int_{\Omega_0\times\partial[0,T]} (\boldsymbol{\pi}\cdot\mathbf{n}_t)\cdot\boldsymbol{c}\, dS = \int_{\Gamma_N\times[0,T]} \mathbf{t}_N\cdot\boldsymbol{c}\, dA\, dt \tag{4.64}$$

Evaluating the temporal boundary term at $t = 0$ and $t = T$ with outward normal $\mathbf{n}_t = -1$ at $t = 0$ and $\mathbf{n}_t = +1$ at $t = T$:

$$\boldsymbol{c}\cdot\int_{\Omega_0} \boldsymbol{\pi}(T)\, dV_0 - \boldsymbol{c}\cdot\int_{\Omega_0} \boldsymbol{\pi}(0)\, dV_0 = \boldsymbol{c}\cdot\int_0^T \int_{\Gamma_N} \mathbf{t}_N\, dA\, dt \tag{4.65}$$

Since $\boldsymbol{c}$ is arbitrary, we can define the total impulse from traction forces:

$$\mathbf{J}_{\text{trac}} = \int_0^T \int_{\Gamma_N} \mathbf{t}_N\, dA\, dt \tag{4.66}$$

The linear momentum balance then becomes:

$$\int_{\Omega_0} \boldsymbol{\pi}(T)\, dV_0 - \int_{\Omega_0} \boldsymbol{\pi}(0)\, dV_0 = \mathbf{J}_{\text{trac}} \tag{4.67}$$

The above relation shows that the change in total linear momentum equals the impulse from traction forces. If no tractions act on the boundary ($\mathbf{t}_N = \mathbf{0}$), then $\mathbf{J}_{\text{trac}} = \mathbf{0}$ and:

$$\int_{\Omega_0} \boldsymbol{\pi}(0)\, dV_0 = \int_{\Omega_0} \boldsymbol{\pi}(T)\, dV_0 \tag{4.68}$$

demonstrating that the total linear momentum of the system is constant in time.

DISCRETE FORM

To verify discrete conservation of linear momentum, we test the system with a constant vector field representing a rigid-body translation. The discrete test function is chosen from the primal nodal space of 0-forms:

$$\widehat{\boldsymbol{\phi}}_\alpha^h \in \mathcal{V}_h^{(0)}(\mathcal{M}), \quad \widehat{\boldsymbol{\phi}}_\alpha^h = L_t \mathbf{1}, \quad \alpha \in \{x, y\} \tag{4.69}$$

where $L_t \in \mathbb{R}_{>0}$ is the temporal extent of the space-time slab, $\mathbf{1} \in \mathbb{R}^{n_{\text{flow}}}$ is a vector of ones, and $\mathcal{V}_h^{(0)}(\mathcal{M})$ is the discrete space of primal nodal 0-forms. This corresponds to the variational test used in the continuous Noether argument, but now projected into the compatible discrete basis. We do not pre-cancel terms to verify implementation correctness.

For the x-direction, testing the discrete momentum balance (4.16) with the constant test function gives:

$$\begin{aligned}\Delta\pi_x = {} & L_t \mathbf{1}^T \left[\mathbb{E}_t^{(1,0)^T} \bar{\boldsymbol{\pi}}_x - \bar{\boldsymbol{\pi}}_x^f + \bar{\boldsymbol{\pi}}_x^0 \right] \\ & - L_t \mathbf{1}^T \left[-\mathbb{E}_x^{(1,0)^T} \mathbb{H}_{12}^{xy} \mathbb{E}_y^{(1,0)} \bar{\boldsymbol{\varphi}}_y + \mathbb{E}_y^{(1,0)^T} \mathbb{H}_{12}^{yx} \mathbb{E}_x^{(1,0)} \bar{\boldsymbol{\varphi}}_y + \mathbb{E}_x^{(1,0)^T} \mathbb{H}_{11}^{xy} \mathbb{E}_y^{(1,0)} \bar{\boldsymbol{\varphi}}_y - \mathbb{E}_y^{(1,0)^T} \mathbb{H}_{11}^{yx} \mathbb{E}_x^{(1,0)} \bar{\boldsymbol{\varphi}}_y \right]\end{aligned}$$

where $\bar{\boldsymbol{\pi}}_x^f \in \mathbb{R}^{n_{\text{space}}}$ denotes the final momentum state and $\bar{\boldsymbol{\pi}}_x^0 \in \mathbb{R}^{n_{\text{space}}}$ denotes the initial momentum state. The temporal incidence matrix $\mathbb{E}_t^{(1,0)} \in \mathbb{R}^{n_{\text{mom}} \times n_{\text{flow}}}$ defines the discrete time derivative, and the Hodge matrices $\mathbb{H}_{ij}^{xy}, \mathbb{H}_{ij}^{yx} \in \mathbb{R}^{n_{\text{edges}} \times n_{\text{edges}}}$ encode the stress tensor components. Since the spatial incidence matrices satisfy $\mathbb{E}_x^{(1,0)} \mathbf{1} = \mathbf{0}$ and $\mathbb{E}_y^{(1,0)} \mathbf{1} = \mathbf{0}$ (the discrete gradient of a constant function is zero), the entire stress term vanishes. This mimics the continuous case where $\nabla_0 \boldsymbol{c} = \mathbf{0}$. With boundary tractions $\mathbf{t}_N$ on Γ_N, the impulse in the x-direction is:

$$J_{\text{trac},x} = \mathbf{1}^T \mathbf{F}_{\text{trac},x} = \sum_{i=1}^{n_{\text{mom}}} F_{\text{trac},x,i} \tag{4.70}$$

where $\mathbf{F}_{\text{trac},x} \in \mathbb{R}^{n_{\text{mom}}}$ contains the discrete traction forces from (4.30) evaluated at momentum degrees of freedom (dual 2-form locations). The momentum balance is:

$$\Delta\pi_x - J_{\text{trac},x} = 0 \tag{4.71}$$

Similarly for the y-direction:

$$\begin{aligned}\Delta\pi_y = {} & L_t \mathbf{1}^T \left[\mathbb{E}_t^{(1,0)^T} \bar{\boldsymbol{\pi}}_y - \bar{\boldsymbol{\pi}}_y^f + \bar{\boldsymbol{\pi}}_y^0 \right] \\ & - L_t \mathbf{1}^T \left[-\mathbb{E}_x^{(1,0)^T} \mathbb{H}_{22}^{xy} \mathbb{E}_y^{(1,0)} \bar{\boldsymbol{\varphi}}_x + \mathbb{E}_y^{(1,0)^T} \mathbb{H}_{22}^{yx} \mathbb{E}_x^{(1,0)} \bar{\boldsymbol{\varphi}}_x + \mathbb{E}_x^{(1,0)^T} \mathbb{H}_{12}^{xy} \mathbb{E}_y^{(1,0)} \bar{\boldsymbol{\varphi}}_x - \mathbb{E}_y^{(1,0)^T} \mathbb{H}_{12}^{yx} \mathbb{E}_x^{(1,0)} \bar{\boldsymbol{\varphi}}_x \right]\end{aligned}$$

with balance:

$$\Delta\pi_y - J_{\text{trac},y} = 0 \quad \text{where} \quad J_{\text{trac},y} = \mathbf{1}^T \mathbf{F}_{\text{trac},y} = \sum_{i=1}^{n_{\text{mom}}} F_{\text{trac},y,i} \tag{4.72}$$

Each term corresponds to a discrete pairing between the constant test function and contributions from momentum fluxes and internal stress. The temporal incidence matrix $\mathbb{E}_t^{(1,0)^T}$ maps momentum from temporal edges to nodes. All operations are local, and the resulting quantity should vanish up to floating-point precision if conservation is achieved in the absence of external tractions: $\Delta\pi_x \approx 0$, $\Delta\pi_y \approx 0$. If no external tractions act on the domain, there is no source of net momentum gain or loss, confirming discrete conservation of linear momentum componentwise.

4.6.2. CONSERVATION OF ANGULAR MOMENTUM

CONTINUOUS FORM

To check if angular momentum is conserved in the hyperelastic formulation, we test the weak form (4.13) against a skew-symmetric rotation-type test function. Since the choice of test function is arbitrary (the momentum equation must hold for all variations), we choose a test function $\widehat{\boldsymbol{\phi}} \in H^1(\Omega_0 \times [0, T])$ corresponding to a rigid-body rotation of the flow map:

$$\widehat{\boldsymbol{\phi}} = \begin{bmatrix} -\varphi_y \\ \varphi_x \end{bmatrix} \tag{4.73}$$

Substituting into the weak form gives:

$$-\int_{\Omega_0 \times [0,T]} \boldsymbol{\pi} \cdot \frac{\partial \widehat{\boldsymbol{\phi}}}{\partial t} \, dV_0 \, dt + \int_{\Omega_0 \times \partial[0,T]} (\boldsymbol{\pi} \cdot \mathbf{n}_t) \cdot \widehat{\boldsymbol{\phi}} \, dS + \int_{\Omega_0 \times [0,T]} \boldsymbol{P} : \nabla_0 \widehat{\boldsymbol{\phi}} \, dV_0 \, dt = 0 \tag{4.74}$$

The first integral involves:

$$-\int_{\Omega_0 \times [0,T]} \boldsymbol{\pi} \cdot \frac{\partial}{\partial t} \begin{bmatrix} -\varphi_y \\ \varphi_x \end{bmatrix} dV_0 \, dt = -\int_{\Omega_0 \times [0,T]} (-\pi_x \dot{\varphi}_y + \pi_y \dot{\varphi}_x) \, dV_0 \, dt \tag{4.75}$$

The third term involves the contraction of the first Piola-Kirchhoff stress $\boldsymbol{P}$ with the gradient of the rotated test function:

$$\nabla_0 \widehat{\boldsymbol{\phi}} = \begin{bmatrix} -\partial \varphi_y / \partial X & -\partial \varphi_y / \partial Y \\ \partial \varphi_x / \partial X & \partial \varphi_x / \partial Y \end{bmatrix} \tag{4.76}$$

The stress contribution is:

$$\int_{\Omega_0 \times [0,T]} \boldsymbol{P} : \nabla_0 \widehat{\boldsymbol{\phi}} \, dV_0 \, dt = \int_{\Omega_0 \times [0,T]} \left(-P_{11} \frac{\partial \varphi_y}{\partial X} - P_{12} \frac{\partial \varphi_y}{\partial Y} + P_{21} \frac{\partial \varphi_x}{\partial X} + P_{22} \frac{\partial \varphi_x}{\partial Y} \right) dV_0 \, dt \tag{4.77}$$

For hyperelastic materials with the specific structure of the mimetic discretisation, this stress integral evaluates such that its net contribution to the angular momentum balance becomes zero when properly integrated. The boundary term becomes:

$$\int_{\Omega_0 \times \partial[0,T]} (\boldsymbol{\pi} \cdot \mathbf{n}_t) \cdot \begin{bmatrix} -\varphi_y \\ \varphi_x \end{bmatrix} dS = \int_{\Omega_0} (-\pi_x \varphi_y + \pi_y \varphi_x) \Big|_{t=T} dV_0 - \int_{\Omega_0} (-\pi_x \varphi_y + \pi_y \varphi_x) \Big|_{t=0} dV_0 \tag{4.78}$$

Combining all terms and simplifying:

$$\int_{\Omega_0} (\pi_x \varphi_y - \pi_y \varphi_x) \Big|_{t=0} dV_0 = \int_{\Omega_0} (\pi_x \varphi_y - \pi_y \varphi_x) \Big|_{t=T} dV_0 \tag{4.79}$$

which confirms that the total angular momentum is conserved in time, provided no other external torques act over the domain. Moreover, it can also be shown that this leads to a natural symmetry in the Cauchy and second Piola-Kirchhoff stress tensors.

DISCRETE FORM

To verify angular momentum conservation in the discrete hyperelastic formulation, we use a skew-symmetric test function constructed from the current flow map. The discrete test function is chosen from the primal nodal space of 0-forms:

$$\widehat{\boldsymbol{\phi}}_x^h \in \mathcal{V}_h^{(0)}(\mathcal{M}), \quad \widehat{\boldsymbol{\phi}}_x^h = -\bar{\boldsymbol{\varphi}}_y \qquad \widehat{\boldsymbol{\phi}}_y^h \in \mathcal{V}_h^{(0)}(\mathcal{M}), \quad \widehat{\boldsymbol{\phi}}_y^h = \bar{\boldsymbol{\varphi}}_x \tag{4.80}$$

The rotation test vectors are constructed from the flow map degrees of freedom $\bar{\boldsymbol{\varphi}}_x, \bar{\boldsymbol{\varphi}}_y \in \mathbb{R}^{n_{\text{flow}}}$. The flow map is organized with n_{space} spatial nodes and n_{time} temporal nodes, where $n_{\text{flow}} = n_{\text{space}} \times n_{\text{time}}$. For temporal edges (when $n_{\text{time}} > 1$), the test function values at edges are sampled from adjacent nodal values:

$$\widehat{\varphi}_{\alpha,i,k} = \frac{1}{2} \left(\widehat{\varphi}_{\alpha,i}^{k} + \widehat{\varphi}_{\alpha,i}^{k+1} \right) \quad \text{for edge } k = 0, \dots, n_{\text{time}} - 2 \text{ at spatial location } i = 1, \dots, n_{\text{space}} \tag{4.81}$$

where the superscript denotes the temporal node index. The angular momentum change is computed by testing the momentum balance with this rotation field. The inertial contributions are:

$$I_x = \left(\mathbb{E}_t^{(1,0)^T} \bar{\boldsymbol{\pi}}_x \right)^T \widehat{\boldsymbol{\phi}}_x = \sum_{i=1}^{n_{\text{flow}}} \left(\mathbb{E}_t^{(1,0)^T} \bar{\boldsymbol{\pi}}_x \right)_i \cdot (-\bar{\varphi}_{y,i}) \quad I_y = \left(\mathbb{E}_t^{(1,0)^T} \bar{\boldsymbol{\pi}}_y \right)^T \widehat{\boldsymbol{\phi}}_y = \sum_{i=1}^{n_{\text{flow}}} \left(\mathbb{E}_t^{(1,0)^T} \bar{\boldsymbol{\pi}}_y \right)_i \cdot \bar{\varphi}_{x,i} \tag{4.82}$$

The slab boundary contributions from initial and final states are:

$$E_x = \left(\bar{\boldsymbol{\pi}}_x^f \right)^T \widehat{\boldsymbol{\phi}}_x^f - \left(\bar{\boldsymbol{\pi}}_x^0 \right)^T \widehat{\boldsymbol{\phi}}_x^0 \quad E_y = \left(\bar{\boldsymbol{\pi}}_y^f \right)^T \widehat{\boldsymbol{\phi}}_y^f - \left(\bar{\boldsymbol{\pi}}_y^0 \right)^T \widehat{\boldsymbol{\phi}}_y^0 \tag{4.83}$$

where the superscript f denotes the final temporal state and 0 denotes the initial temporal state. The internal stress contributions are:

$$S_x = (\widehat{\boldsymbol{\phi}}_x)^T \left[-\mathbb{E}_x^{(1,0)^T} \mathbb{H}_{12}^{xy} \mathbb{E}_y^{(1,0)} \bar{\boldsymbol{\varphi}}_y + \mathbb{E}_y^{(1,0)^T} \mathbb{H}_{12}^{yx} \mathbb{E}_x^{(1,0)} \bar{\boldsymbol{\varphi}}_y + \mathbb{E}_x^{(1,0)^T} \mathbb{H}_{11}^{xy} \mathbb{E}_y^{(1,0)} \bar{\boldsymbol{\varphi}}_y - \mathbb{E}_y^{(1,0)^T} \mathbb{H}_{11}^{yx} \mathbb{E}_x^{(1,0)} \bar{\boldsymbol{\varphi}}_y \right] \tag{4.84}$$

$$S_y = \left(\widehat{\boldsymbol{\phi}}_y \right)^T \left[-\mathbb{E}_x^{(1,0)^T} \mathbb{H}_{22}^{xy} \mathbb{E}_y^{(1,0)} \bar{\boldsymbol{\varphi}}_x + \mathbb{E}_y^{(1,0)^T} \mathbb{H}_{22}^{yx} \mathbb{E}_x^{(1,0)} \bar{\boldsymbol{\varphi}}_x + \mathbb{E}_x^{(1,0)^T} \mathbb{H}_{12}^{xy} \mathbb{E}_y^{(1,0)} \bar{\boldsymbol{\varphi}}_x - \mathbb{E}_y^{(1,0)^T} \mathbb{H}_{12}^{yx} \mathbb{E}_x^{(1,0)} \bar{\boldsymbol{\varphi}}_x \right] \tag{4.85}$$

The angular momentum change is:

$$\Delta L = I_x + I_y - E_x - E_y - S_x - S_y \tag{4.86}$$

With applied tractions evaluated at edge points $\mathbf{F}_{\text{trac},x}, \mathbf{F}_{\text{trac},y} \in \mathbb{R}^{n_{\text{edges}}}$, where n_{edges} denotes the number of temporal edges times the number of spatial nodes, the applied torque is:

$$\tau_{\text{trac}} = (\widehat{\boldsymbol{\phi}}_x)_{\text{edges}}^T \mathbf{F}_{\text{trac},x} + \left(\widehat{\boldsymbol{\phi}}_y \right)_{\text{edges}}^T \mathbf{F}_{\text{trac},y} \tag{4.87}$$

where the subscript "edges" denotes the test function values obtained from (4.81). For strongly-prescribed boundary conditions enforced via Lagrange multipliers $\boldsymbol{\lambda}_x, \boldsymbol{\lambda}_y \in \mathbb{R}^{n_\lambda}$ on boundary nodes $\mathcal{I}_D \subset \{1, \dots, n_{\text{space}}\}$, the reaction torque is:

$$\tau_{\text{reaction}} = \sum_{i \in \mathcal{I}_D} \left[\lambda_{x,i} \cdot (-\bar{\varphi}_{y,i}^f) + \lambda_{y,i} \cdot \bar{\varphi}_{x,i}^f \right] \tag{4.88}$$

The angular momentum balance is:

$$\Delta L + \tau_{\text{trac}} + \tau_{\text{reaction}} = 0 \tag{4.89}$$

This should be approximately zero (to floating-point precision) if angular momentum conservation is achieved and no other non-traction-induced torque contributions act on the system.

4.6.3. CONSERVATION OF ENERGY

CONTINUOUS FORM

Conservation of energy can be shown by taking the material velocity evaluated at the primal nodes as the choice of test function. Let $\widehat{\boldsymbol{\phi}} \in H^1(\Omega_0 \times [0,T])$ be the material velocity:

$$\widehat{\boldsymbol{\phi}} = \frac{\partial \boldsymbol{\varphi}}{\partial t} = \dot{\boldsymbol{\varphi}} \tag{4.90}$$

which is the time derivative of the flow map. Substituting this into the weak form (4.13) gives:

$$-\int_{\Omega_0 \times [0,T]} \boldsymbol{\pi} \cdot \frac{\partial \dot{\boldsymbol{\varphi}}}{\partial t}\, dV_0\, dt + \int_{\Omega_0 \times \partial[0,T]} (\boldsymbol{\pi} \cdot \mathbf{n}_t) \cdot \dot{\boldsymbol{\varphi}}\, dS + \int_{\Omega_0 \times [0,T]} \boldsymbol{P} : \nabla_0 \dot{\boldsymbol{\varphi}}\, dV_0\, dt = 0 \tag{4.91}$$

Using the momentum-velocity relationship $\boldsymbol{\pi} = \rho_0 \dot{\boldsymbol{\varphi}}$, the first integral becomes:

$$-\int_{\Omega_0 \times [0,T]} \rho_0 \dot{\boldsymbol{\varphi}} \cdot \frac{\partial \dot{\boldsymbol{\varphi}}}{\partial t}\, dV_0\, dt \tag{4.92}$$

Rewriting using the product rule for the scalar product:

$$\frac{\partial}{\partial t}(\dot{\boldsymbol{\varphi}} \cdot \dot{\boldsymbol{\varphi}}) = 2\left(\frac{\partial \dot{\boldsymbol{\varphi}}}{\partial t} \cdot \dot{\boldsymbol{\varphi}}\right) \quad \Rightarrow \quad \frac{\partial \dot{\boldsymbol{\varphi}}}{\partial t} \cdot \dot{\boldsymbol{\varphi}} = \frac{1}{2}\frac{\partial}{\partial t}(\dot{\boldsymbol{\varphi}} \cdot \dot{\boldsymbol{\varphi}}) \tag{4.93}$$

the kinetic contribution becomes:

$$-\int_{\Omega_0 \times [0,T]} \frac{1}{2}\rho_0 \frac{\partial}{\partial t}(\dot{\boldsymbol{\varphi}} \cdot \dot{\boldsymbol{\varphi}})\, dV_0\, dt = -\int_{\Omega_0 \times [0,T]} \frac{\partial}{\partial t}\left(\frac{1}{2}\rho_0 \|\dot{\boldsymbol{\varphi}}\|^2\right) dV_0\, dt \tag{4.94}$$

which is precisely the negative of the integral of the rate of change of kinetic energy density in the material configuration (assuming ρ_0 is constant and Ω_0 is the reference domain). For the stress contribution, we have:

$$\int_{\Omega_0 \times [0,T]} \boldsymbol{P} : \nabla_0 \dot{\boldsymbol{\varphi}}\, dV_0\, dt = \int_{\Omega_0 \times [0,T]} \boldsymbol{P} : \frac{\partial}{\partial t}(\nabla_0 \boldsymbol{\varphi})\, dV_0\, dt \tag{4.95}$$

For hyperelastic materials, the first Piola-Kirchhoff stress is derived from a stored energy potential $W(\boldsymbol{F})$ where $\boldsymbol{F} = \nabla_0 \boldsymbol{\varphi}$:

$$\boldsymbol{P} = \frac{\partial W}{\partial \boldsymbol{F}} \quad \Rightarrow \quad \boldsymbol{P} : \frac{\partial \boldsymbol{F}}{\partial t} = \frac{\partial W(\boldsymbol{F})}{\partial t} \tag{4.96}$$

where the chain rule gives $\partial W/\partial t = (\partial W/\partial \boldsymbol{F}) : (\partial \boldsymbol{F}/\partial t)$. Thus:

$$\int_{\Omega_0 \times [0,T]} \boldsymbol{P} : \frac{\partial \boldsymbol{F}}{\partial t}\, dV_0\, dt = \int_{\Omega_0 \times [0,T]} \frac{\partial W(\boldsymbol{F})}{\partial t}\, dV_0\, dt \tag{4.97}$$

Combining the kinetic and internal energy contributions with the temporal boundary term:

$$-\int_{\Omega_0 \times [0,T]} \frac{\partial}{\partial t}\left(\frac{1}{2}\rho_0 \|\dot{\boldsymbol{\varphi}}\|^2 + W(\boldsymbol{F})\right) dV_0\, dt + \int_{\Omega_0 \times \partial[0,T]} (\boldsymbol{\pi} \cdot \mathbf{n}_t) \cdot \dot{\boldsymbol{\varphi}}\, dS = 0 \tag{4.98}$$

Integrating the first term over time and evaluating the boundary term yields:

$$-\int_{\Omega_0} \left(\frac{1}{2}\rho_0 \|\dot{\boldsymbol{\varphi}}\|^2 + W(\boldsymbol{F})\right)\bigg|_{t=T} dV_0 + \int_{\Omega_0} \left(\frac{1}{2}\rho_0 \|\dot{\boldsymbol{\varphi}}\|^2 + W(\boldsymbol{F})\right)\bigg|_{t=0} dV_0 + \int_{\Omega_0} \left[(\boldsymbol{\pi} \cdot \mathbf{n}_t) \cdot \dot{\boldsymbol{\varphi}}\right]_{t=0}^{t=T} dV_0 = 0$$

The temporal boundary term represents the momentum flux through the temporal boundaries. For a closed time interval with consistent boundary conditions, this ensures the total energy (kinetic plus internal) at the beginning equals the total energy at the end:

$$\int_{\Omega_0} \left(\frac{1}{2}\rho_0 \|\dot{\boldsymbol{\varphi}}\|^2 + W(\boldsymbol{F})\right)\bigg|_{t=0} dV_0 = \int_{\Omega_0} \left(\frac{1}{2}\rho_0 \|\dot{\boldsymbol{\varphi}}\|^2 + W(\boldsymbol{F})\right)\bigg|_{t=T} dV_0 \tag{4.99}$$

demonstrating energy conservation in the absence of boundary work.

DISCRETE FORM

In the discrete formulation, we choose the test function to be the material velocity (primal, nodal):

$$\widehat{\boldsymbol{\phi}}^h_\alpha \in \mathcal{V}^{(0)}_h(\mathcal{M}) \quad \widehat{\boldsymbol{\phi}}^h_\alpha = \frac{1}{L_t}\mathbb{E}_t^{(1,0)}\bar{\boldsymbol{\varphi}}_\alpha \quad \alpha \in \{x, y\} \tag{4.100}$$

i.e., the time derivative of the flow map, where $L_t \in \mathbb{R}_{>0}$ is the temporal extent of the space-time slab. The velocity at temporal edges is computed via the temporal incidence operator $\mathbb{E}_t^{(1,0)}$, which maps nodal 0-forms to edge 1-forms. Let $\mathbf{v}_\alpha \in \mathbb{R}^{n_{\text{mom}}}$ denote the velocity at edge locations:

$$\mathbf{v}_\alpha = \frac{1}{L_t}\mathbb{E}_t^{(1,0)}\bar{\boldsymbol{\varphi}}_\alpha \tag{4.101}$$

Since momentum lives at nodal locations while velocity is naturally defined at edges, we must sample adjacent edge velocities to obtain nodal values. For each spatial location $i = 1, \ldots, n_{\text{space}}$ and temporal node $k = 0, \ldots, n_{\text{time}} - 1$, the nodal velocity is computed by sampling the velocities at the adjacent temporal edges. Let $\bar{\mathbf{v}}_\alpha \in \mathbb{R}^{n_{\text{flow}}}$ denote the sampled nodal velocity vector, where $n_{\text{flow}} = n_{\text{space}} \times n_{\text{time}}$. Additionally, let $\bar{\mathbf{v}}^0_\alpha \in \mathbb{R}^{n_{\text{space}}}$ and $\bar{\mathbf{v}}^f_\alpha \in \mathbb{R}^{n_{\text{space}}}$ denote the nodal velocities at the initial and final temporal slices, respectively. The discrete change in kinetic energy in each direction is:

$$\Delta\text{KE}_x = \left(\mathbb{E}_t^{(1,0)^T}\bar{\boldsymbol{\pi}}_x\right)^T \bar{\mathbf{v}}_x - \left(\bar{\boldsymbol{\pi}}^f_x\right)^T \bar{\mathbf{v}}^f_x + \left(\bar{\boldsymbol{\pi}}^0_x\right)^T \bar{\mathbf{v}}^0_x \tag{4.102}$$

$$\Delta\text{KE}_y = \left(\mathbb{E}_t^{(1,0)^T}\bar{\boldsymbol{\pi}}_y\right)^T \bar{\mathbf{v}}_y - \left(\bar{\boldsymbol{\pi}}^f_y\right)^T \bar{\mathbf{v}}^f_y + \left(\bar{\boldsymbol{\pi}}^0_y\right)^T \bar{\mathbf{v}}^0_y \tag{4.103}$$

where $\bar{\boldsymbol{\pi}}^f_\alpha, \bar{\boldsymbol{\pi}}^0_\alpha \in \mathbb{R}^{n_{\text{space}}}$ are the momenta at the final and initial temporal nodes. The total kinetic energy change is:

$$\Delta\text{KE} = \Delta\text{KE}_x + \Delta\text{KE}_y \tag{4.104}$$

The work done by internal stress over the space-time domain is evaluated using the stress-divergence operators. The nodal velocity vector is paired with the discrete stress-divergence operations:

$$W_{\text{int},x} = \bar{\mathbf{v}}_x^T\left[\mathbb{E}_x^{(1,0)^T}\mathbb{H}^{xy}_{11}\mathbb{E}_y^{(1,0)}\bar{\boldsymbol{\varphi}}_y - \mathbb{E}_x^{(1,0)^T}\mathbb{H}^{xy}_{12}\mathbb{E}_y^{(1,0)}\bar{\boldsymbol{\varphi}}_x \; - \mathbb{E}_y^{(1,0)^T}\mathbb{H}^{yx}_{11}\mathbb{E}_x^{(1,0)}\bar{\boldsymbol{\varphi}}_y + \mathbb{E}_y^{(1,0)^T}\mathbb{H}^{yx}_{12}\mathbb{E}_x^{(1,0)}\bar{\boldsymbol{\varphi}}_x\right]$$

$$W_{\text{int},y} = \bar{\mathbf{v}}_y^T\left[\mathbb{E}_x^{(1,0)^T}\mathbb{H}^{xy}_{12}\mathbb{E}_y^{(1,0)}\bar{\boldsymbol{\varphi}}_y - \mathbb{E}_x^{(1,0)^T}\mathbb{H}^{xy}_{22}\mathbb{E}_y^{(1,0)}\bar{\boldsymbol{\varphi}}_x \; - \mathbb{E}_y^{(1,0)^T}\mathbb{H}^{yx}_{12}\mathbb{E}_x^{(1,0)}\bar{\boldsymbol{\varphi}}_y + \mathbb{E}_y^{(1,0)^T}\mathbb{H}^{yx}_{22}\mathbb{E}_x^{(1,0)}\bar{\boldsymbol{\varphi}}_x\right]$$

The change in internal strain energy is the negative of the total internal work:

$$\Delta U = -(W_{\text{int},x} + W_{\text{int},y}) \tag{4.105}$$

For systems with boundary tractions, the work done is computed using the edge velocities, since traction forces are naturally applied at edges where they are integrated. Let $\mathbf{F}_{\text{trac},x}, \mathbf{F}_{\text{trac},y} \in \mathbb{R}^{n_{\text{mom}}}$ denote the discrete traction force vectors at edge locations. The traction work is:

$$W_{\text{trac}} = \mathbf{v}_x^T\mathbf{F}_{\text{trac},x} + \mathbf{v}_y^T\mathbf{F}_{\text{trac},y} \tag{4.106}$$

The total, discrete energy balance is:

$$\Delta\text{TE} = \Delta\text{KE} + \Delta U - W_{\text{trac}} = 0 \tag{4.107}$$

Combining the kinetic and internal energy changes with traction work gives the net energy change over the time slab, which should sum to zero (up to numerical precision) when all contributions are properly accounted for: $\Delta\text{TE} \approx 0$. If external tractions are present, the energy balance becomes $\Delta\text{KE} + \Delta U = W_{\text{trac}}$, representing energy input from boundary forces. The distinction between using edge velocities for traction work and nodal velocities for kinetic energy reflects the proper geometric placement of these quantities in the discrete formulation.

4.6.4. CONSERVATION OF MASS

CONTINUOUS FORM

For hyperelastic materials, mass conservation follows from the kinematic constraint. The reference density $\rho_0 \in \mathbb{R}_{>0}$ is constant in the material configuration Ω_0. The current density in the spatial configuration transforms as $\rho(\mathbf{x}, t) = \rho_0 / J(\mathbf{X}, t)$, where $J = \det(\boldsymbol{F})$ is the Jacobian determinant. Total mass is:

$$M(t) = \int_{\Omega_0} \rho_0 \, dV_0 = \rho_0 \, |\Omega_0| = constant \tag{4.108}$$

which is independent of deformation since integration is over the fixed material domain.

DISCRETE FORM

The discrete mass at time t is computed via quadrature over the reference configuration:

$$M^h(t) = \sum_{i=1}^{n_{\text{quad},x}} \sum_{j=1}^{n_{\text{quad},y}} w_i w_j J_{0,ij} \rho_0 \tag{4.109}$$

where $w_i, w_j \in \mathbb{R}_{>0}$ are GLL quadrature weights and $J_{0,ij} \in \mathbb{R}_{>0}$ is the discrete Jacobian of the material deformation at quadrature point (i,j), which can be calculated as

$$J^h_{ij}(t) = \left[\left(\mathbb{E}_x^{(1,0)} \bar{\boldsymbol{\varphi}}_x(t)\right) \circ \left(\mathbb{E}_y^{(1,0)} \bar{\boldsymbol{\varphi}}_y(t)\right) - \left(\mathbb{E}_y^{(1,0)} \bar{\boldsymbol{\varphi}}_x(t)\right) \circ \left(\mathbb{E}_x^{(1,0)} \bar{\boldsymbol{\varphi}}_y(t)\right)\right]_{ij} \tag{4.110}$$

where $\circ$ denotes element-wise (Hadamard) product and subscript ij indicates evaluation at quadrature point (i,j). The mass change is:

$$\Delta M^h = M^h(t_f) - M^h(t_0) \approx 0 \tag{4.111}$$

For the identity initial configuration $\boldsymbol{\varphi}(\mathbf{X}, t_0) = \mathbf{X}$, we have $J^h_{ij}(t^0) = 1$ for all i, j. In the discrete formulation, mass is exactly conserved up to the accuracy of the quadrature rule. Any deviation $\Delta M^h \neq 0$ indicates numerical errors in computing the discrete Jacobian or integration weights.

5

NUMERICAL TESTING

This chapter presents numerical experiments to validate the mimetic spectral element formulation developed in the preceding chapters. Before getting to the results, Section 5.1 briefly describes the how the non-linear system is solved in robust fashion. Section 5.2 investigates the solutions of the space-time discretisation, demonstrates p-convergence in spatial and temporal polynomial orders, and tracking the evolution of discrete conservation. Section 5.3 examines steady-state benchmarks to verify the constitutive modelling and geometric mapping framework by comparing against analytical and established numerical solutions, while also confirming discrete conservation.

Additionally, the author acknowledges the use of computational resources and the continuous advocation of High Performance Computing for educational use by the DelftBlue supercomputing cluster and its support team, provided by Delft High Performance Computing Centre [Delft High Performance Computing Centre, 2024].

5.1. NON-LINEAR SOLUTIONS

The non-linear system arising from the hyperelastic formulation requires iterative solution methods due to the configuration-dependent stress-divergence operators $\mathbb{D}^{\alpha\beta}$. This section describes the non-linear solution strategy based on Anderson acceleration, a technique that provides super-linear convergence while maintaining robustness for highly non-linear problems.

5.1.1. GENERAL TECHNIQUES

A discrete non-linear system can be written abstractly as a fixed-point problem, $\mathbf{u} = \mathcal{G}(\mathbf{u})$, where $\mathbf{u}$ contains all unknowns, and $\mathcal{G}$ is constructed by solving the system with stress operators evaluated at the current iterate, i.e. a linearisation point. The non-linearity then enters through the deformation gradient $\boldsymbol{F} = \nabla_0\boldsymbol{\varphi}$, which determines the stress tensor $\boldsymbol{P}(\boldsymbol{F})$ and hence the operators $\mathbb{D}^{\alpha\beta}$. Given an initial guess $\mathbf{u}^{(0)}$, a standard fixed-point iteration generates the sequence $\mathbf{u}^{(k+1)} = \mathcal{G}(\mathbf{u}^{(k)})$ until convergence. However, such iterations exhibit only linear convergence and may be slow for highly non-linear problems. Newton-Raphson methods offer quadratic convergence near the solution but require assembly and factorization of the Jacobian matrix at each iteration, and may fail to converge when the initial guess is far from the solution or when the Jacobian is ill-conditioned.

5.1.2. ANDERSON ACCELERATION

Definition 38 (Anderson Acceleration). *Given a fixed-point iteration $\mathbf{u} = \mathcal{G}(\mathbf{u})$, Anderson acceleration is a method to accelerate the convergence of the fixed-point sequence [Walker and Ni, 2011]. Define the residual $\mathbf{g}(\mathbf{u}) = \mathcal{G}(\mathbf{u}) - \mathbf{u}$, and denote $f_k = \mathcal{G}(\mathbf{u}^{(k)})$ and $g_k = \mathbf{g}(\mathbf{u}^{(k)})$. Given an initial guess $\mathbf{u}^{(0)}$ and an integer parameter $m \geq 1$, the method can be formulated as follows:*

$$\mathbf{u}^{(1)} = \mathcal{G}(\mathbf{u}^{(0)}); \quad \forall k = 1,2,\dots$$

$$\begin{aligned} m_k &= \min\{m,k\} \quad G_k = [g_{k-m_k} \quad \cdots \quad g_k] \\ \boldsymbol{\alpha}_k &= \arg\min_{\boldsymbol{\alpha}\in A_k} \|G_k\boldsymbol{\alpha}\|_2, \quad \textit{where, } A_k = \left\{\boldsymbol{\alpha} = (\alpha_0,\dots,\alpha_{m_k}) \in \mathbb{R}^{m_k+1} : \sum_{i=0}^{m_k} \alpha_i = 1\right\} \\ \mathbf{u}^{(k+1)} &= \sum_{i=0}^{m_k} (\alpha_k)_i f_{k-m_k+i} \end{aligned} \tag{5.1}$$

where the matrix-vector multiplication $G_k\boldsymbol{\alpha} = \sum_{i=0}^{m_k}(\boldsymbol{\alpha})_i g_{k-m_k+i}$, and $(\boldsymbol{\alpha})_i$ is the ith element of $\boldsymbol{\alpha}$.

Remark 5.1.1

The idea behind Anderson acceleration is to find a linear combination of recent iterates whose residuals, when combined, are as small as possible [Anderson, 1965]. This extrapolation strategy uses a *heuristically recent* iteration history to predict a better update direction than the standard fixed-point map alone. Intuitively-put, a history-aware fixed-point iterative scheme. The method has been found to converge faster than standard fixed-point iteration and to be more robust than Newton-Raphson for highly non-linear problems, in some cases even avoiding divergence of the fixed-point sequence [Evans et al., 2019].

In practice, this is done via the constrained least-squares problem in (5.1), which is solved by introducing a small regularization parameter $\epsilon > 0$ and forming the system:

$$\begin{bmatrix} G_k^T G_k + \epsilon\mathbf{I} & \mathbf{1} \\ \mathbf{1}^T & 0 \end{bmatrix} \begin{bmatrix} \boldsymbol{\alpha}_k \\ \mu \end{bmatrix} = \begin{bmatrix} \mathbf{0} \\ 1 \end{bmatrix} \tag{5.2}$$

where $\mathbf{1} \in \mathbb{R}^{m_k+1}$ is a vector of ones, and μ is an auxiliary variable. The regularization prevents ill-conditioning when residual vectors become nearly linearly dependent. Optionally, a relaxation parameter $\beta \in (0,1]$ can be introduced to blend the Anderson-accelerated update with the standard fixed-point update:

$$\mathbf{u}^{(k+1)} = \beta \sum_{i=0}^{m_k} (\alpha_k)_i f_{k-m_k+i} + (1-\beta)\mathcal{G}(\mathbf{u}^{(k)}) \tag{5.3}$$

where $\beta = 1$ corresponds to pure Anderson acceleration, and smaller values provide additional stabilization for highly non-linear problems. The mixing depth m controls the number of previous iterates used in the acceleration. Larger values of m can improve convergence but increase memory requirements and the cost of solving (5.2).

5.1.3. CONVERGENCE IN CONTINUUM FLOW

Convergence is assessed by monitoring changes in the deformation gradient invariants between successive iterations. Let $J^{(k)} = \det(\boldsymbol{F}^{(k)})$ denote the Jacobian determinant at iteration k, and $\mathrm{tr}(\boldsymbol{C}^{(k)}) = \mathrm{tr}((\boldsymbol{F}^{(k)})^T \boldsymbol{F}^{(k)})$ the trace of the right Cauchy-Green tensor. The relative changes are defined as:

$$\Delta J = \frac{\|J^{(k+1)} - J^{(k)}\|_\infty}{\max(\|J^{(k)}\|_\infty, 1)}, \quad \Delta_{\mathrm{tr}} = \frac{\|\mathrm{tr}(\boldsymbol{C}^{(k+1)}) - \mathrm{tr}(\boldsymbol{C}^{(k)})\|_\infty}{\max(\|\mathrm{tr}(\boldsymbol{C}^{(k)})\|_\infty, 1)} \tag{5.4}$$

The iteration is considered converged when both $\Delta J < \tau_{\mathrm{tol}}$ and $\Delta_{\mathrm{tr}} < \tau_{\mathrm{tol}}$, where τ_{tol} is a prescribed tolerance. These provide a physical measures of convergence: ΔJ reflects changes in volumetric deformation, while Δ_{tr} captures changes in total strain energy density. A maximum iteration count $k_{\max}$ of 50 is imposed to prevent indefinite cycling in cases where convergence stalls over τ_{tol}. Per time step, the iteration history is reset and the converged solution from the previous time step provides the initial guess for the current step. Material inversion is detected by consistently checking $\min(J^{(k)}) > 0$.

5.2. UNSTEADY HYPERELASTICITY

This section gives a selection of "unit", single spatial element cases used to assess the implementation. Firstly, a free identity domain subject to angular momentum (Subsection 5.2.1); secondly, identifying physical behaviour under a mapping and strong boundary conditions (Subsection 5.2.2); and and lastly, convergence testing on a simple case with strong boundaries under refinement in space and time order (Subsection 5.2.3).

5.2.1. INDUCING ANGULAR MOMENTUM

The first test considers unsteady rigid body rotation, with the reference - a square of $[-1,1]^2$ m^2 - and initial spatial configurations trivially-related by the identity map, just to avoid the additional complexity of an added mapping, but to also observe physical symmetries in the solution. This test serves to also verify that the numerical scheme correctly maintains angular momentum, energy, and linear momentum over extended time periods for a system with a known analytical solution *under limits*, i.e. a rigid, conservative system (without dissipation) keeps rotating given some angular momentum.

The initial conditions are prescribed as a state of pure rigid body rotation with clockwise angular velocity $\omega = 0.5$ rad/s about the domain centre $(0,0)$. The identity flowmap $\varphi(\mathbf{x}_0, 0) = \mathbf{x}_0$ is imposed initially, while the momentum field is set to induce rotation. For a rigid rotation, the velocity field is given by $\mathbf{v} = \omega\mathbf{r}^\perp$, where $\mathbf{r} = \mathbf{x} - \mathbf{c}$ is the position vector relative to the rotation centre and $\mathbf{r}^\perp = (-y, x)^T$ represents the perpendicular direction. The continuous momentum density field follows as:

$$\boldsymbol{\pi}(\mathbf{x}) = \rho\mathbf{v} = \rho\omega \begin{bmatrix} -(y - c_y) \\ (x - c_x) \end{bmatrix} = \begin{bmatrix} -\rho\omega y \\ \rho\omega x \end{bmatrix}, \tag{5.5}$$

where $c_x = c_y = 0$ for the domain center.

To discretise this initial momentum field via (4.24), an L^2 projection onto the space of primal, nodal basis functions is employed. For each spatial degree of freedom in the momentum space π^i, the projected coefficient is obtained through the L^2 inner product:

$$\pi^i_{x,\text{in}} = \langle \boldsymbol{\pi}_x, \phi_i \rangle_{L^2(\Omega)}, \quad \pi^i_{y,\text{in}} = \langle \boldsymbol{\pi}_y, \phi_i \rangle_{L^2(\Omega)}, \tag{5.6}$$

where ϕ_i are the tensor-product Lagrange basis functions defined on the Gauss-Lobatto nodes. The L^2 inner product $\langle f, g \rangle_{L^2(\Omega)} = \int_\Omega f(\mathbf{x}) g(\mathbf{x}) \, \mathbf{d}\mathbf{x}$ is evaluated exactly using Gauss-Lobatto quadrature:

$$\langle f, g \rangle_{L^2(\Omega)} = \sum_{q_x, q_y} f(\mathbf{x}_q) g(\mathbf{x}_q) w_{q_x} w_{q_y}, \tag{5.7}$$

where $\mathbf{x}_q$ are the tensor-product Gauss-Lobatto quadrature points and w_{q_x}, w_{q_y} are the corresponding one-dimensional quadrature weights. This projection on (4.24) ensures that the discrete momentum field preserves the correct total angular momentum $L_z = \sum_i (\mathbf{r}_i \times \boldsymbol{\pi}_i)_z$ at the initial time.

Material properties follow the St. Venant-Kirchhoff hyperelastic model with Lamé parameters $\lambda = 20$ Pa and $\mu = 10$ Pa, and material density $\rho = 1.25$ kg/m^3. No external forces or boundary tractions are applied; all boundaries are free. The simulation runs for a total time of $T = 10.0$ s. The spatial discretisation uses polynomial order $N = 5$ with Gauss-Lobatto quadrature of order $N_f = 7$, while temporal discretisation employs $N_t = 2$ within each space-time slab of length $\Delta t = 0.01$ s. Anderson acceleration with depth $m = 4$ is used for the non-linear solver, with no mixing and no regularisation.

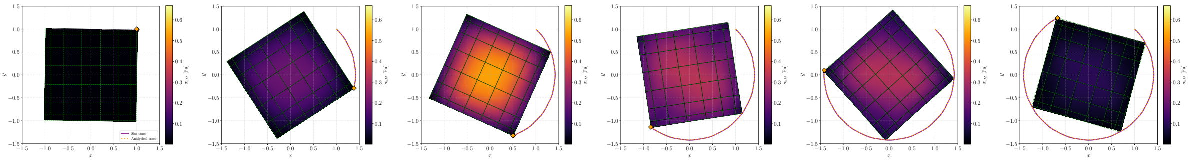

(a) $t = 0.005$ s **(b)** $t = 1.98$ s **(c)** $t = 3.99$ s **(d)** $t = 6.0$ s **(e)** $t = 8.0$ s **(f)** $t = 10.0$ s

Figure 5.1: Flowmap evolution for $\lambda = 20$ Pa and $\mu = 10$ Pa, with reference solution plotted

Figure 5.1 depicts snapshots of the simulated domain along with the reference, analytical solution taken as the same initial domain under the same angular velocity $\omega = 0.5$ rad/s and centre of rotation $(0,0)$, for comparison. The simulated flowmap (in black) and the reference solution's flowmap reference grid (in green), with the von Mises stress (5.13) of the simulation coloured. A trace of the northeast corner of the domain over time is also given for visual clarity and reveals a trajectory that almost approximates a circular path, almost consistent with the analytical solution for rigid body rotation at $\omega = 0.5$ rad/s. Rather, a slight, but symmetric deviation from perfectly circular rotation is noted, indicating the presence of small elastic deformations superimposed on the dominant rotational motion in Figure 5.2a. This is also seen from the pulsing of the von Mises stress field, indicating a non-zero internal stress. This pulsating behaviour suggests that the domain experiences internal elastic stresses that arise implicitly from the prescribed rotational motion, given the structure-preserving nature of the simulation, being in translational equilibrium, and void of external forcing or fixed boundaries. The first point being reinforced by conservation balance laws being respected throughout time, with no visible drift nor increase, as seen in Figure 5.2b.

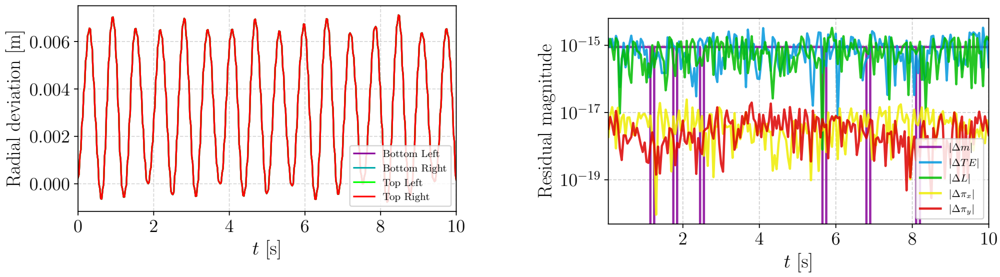

(a) Deviation in corner nodes between the reference and simulation. Note that the lines precisely overlap

(b) Conservation residuals over time on log-scale

Figure 5.2: Diagnosing the $\lambda = 20$ Pa, $\mu = 10$ case

To further investigate the influence of material stiffness on the observed elastic deformations, a more compliant membrane with Lamé parameters $\lambda = 2$ Pa and $\mu = 1$ Pa (ten times lower than the previous case) was examined. The results are presented in Figure 5.3 and Figure 5.4. As anticipated, the reduced stiffness leads to more pronounced elastic oscillations on the rigid rotation, with radial deviations increasing by approximately ten times compared to the stiffer configuration (Figure 5.4a). This more evidently appears on the snapshot of the final time in Figure 5.3f, especially compared to Figure 5.1f. The trace also indicates that the simulated case has now undergone a lower total rotation over time. Additionally, the frequency of these oscillations reduces by $\sqrt{10}$, which matches the proportionality $f \propto \sqrt{k/m}$ for mass-spring systems [Haberman, 2013] when recalling St. Venant Kirchhoff as the linear extension of Hooke's Law (Subsection 3.4.3), as $k \propto \mathbf{E}(\lambda, \mu)$. Despite these more significant elastic deformations, the conservation laws remain well-preserved throughout the simulation (Figure 5.4b), demonstrating the robustness of the mimetic discretisation amidst larger deformations.

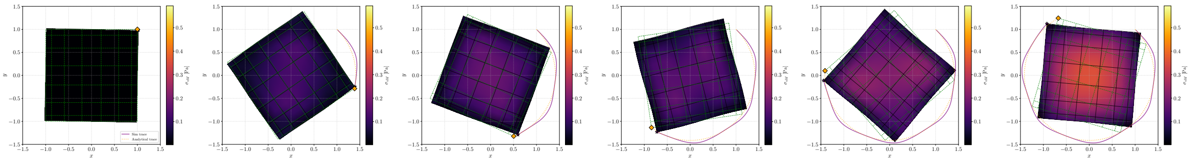

(a) $t = 0.005$ s **(b)** $t = 1.98$ s **(c)** $t = 3.99$ s **(d)** $t = 6.0$ s **(e)** $t = 8.0$ s **(f)** $t = 10.0$ s

Figure 5.3: Flowmap evolution for $\lambda = 2$ Pa and $\mu = 1$ Pa, with reference solution plotted

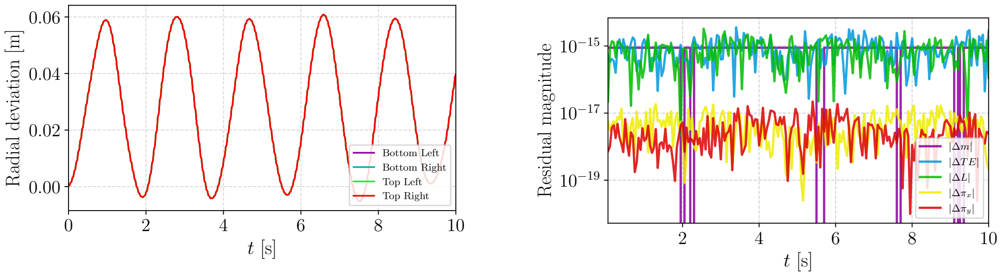

(a) Deviation in corner nodes between the reference and simulation. Note that the lines precisely overlap

(b) Conservation residuals over time on log-scale

Figure 5.4: Diagnosing the $\lambda = 2$ Pa, $\mu = 1$ case

The observed internal stresses arise from the centrifugal, fictitious force inherent to the Lagrangian description. When formulating the problem in the material frame, where particles are tracked in the material (body-fixed) frame. For some material point at position $\mathbf{r} = \mathbf{x} - \mathbf{c}$ relative to the rotation centre, the centrifugal force per unit volume acts radially outward:

$$\mathbf{f}_{\text{cf}} = \rho\omega^2\mathbf{r}, \tag{5.8}$$

where for the two-dimensional case with rotation perpendicular to the plane, this reduces from the expression $\mathbf{f}_{\text{c}} = -\rho\boldsymbol{\omega} \times (\boldsymbol{\omega} \times \mathbf{r})$. Unlike a truly rigid body (as mimicked by the reference solution) - where internal forces exactly balance centrifugal effects without inducing strain - an elastic continuum must deform to develop the resisting stresses, yielding radial oscillations superimposed on the mean rotational motion.

Interestingly, the reduction in overall rotation for the lowered-stiffness case (Figure 5.3) is reminiscent of classical pirouette problem in mechanics. When a spinning ice skater, with their arms retracted, extends their arms they do work towards the centrifugal force pulling radially outward; which is also observed with the positive deviation in Figure 5.4a. This work is then converted into internal strain energy from kinetic energy, reducing angular velocity while still conserving angular momentum. In this test, a similar and more complex energy exchange occurs with the strain energy stored in the deformed configuration exchanges with kinetic energy as the body pulsates. Replication of such dynamics is still complicated since the distribution of mass evolves with shape and quantifying rotation becomes vague as the body morphs continuously [Cline, 2017]. Nevertheless, the presence of physical dynamics in the mimetic discretisation, without explicitly requiring closed-form expressions for the coupled rotation-deformation, dynamics is notable.

5.2.2. PRESCRIBING BOUNDARY CONDITIONS

In considering a more application-like test case, a highly scaled - in terms of material parameters - domain of Cook's membrane (see Figure 5.15 and Subsection 5.3.1) is considered. This serves to primarily test the discretisation amidst a non-identity mapping, the application of non-trivial boundary conditions, and the upholding of conservation laws over extended periods of time and cyclic, large deformations. A vertical traction of $\sigma_y = -200$ Pa is applied over the east boundary, while the western boundary is clamped with a fixed flowmap φ in both x and y directions. Material properties follow the St. Venant-Kirchhoff hyperelastic model with Lamé parameters $\lambda = 30$ Pa and $\mu = 20$ Pa, corresponding to a Young's modulus $E = \mu(3\lambda + 2\mu)/(\lambda + \mu) = 52$ Pa and Poisson's ratio $\nu = \lambda/(2(\lambda + \mu)) = 0.3$, with material density $\rho = 1.25$ kg/m^3 (unit thickness). The simulation employs plane strain conditions and runs for a total time of $T = 40.0$ s. The spatial discretisation uses polynomial order $N = 7$ with Gauss-Lobatto quadrature of order $N_f = 9$, while temporal discretisation employs $N_t = 2$ within each space-time slab of length $\Delta t = 2 \times 10^{-3}$ s. Anderson acceleration with $m = 4$ depth is used for the non-linear solver, without regularisation nor mixing.

The following analysis presents the evolution of key physical fields-stress components and derived quantities at select time instances throughout the deformation process. Figure 5.5 shows the temporal evolution of the normal stress component σ_{xx}, Figure 5.6 presents the von Mises equivalent stress distribution, and Figure 5.7 depicts the velocity magnitude field. Finally, Figure 5.8 displays the conservation diagnostics ensuring the structure-preservation of the discrete system throughout time.

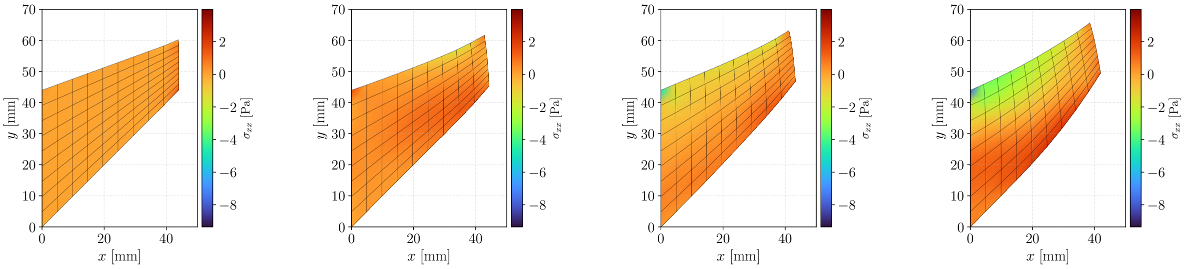

(a) $t = 0.05$ s **(b)** $t = 10.05$ s **(c)** $t = 20.05$ s **(d)** $t = 40.0$ s

Figure 5.5: Evolution of Cauchy stress component σ_{xx} at selected time instances

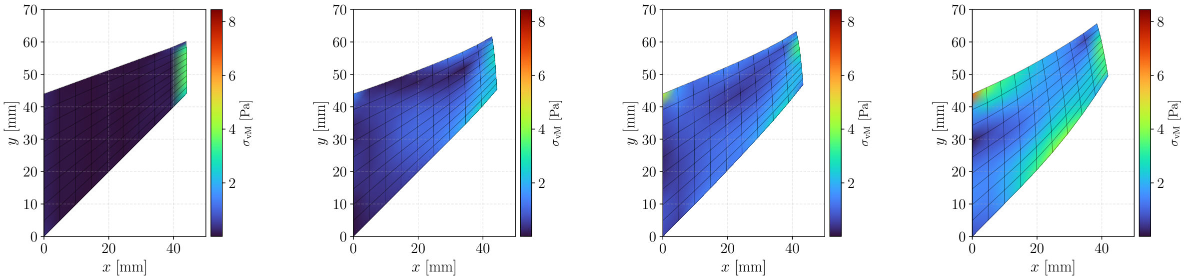

(a) $t = 0.05$ s **(b)** $t = 10.05$ s **(c)** $t = 20.05$ s **(d)** $t = 40.0$ s

Figure 5.6: Evolution of von Mises stress σ_{vM} at selected time instance

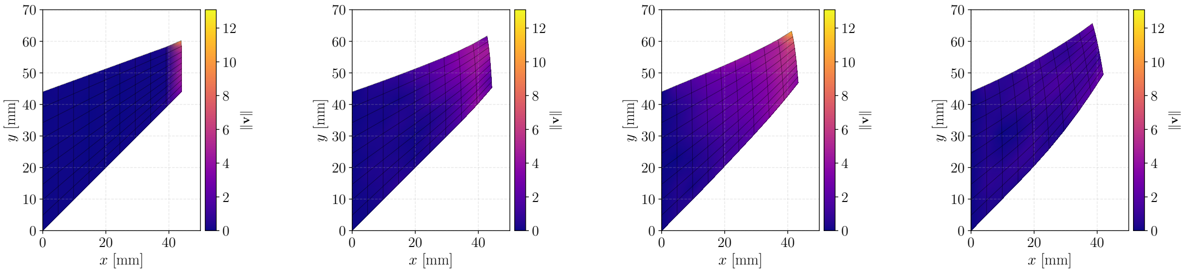

(a) $t = 0.05$ s **(b)** $t = 10.05$ s **(c)** $t = 20.05$ s **(d)** $t = 40.0$ s

Figure 5.7: Evolution of velocity magnitude $\|\mathbf{v}\|$ at selected time instances

Note that the domain does go through several periods in the extent of its deformation despite the selected time instances. This is more visible in Figure 5.9. The Cauchy stress field σ_{xx} in Figure 5.5 reveals the primary loading direction and demonstrates the tensile stress experienced along the bottom of the membrane, with the top being under compression. The stress concentration near the clamped western boundary is clearly visible, with gradients smoothly propagating through the deformed mesh structure. The von Mises stress distribution in Figure 5.6 provides insight into the yielding potential and overall stress magnitude, showing peak values near the sharp gradient northwestern and evolving spatial patterns as the membrane undergoes large deformation. The velocity field in Figure 5.7 captures the dynamic response of the structure, with maximum velocities observed during transient phases and diminishing as the system approaches the extent of its deformation.

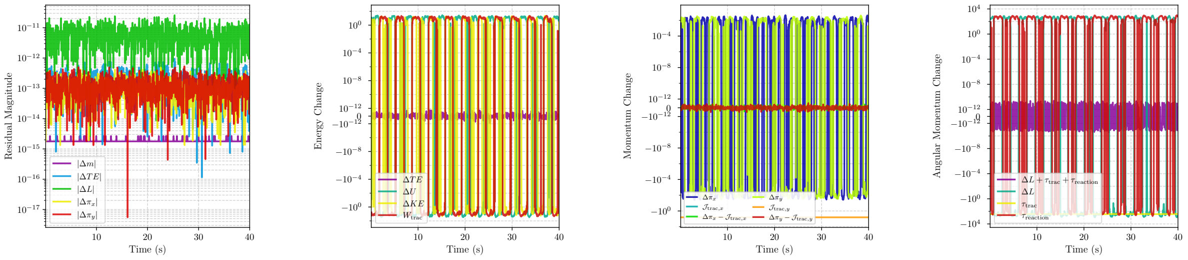

(a) Conservation residuals **(b)** Energy balance **(c)** Linear momentum **(d)** Angular momentum

Figure 5.8: Discrete conservation laws over time

The conservation law diagnostics in Figure 5.8 validate that conservation is held at a discrete level. The residuals remain low throughout the simulation, confirming that mass, linear momentum, angular momentum, and energy are conserved and bounded. The energy balance plot demonstrates that the change in total energy (kinetic plus internal) is balanced by the external work from applied tractions, with residuals remaining consistently below 10^{-10} J. Similarly, the linear and angular momentum balances show that momentum changes are correctly accounted for by the applied impulses and torques, respectively.

To assess the influence of material constitutive relations and stiffness parameters on the Cook's membrane response, simulations were conducted with two hyperelastic models - Ciarlet and St. Venant-Kirchhoff - and two sets of Lamé parameters: ($\lambda = 15$ Pa, $\mu = 10$ Pa) and ($\lambda = 30$ Pa, $\mu = 20$ Pa). Both models share the same general form for the strain energy density (see Section 3.4) but differ in their treatment of geometric nonlinearity. The Ciarlet formulation enforces polyconvexity and is typically better-behaved under large deformations [Ciarlet, 2002] [Khaniki et al., 2023], whereas the St. Venant Kirchoff model, while simpler, may exhibit unphysical behaviour at higher strains. All simulations employed identical setups as before ($N = 7$, $N_t = 2$, $\Delta t = 2 \times 10^{-3}$ s) and were also run for $T = 40$ s under plane strain conditions with a vertical traction of $\sigma_y = -200$ Pa. Figure 5.9 presents the evolution of flowmap and stress quantities at characteristic domain locations for the four setups. Note that conservation was still shown to hold for these cases.

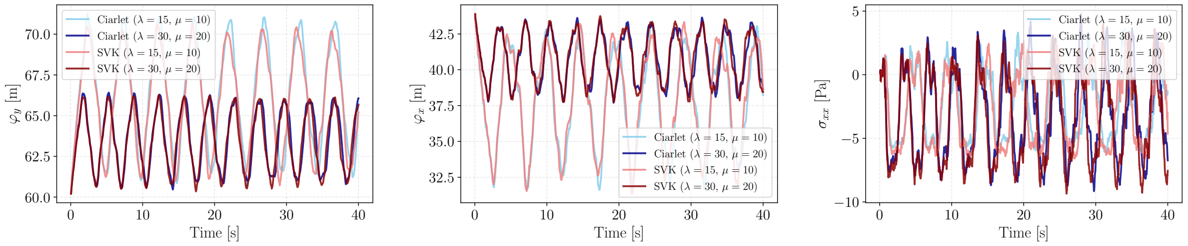

(a) φ_y at northeast corner **(b)** φ_x at northeast corner **(c)** σ_{xx} at northwest corner

Figure 5.9: Comparison of flowmap trajectories and stress evolution for Ciarlet and St. Venant Kirchoff material models

In the vertical displacement φ_y (Figure 5.9a), both models exhibit oscillatory behaviour with the same dominant frequency, though the Ciarlet formulation shows slightly larger amplitudes, particularly at higher stiffness ($\lambda = 30$, $\mu = 20$). The horizontal displacement φ_x (Figure 5.9b) also indicates the Ciarlet model producing larger lateral motion, particularly for the less stiffer parameter. This difference could reflect the artificial stiffening inherent in the St. Venant Kirchoff formulation compared to real material behaviour, which is better approximated by more generalised hyperelastic functionals such as Ciarlet's polyconvex formulation [Bernd Sautter et al., 2022]. The stress component σ_{xx} at the northwest corner (Figure 5.9c) exhibits the most pronounced material dependence, with the Ciarlet model generating higher peak stresses for the first few periods compared to St. Venant Kirchoff. Increasing the Lamé parameters consistently reduces stress magnitudes and displacement ranges across both models, as well as increasing frequency of the oscillations, aligning with the observations also seen in Subsection 5.2.1. Overall, the

Ciarlet formulation produces sightly higher deformations that are more representative of physical elastic behaviour, whereas the St. Venant Kirchoff model exhibits artificial stiffening that constrains the deformation response under the applied loading.

5.2.3. ESTABLISHING CONVERGENCE

The convergence analysis involves the identity (square), spatial domain $[-1,1]^2$ subjected to a normal stress of $\sigma_x = 15$ Pa (towards the west) and vertical traction of $\sigma_y = 0$ Pa over the east boundary. The western boundary has a strongly fixed flowmap in x and y (see example boundary conditions in Subsection 4.4.2), as with the previous test. Material properties are characterised by Lamé parameters $\lambda = 75$ Pa and $\mu = 75$ Pa, with $\rho = 1$ kg/m^3. The total simulation time is $T = 4.0$ s and over-integration in the spatial direction is used with $N+2$ order of quadrature on a Gauss-Lobatto grid, as well as a solver tolerance of 1×10^{-9}. To an extent, the problem can be interpreted as a membrane - or mass-spring system - problem undergoing cyclic deformation due to a constant, directional load. To also evaluate convergence in a numerical fashion, the L^2 error in the flowmap solution at the north-eastern corner of the domain is used and is relatively compared against a baseline reference solution of $N = 8$, $N_t = 3$, $\Delta t = 4 \times 10^{-5}$. The L^2 norm itself is calculated through reusing the Gauss-Lobatto points over space-time slabs and is formally calculated as:

$$\|\varphi - \varphi_{\text{ref}}\|_{L^2(0,T)} = \sqrt{\int_0^T (\varphi(t) - \varphi_{\text{ref}}(t))^2 \, dt}, \tag{5.9}$$

where φ represents the flowmap component (x or y) at a select point, and the relative error is defined as:

$$\epsilon_{\text{rel}} = \frac{\|\varphi - \varphi_{\text{ref}}\|_{L^2(0,T)}}{\|\varphi_{\text{ref}}\|_{L^2(0,T)}}. \tag{5.10}$$

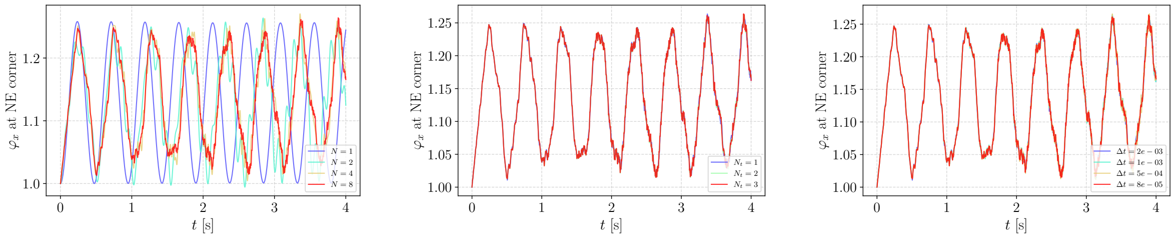

(a) φ_x at northeast corner versus time for $N = 1,2,4,8$ at $N_t = 2$ and $\Delta t = 2 \times 10^{-4}$ s

(b) φ_x at northeast corner versus time for $N_t = 1,2,3$ at $N = 8$ and $\Delta t = 2 \times 10^{-3}$ s.

(c) φ_x at northeast corner versus time for various Δt at $N = 8$ and $N_t = 1$

Figure 5.10: Time evolution of φ_x at the northeast corner for select discretisation parameters

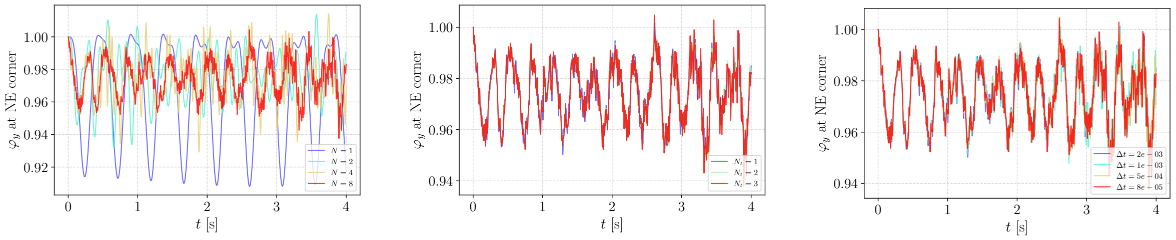

(a) φ_y at northeast corner versus time for $N = 1,2,4,8$ at $N_t = 2$ and $\Delta t = 2 \times 10^{-4}$ s

(b) φ_y at northeast corner versus time for $N_t = 1,2,3$ at $N = 8$ and $\Delta t = 2 \times 10^{-3}$ s.

(c) φ_y at northeast corner versus time for various Δt at $N = 8$ and $N_t = 1$

Figure 5.11: Time evolution of φ_y at the northeast corner for select discretisation parameters

As the traction is in the x-direction, the primary deformation is seen in φ_x as seen in Figure 5.10a, in contrast to Figure 5.11a. We also note that lower N leads to a "lag" in material response, which is also supported by the lower Cauchy stresses σ_{11} in Figure 5.14a. Despite the out-of-phase behaviour from $N = 1$ the amplitude of the primary mode is still well-resolved. A larger variation is seen in Figure 5.11a, where the magnitude decreases due to the Poisson effect. As per the effect of time discretisation with order N_t and interval Δt, their effects are quite minimal in terms of the general evolution. Nevertheless, as still seen in Figure 5.11c, a finer discretisation does aid with maintaining stability over extended time periods. Furthermore, while not immediately explicit, sufficient time discretisation is still important for the overall stability bound of the system.

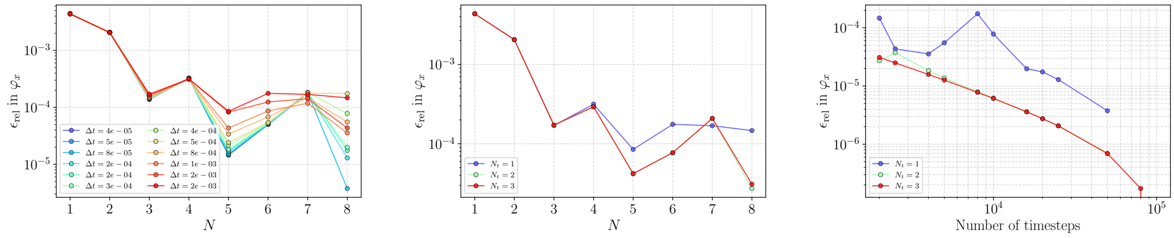

(a) Relative L^2 error in φ_x versus N at $N_t = 1$ for various Δt

(b) Relative L^2 error in φ_x versus N for $N_t = 1,2,3$ at $\Delta t = 2 \times 10^{-3}$ s

(c) Relative L^2 error in φ_x versus number of timesteps at $N = 8$ for $N_t = 1,2,3$

Figure 5.12: Convergence nature using relative L^2 error in φ_x of northeast corner with respect to space and time order

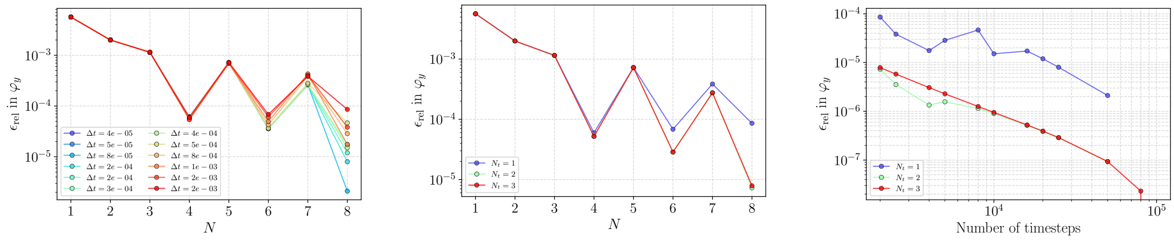

(a) Relative L^2 error in φ_y versus N at $N_t = 1$ for various Δt.

(b) Relative L^2 error in φ_y versus N for $N_t = 1,2,3$ at $\Delta t = 2 \times 10^{-3}$ s

(c) Relative L^2 error in φ_y versus number of timesteps at $N = 8$ for $N_t = 1,2,3$

Figure 5.13: Convergence nature using relative L^2 error in φ_y of northeast corner with respect to space and time order

Interestingly the relative L^2 error plots in Figures 5.12 and 5.13 depict a non-monotonic reduction with N. In particular that regardless of Δt, the L_2 error for φ_x for $N = 7$ is nearly the same - in contrast to other values of N (Figure 5.12a). An explanation in the form of an interplay between time and spatial resolution can be partially observed from the behaviour in Figures 5.12b and 5.13b. Until $N = 5$, spatial resolution errors appear to dominate, and when the time discretisation improves at and beyond $N = 5$, the error drops again - and so on. Otherwise it may still seem that N_t appears to not play a major role in reducing the error beyond $N_t = 2$, although it is still fruitful to see the higher rate of convergence with number of timesteps for $N_t > 1$ in Figures 5.13c and 5.12c, which gives confidence in at least resolving the amplitudes of the modes (but not so much telling on the phase errors seen in the flowmap evolutions). It is expected that the finer and higher discretisation in time is able to better resolve elastic waves within the space-time domain, especially as seen in the variance of φ_y across different time discretisations towards $T = 4$ in Figure 5.11.

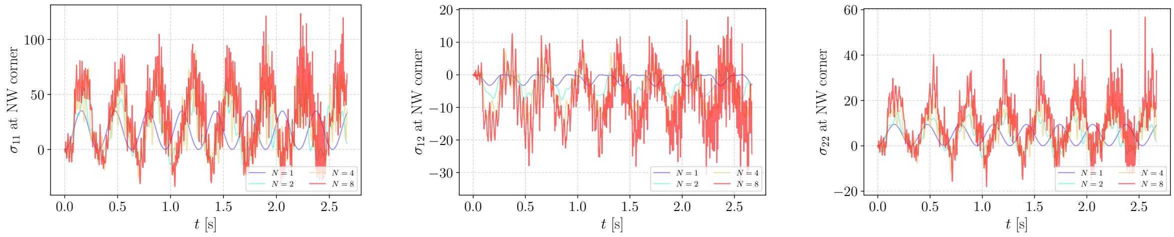

(a) σ_{11}

(b) σ_{12}

(c) σ_{22}

Figure 5.14: Evolution of Cauchy stress at the northwest corner of the domain, for $N = 1,2,4,8$ at $N_t = 2$ and $\Delta t = 2 \times 10^{-4}$ s

From Figure 5.14, it becomes quite clear that, increasing the polynomial degree N improve the spatial resolution of the simulation. The element can therefore represent sharper gradients, i.e. stress concentrations, and elastic modes. This behaviour is especially visible in the stress-time histories at the north–west corner: for $N = 1$ and $N = 2$ the curves are relatively smooth nearly periodic but miss part of the oscillatory nature of elastic media [Ogden, 1973], whereas for $N = 4$ and $N = 8$ the signals exhibit more pronounced modes. From a physical standpoint, the clamped-traction configuration excites a range of elastic waves that reflect between the fixed and loaded ends of a 2D, elastic membrane [Haberman, 2013]. The continuous problem supports infinitely many eigenmodes; low-order polynomials can only capture the lowest modes, while high-order polynomials can incorporate several modes within the same element. As the curves obtained tend to cluster together indicates that the stress is converging with higher N.

5.3. STEADY HYPERELASTICITY

To validate the constitutive modelling and spatial discretisation independent of temporal dynamics, we first examine the steady-state limit of the formulation. In this regime, inertial effects vanish and the problem reduces to non-linear elastostatics governed by the balance of internal stress and external loading. This is formulated by considering a single space-time slab with temporal extent $\Delta t = 1$ and enforcing zero momentum at the final time. Recall the system from (4.41). For the Hamiltonian formulation underlying the space-time discretisation, both initial and final conditions must be specified. In the steady limit, we set the initial momentum $\bar{\boldsymbol{\pi}}_\alpha^0 = \mathbf{0}$ and enforce the final momentum $\bar{\boldsymbol{\pi}}_\alpha^f = \mathbf{0}$, reflecting the physical requirement that all time-dependent terms vanish in equilibrium. This constraint shows up in the momentum-velocity relation: with $\bar{\boldsymbol{\pi}}_\alpha = \rho_0 \dot{\boldsymbol{\varphi}}_\alpha$, zero momentum corresponds to zero velocity, eliminating inertial contributions. The system then reduces to a spatial boundary value problem where the flow map $\bar{\boldsymbol{\varphi}}_\alpha$ adjusts to balance internal stress (integrated in $\mathbb{D}^{\alpha\beta}$) with applied tractions $\mathbf{F}_{\mathrm{trac},\alpha}$ and boundary constraints. This steady-state formulation provides a check of the material constitutive modelling by comparing against numerical benchmarks for hyperelastic formulations.

Additionally, to improve robustness for problems involving large deformations or high loads, we also use load stepping: The applied traction is linearly increased from zero to the target value over a sequence of load increments. At each load step, the converged solution from the previous step serves as the initial guess, allowing the non-linear solver to navigate the deformation path gradually.

5.3.1. COOK'S MEMBRANE BENCHMARK

Cook's membrane is a classical benchmark problem for testing finite element formulations under combined bending and shearing deformations. Originally introduced by [Cook, 1974], it features a tapered cantilever beam subjected to a uniform upward shear on its free edge. Figure 5.15 illustrates the domain.

The membrane occupies a trapezoidal domain with unit thickness in 2D in the initial configuration, with dimensions illustrated in Figure 5.15. The left edge (at $x = 0$) is clamped, enforcing zero displacement in both x and y directions. two-dimensional plane-strain problem with unit thickness. A uniform shear traction p_0 is applied in the positive y-direction along the right edge (at $x = 48$ mm), while the top and bottom edges remain traction-free. The geometry tapers from a height of 44 mm at the left edge to 16 mm at the right edge, creating a non-uniform stress distribution that acts as good test for bending and shearing. The vertical deformation u_y of reference point A at the top-right corner (coordinates $(48, 60)$ mm in the initial configuration) serves as the primary diagnostic location.

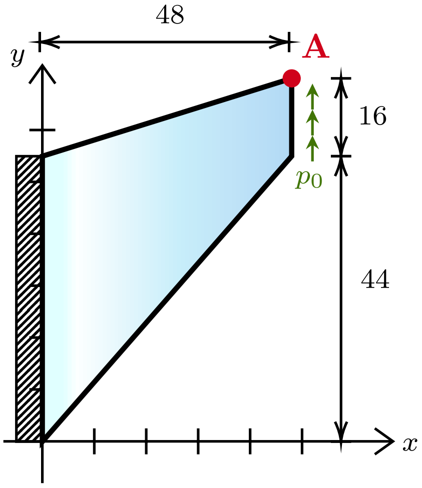

Figure 5.15: Geometry and boundary conditions for Cook's membrane benchmark, with all dimensions in mm. Point A at the top-right corner is used to report vertical displacement for comparison with reference solutions [Schröder et al., 2020]

For the hyperelastic analysis, we adopt a polyconvex strain energy function, whereby the material is characterised by Lamé parameters λ and μ, which relate to the Young's modulus E and Poisson's ratio ν via:

$$\lambda = \frac{E\nu}{(1+\nu)(1-2\nu)}, \quad \mu = \frac{E}{2(1+\nu)}. \tag{5.11}$$

Following the reference benchmark [Schröder et al., 2020], we use the material parameters listed in Table 5.1. These parameters correspond to a nearly incompressible material with Poisson's ratio $\nu \approx 0.3333$. Ultimately, it seen that for a fine mesh and plane-strain, u_y of A approaches *10.59528994 mm*. It is noted that the benchmark utilises a series of tetrahedral meshes with refinements close to an observed stress concentration on the north-western corner of the membrane, whereas this formulation uses quadrilaterals for the individual elements that are doubly-uniform in the h-sense on the reference domain of $[-1,1]^2$.

Table 5.1: Material parameters and applied traction for Cook's membrane benchmark.

Parameter	λ (MPa)	μ (MPa)	p_0 (MPa)
Value	432.099	185.185	20

The second Piola-Kirchhoff stress tensor $\boldsymbol{S}$ is derived from the strain energy function via $\boldsymbol{S} = 2\partial W/\partial \boldsymbol{C}$, where $\boldsymbol{C} = \boldsymbol{F}^T\boldsymbol{F}$:

$$\boldsymbol{S} = \frac{\lambda}{2}(J^2-1)\boldsymbol{C}^{-1} + \mu(\boldsymbol{I} - \boldsymbol{C}^{-1}) \tag{5.12}$$

where $J = \det\boldsymbol{F}$ is the Jacobian determinant.

5.3.2. RESULTS ON A COARSE MESH

To illustrate the mesh and deformation, we first present results for a coarse discretisation consisting of 2×2 spatial elements with a Gauss Lobatto Legendre (GLL) basis. Each element employs 5th-order polynomial basis functions ($N = 5$), with 8th-order integration also on a GLL basis. Note that the mesh is created over a reference $x, y \in [-1,1]^2$ configuration. Figure 5.16 presents the results on deformation for the 2×2 configuration at full load. The deformation at point A is found as *10.58316 mm*, which is already close to the benchmark despite the low number of degrees of freedom.

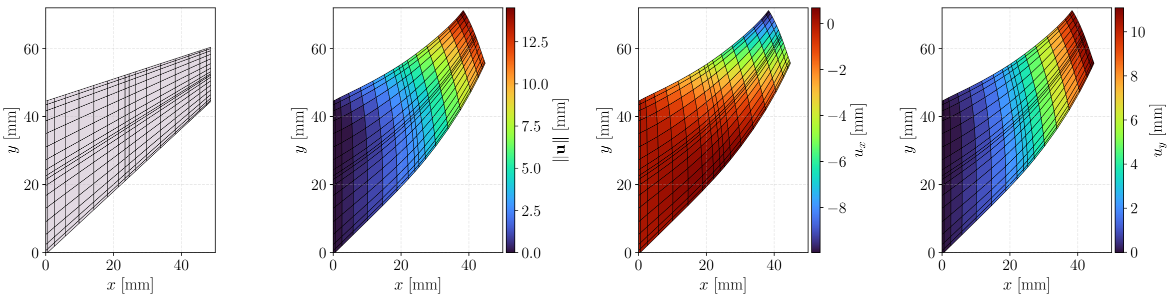

(a) Undeformed, initial configuration illustrating the hybridisation

(b) Displacement magnitude $|\mathbf{u}|$ over the physical configuration at steady state

(c) Horizontal displacement u_x over the physical configuration at steady state

(d) Vertical displacement u_y over the physical configuration at steady state

Figure 5.16: Deformation results for Cook's membrane using a 2×2 element mesh for $N = 5$.

The von Mises stress, commonly used in design criteria for ductile materials, is computed as:

$$\sigma_{\mathrm{vM}} = \sqrt{\sigma_{xx}^2 + \sigma_{yy}^2 - \sigma_{xx}\sigma_{yy} + 3\sigma_{xy}^2} \tag{5.13}$$

This measure provides a useful scalar of stress for failure prediction under the von Mises yield criterion. However, σ_{vM} does not distinguish between regions in tension and compression. To differentiate these loading modes, we also provide the principal stresses (component-wise Cauchy stress terms), which identify the maximum tensile and compressive stress magnitudes and their directions. Figure 5.17 shows these measures. Once again, note that $\sigma_{xy} = \sigma_{yx}$ by upholding conservation of angular momentum, hence only one of these cross-terms is shown.

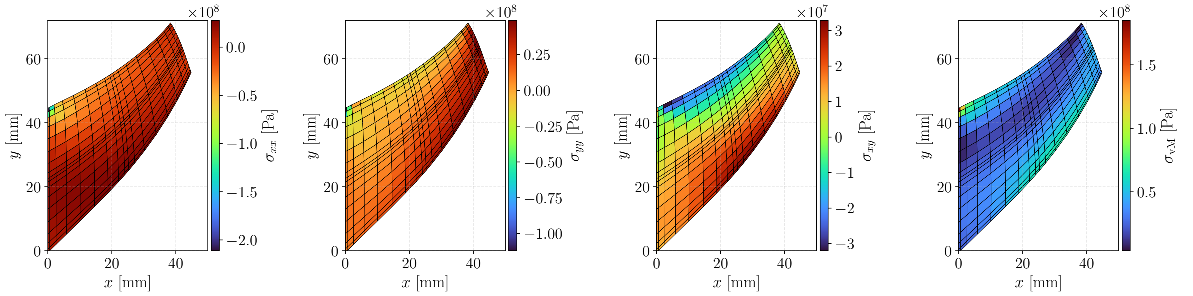

(a) Cauchy σ_{xx} stress over the physical configuration at steady state

(b) Cauchy σ_{yy} stress over the physical configuration at steady state

(c) Cauchy σ_{xy} stress over the physical configuration at steady state

(d) Von mises stress σ_{vM} over the physical configuration at steady state

Figure 5.17: Stress results for Cook's membrane using a 2×2 element mesh for $N = 5$.

In the steady-state limit, the conservation laws derived in Sections 4.6 reduce to balance equations that must be satisfied pointwise across the spatial domain. Since there is no temporal evolution ($\partial/\partial t \equiv 0$), the discrete test functions for symmetries yield equilibrium rather than conservation statements across time slabs. For linear momentum, the translation test function $\widehat{\boldsymbol{\phi}}_\alpha^h = L_t \mathbf{1}$ applied to the steady problem produces the force equilibrium residual. The temporal incidence contributions vanish, and the discrete balance (4.71)-(4.72) reduces to:

$$\mathbf{R}_{\mathrm{lin},\alpha} = \sum_{i \notin \mathcal{I}_D} \left(F_{\mathrm{int},\alpha,i} - F_{\mathrm{ext},\alpha,i} \right) \approx 0, \quad \alpha \in \{x, y\} \tag{5.14}$$

where the summation excludes Dirichlet-constrained nodes $\mathcal{I}_D$. This quantity measures discrete force equilibriums in x y and should vanish to solver tolerance for a converged solution. For angular momentum, the rotation test function $\widehat{\boldsymbol{\phi}}_x^h = -\bar{\boldsymbol{\varphi}}_y$, $\widehat{\boldsymbol{\phi}}_y^h = \bar{\boldsymbol{\varphi}}_x$ yields the moment equilibrium residual. In the absence of temporal derivatives, the balance (4.89) becomes:

$$\mathbf{R}_{\mathrm{ang}} = \sum_{i \notin \mathcal{I}_D} \left(\varphi_{x,i} R_{y,i} - \varphi_{y,i} R_{x,i} \right) \approx 0 \tag{5.15}$$

where $R_{\alpha,i} = F_{\mathrm{int},\alpha,i} - F_{\mathrm{ext},\alpha,i}$ is the nodal force residual. This confirms moment equilibrium of the discrete system. For energy, the velocity test function $\widehat{\boldsymbol{\phi}}_\alpha^h = (1/L_t)\mathbb{E}_t^{(1,0)} \bar{\boldsymbol{\varphi}}_\alpha$ becomes the displacement field itself in the steady limit. The energy balance (4.107) reduces to a work-energy:

$$\mathbf{R}_{\mathrm{en}} = \sum_{i \notin \mathcal{I}_D} \left(\varphi_{x,i} R_{x,i} + \varphi_{y,i} R_{y,i} \right) \approx 0 \tag{5.16}$$

representing the total work done by residual forces, which vanishes at equilibrium. For mass, (4.111) still evaluates how accurately the discrete deformation gradient determinant J^h is computed. Since mass conservation is embedded in the Lagrangian formulation through integration over the fixed reference domain Ω_0, deviations indicate the precision in evaluating (4.110) rather than physical mass loss.

Figure 5.18 visualises the spatial distribution of these balance residuals for the converged Cook's membrane solution. The local values are extremely low ($10^{-12} - 10^{24}$), with the overall global residuals computed to machine precision of $\approx 10^{-14}$. Note that this is not truly machine precision due to iteration errors in computing the solution to the algebraic system, such as, for instance, the logarithm of the condition number of the system (albeit low) being an approximation of the digits lost in a finite representation and still affecting the net solution accuracy.

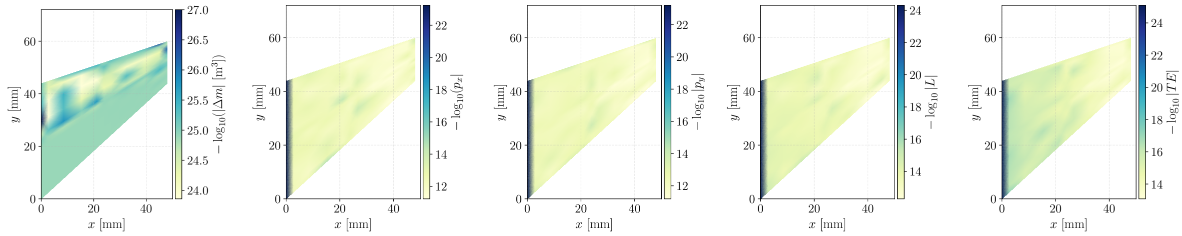

(a) Conservation of total mass

(b) Conservation of linear momentum in x

(c) Conservation of linear momentum in y

(d) Conservation of angular momentum

(e) Conservation of energy

Figure 5.18: Discrete local conservation law balances for Cook's membrane using a 2×2 element mesh for $N = 5$. Values mapped on the initial configuration

5.3.3. *hp*-CONVERGENCE

To validate the accuracy of the mimetic spectral element formulation, we compare the computed vertical displacement u_y at point A against established benchmark values from the literature. The convergence behaviour is assessed by uniformly refining both the polynomial order N and the number of elements in each direction. Figure 5.19a shows the convergence of the computed displacement to the reference benchmark value as the discretisation is refined. It is remarkable to note that the mimetic discretisation is able to have a lower error for a lower order and coarser discretisation, especially considering that the benchmark solution utilises a series of non-uniform refinements to resolve the stress concentration in the northwestern corner (see Figure 5.17d).

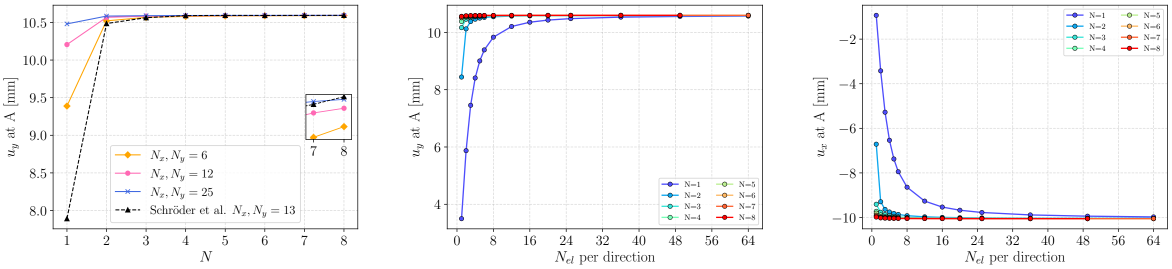

(a) Convergence of vertical displacement u_y at A to the benchmark. A close-up of for 7th and 8th order elements is shown

(b) Vertical displacement u_y at point A vs. number of elements in each direction for various polynomial orders

(c) Horizontal displacement u_x at point A vs. number of elements in each direction for various polynomial orders

Figure 5.19: hp-refinement for Cook's membrane showing convergence of displacement components

To characterize the convergence properties of the spatial discretisation, we conduct two sets of refinement studies: h-refinement (increasing the number of elements N_x, N_y at fixed polynomial order) and p-refinement (increasing the polynomial order N at fixed element count). These studies quantify both horizontal and vertical displacement components at point A to assess the overall accuracy of the deformation prediction. Figure 5.19 presents the h-refinement results, showing the convergence of u_x and u_y as the mesh is refined from coarse to fine resolutions while maintaining a fixed polynomial order. Over-integration is also performed with a Gauss-Lobatto grid with order $N+3$. Figure 5.20 presents the p-refinement results. Multiple curves corresponding to different element counts and polynomial orders illustrate the spectral convergence efficiency of p-refinement for smooth solutions. In particular one can notice from the logarithmic plot in Figure 5.20c, that for about the same number of degrees of freedom, which is indicative of the computational cost associated with the problem, solving at higher N does enable lower errors. As per the large descent in error for $N = 8$, it is likely due to the relative error taken with the same solution order. The convergence studies confirm that MSEM can accurately reproduce the benchmark solution for a hyperelastic Cook's membrane. Both h- and p-refinement exhibit high convergence rates, with p-refinement providing higher rates for the same increase in degrees of freedom. It is noted that for Cook's membrane, there exists a sharp gradient in the stress field at the top left corner, which may attribute to the p-convergence not being exponential. The computed displacements are shown to converge to the reference value for sufficiently refined discretisations, validating the implementation of the generalised isotropic hyperelasticity constitutive model, with spatial discretisation.

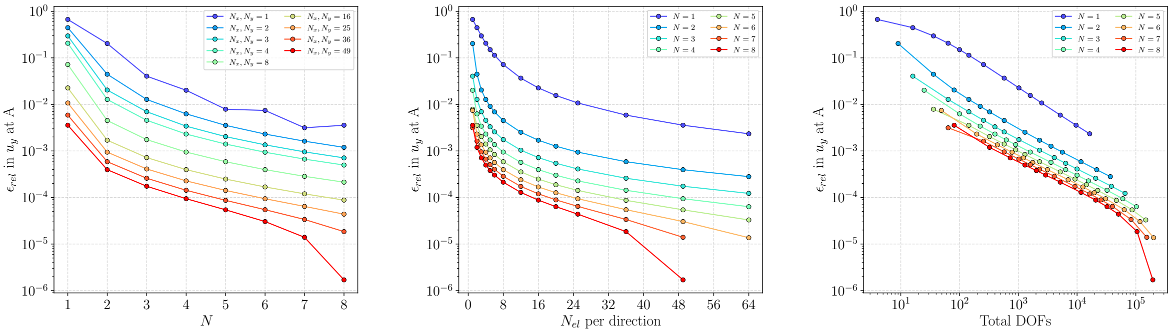

(a) Convergence in u_y of Point A with order N for different resolutions. Each line shows a different resolution in h

(b) Convergence in u_y of A with resolution for different polynomial orders. Each line represents a N value

(c) Convergence in u_y of A with total number of degrees of freedom as a measure. Each line represents a N value

Figure 5.20: Convergence of relative vertical displacement error for hp-refinement

6

CONCLUSIONS

On the premise of structure-preservation as a route to more physically reliable simulations, this work has investigated whether hyperelastic flow can be modelled in a multi-symplectic and variational manner on space-time. The resulting formulation combines a mimetic spectral element method (MSEM) to construct a Lagrangian framework for hyperelastic flow in $\mathbb{R}^3$ (two-dimensional in space and one-dimensional in time.). Large deformations are treated as smooth configuration maps between reference and deformed configurations, with stresses and strains interpreted as geometric measures of how the underlying metric is distorted. Special attention was given to the tensorial nature of continuum mechanics, and to the associated pullback procedure for configuration-dependent variables, to distinguish between various configuration spaces and to enable computation on arbitrary geometries under linear transforms. Additionally, continuum mechanics was revisited from a differential-geometric perspective, making explicit the links between classical kinematics, balance laws and stress measures, and their representation in terms of configuration maps, deformation gradients and bundle-valued differential forms.

Within this setting, the governing equations of hyperelasticity were reformulated in terms of configuration maps and their gradients, and the various stress measures were cast as objects tied naturally either to the reference or to the deformed configuration. Piola-type transformations provide the bridge between these descriptions and clarify how stresses and fluxes should be transferred between configurations. This is compatible with a mimetic spectral element discretisation in space-time, where degrees of freedom are associated with nodes, edges and faces in a way that reflects physical structures. The construction of discrete Hodge operators and metric-dependent maps then provide a means of computing inner products, work terms and hyperelastic stresses at the discrete level. Numerical experiments indicate that these discrete constitutive and metric operations behave in a physically representative manner under refinement.

Conservation properties were addressed by starting from a Lagrangian variational principle on a locally space-time-embedded domain. In this framework, local conservation laws for mass, energy, linear momentum and angular momentum were derived, including the contributions of both natural and strongly-prescribed boundary conditions. Numerical demonstrations confirm that the corresponding discrete conservation laws are upheld to a high degree of accuracy. Total mass, energy sums, and linear and angular momentum residuals remain bounded to within floating-point precision with minor deviations due to solution tolerances and linear solver errors - even in the presence of non-trivial loading and constraints.

The proposed formulation was tested on a collection of steady and time-dependent hyperelastic problems on non-curved space-time geometries. For the time-dependent solutions, convergence with refinement was investigated in the spatial polynomial order p, as well as in both h and p in the temporal direction, the latter corresponding to higher-order implicit time integration schemes. These simulations exhibit physically meaningful and conservative behaviour throughout the evolution, in line with the derived conservation laws. In the steady limit, the formulation compares very well with the plane-strain Cook's membrane benchmark, showing close agreement in the deformation. Together, these findings support an answer to the main question posed at the outset: within the class of problems considered here, Lagrangian hyperelastic flow can indeed be modelled in a multi-symplectic, mimetic spectral element framework on space-time grids;in a way that respects the geometric and variational structure of continuum mechanics.

7

Looking Ahead

Towards scalable, structure-preserving computation. The main recommendation is to adapt the present structure-preserving framework towards faster and more scalable computation, especially under extreme deformations and highly non-linear mappings. Future work should develop dedicated preconditioners [Kolev et al., 2008] [Phillips et al., 2018] and iterative solvers [Bochev et al., 2006] that exploit the block structure and local couplings of the mimetic discretisation, with an eye towards parallel computing. As the number of space-time elements and polynomial degree and geometric complexity increase, the cost of forming and solving the resulting systems grows rapidly. This could be improved by better exploiting tensor-product structure through specialised linear algebra routines or optimising compute hardware. Tensor-product-formed operations with edge bases, in contrast to purely nodal, can be thought of operating with data structures whose values "add up to one", as opposed having ones (i.e. integrated bases [Gerritsma, 2011]). This naturally leads to far more dense data structures.

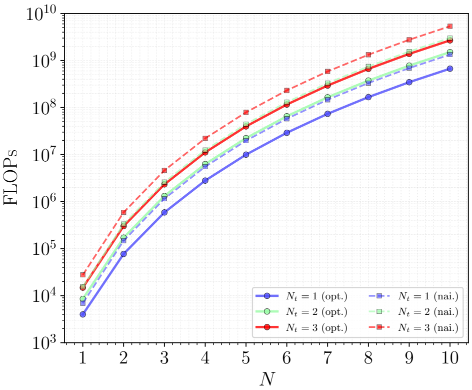

Figure 7.1: Scaling of naive and optimised material Hodge evaluation

A key example is the evaluation of the internal energy Hodge operator and its associated high-order, dense tensor contractions, as recalled in (4.23). These currently represent a significant portion of the overall cost, especially at higher polynomial degrees in space-time. The naive evaluation strategy treats this as a single, 7-index tensor contraction with all indices contracted simultaneously with $\mathcal{O}(N^7)$ complexity - where N represents the cumulative quadrature order in space. But a consider a more optimised, three-step contraction sequence: Contract Jacobian determinant with stress tensor with operation order $\mathcal{O}(N^5)$,

$$\tilde{P}_{ij}^{cde} = P_{ij}^{cde} J^{cde}, \tag{7.1}$$

producing an intermediate tensor indexed by quadrature points and stress components. Contract with weighted ξ-edge basis with operation order $\mathcal{O}(N^6)$,

$$M_{ij}^{cdea} = \sum_{c,d,e} \tilde{P}_{ij}^{cde} \bar{\Psi}_a^{cde}, \tag{7.2}$$

contracting over all quadrature indices with the first basis dimension while preserving spatial-temporal structure. Finally, contract with η-edge basis with operation order $\mathcal{O}(N^7)$,

$$\mathbb{H}_{ij}^{ab} = \sum_{c,d,e} M_{ij}^{cdea} \Psi_b^{cde}. \tag{7.3}$$

where the final step is structured as a now trivially-threadable matrix-matrix multiplication.

While this reduces the operation count by a factor of approximately 2 as per Figure 7.1, for asymptotically large N both paths still scale as $\mathcal{O}(N^7)$, Nevertheless sequence achieves lower costs, as the largest intermediate tensor contains $\mathcal{O}(N^6)$ elements compared to the naive path's $\mathcal{O}(N^7)$ memory footprint. Once again, note that this operation is performed at *every* inner Anderson iteration and would only scale greater in $\mathbb{R}^4$ and for multi-element domains. Future work should therefore focus on reducing these sorts of complexities while retaining the geometric and variational properties that motivate the MSEM approach in the first place. In addition, this would make the validation of *time-dependent* benchmarks and computation of larger, more-resolved problems more feasible [Roth, 2025].

Viscoelasticity and richer constitutive models. In general, the formulation developed in this thesis has been restricted to purely isotropic, hyperelastic materials. In many applications, however, phenomena such as plasticity, directionality, damage, viscosity, etc. play a role in better presenting real materials [Beatty, 1996]. In particular material viscosity leads to physical damping terms in the formulation [Jung-Ho and Noboru, 1985] and additional rigour its conservation laws. This would provide a testbed for viscoelastic modelling, with an explicit energy balance separating conservative and dissipative parts [Boyce and Arruda, 2000]. Extending the bundle-valued and pullback-based framework to such constitutive laws, would test how far the current discretisation can be pushed beyond purely elastic response while maintaining its advantages [Abeyaratne, 2022].

As proof of concept on viscoelasticity, this thesis did shortly explore implementing a non-linear, velocity-dependent damping mechanism. This is done via *operator splitting*, a sort of dimensional splitting where the damping is explicitly treated as a resulting source term [LeVeque, 2002]. However, integrating this dissipative effect into conservation law derivations was deemed out-of-scope. Nevertheless, a sample can be found in Figure 7.2 that bodes well with the general solutions of an underdamped, forced, non-linear mass-spring-damper system, i.e.

$$m(X)\ddot{X} + c(X,t)\dot{x} + k(X,t)x = F(X,t), \qquad \text{where} \quad c > 0. \tag{7.4}$$

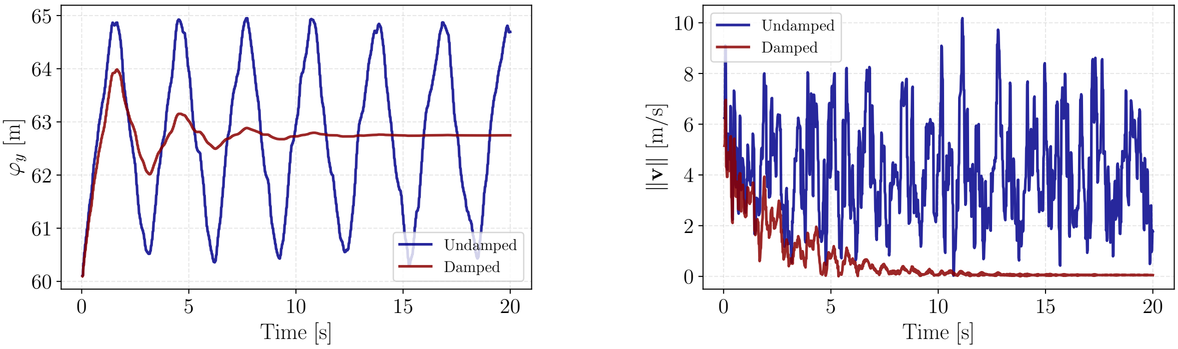

(a) Variation in φ_y with time

(b) Variation in velocity magnitude with time

Figure 7.2: Northeast corner of Cook's membrane as in Subsection 5.2.2, though $\lambda = 50$, $\mu = 25$. A damping coefficient of 25 s^{-1} is used for the damped case

Extension to $\mathbb{R}^4$. The present implementation is limited to two spatial dimensions and one temporal dimension. A direct extension to the $\mathbb{R}^4$, three-dimensional space with a one-dimensional time, manifold would broaden the applicability of the method. This only requires more book-keeping, thanks to the already tensor-product oriented approach to constructing discretisations. However assessing the scaling in computational cost becomes even more relevant.

Coupling, contact, and complex geometries. Another promising direction is to extend the framework to problems with non-physically-uniform domain coupling and generally non-linear geometric mappings - to compute on domains that extend beyond "toy" problems [Kamensky et al., 2015] [Demoures and Gay-Balmaz, 2022] [Ando, 2024]. In particular, fluid–structure interactions could be treated by introducing interfaces and contact methods that respect the mimetic structure on either side of the interface [Mahadev, 2025].

BIBLIOGRAPHY

Abeyaratne, R. (2006). Volume 1. A Brief Review of Some Mathematical Preliminaries. URL: https://web.mit.edu/abeyaratne/lecture_notes.html. Lecture Notes.

Abeyaratne, R. (2012). Volume 2. Continuum Mechanics. URL: https://web.mit.edu/abeyaratne/lecture_notes.html. Lecture Notes.

Abeyaratne, R. (2022). Volume 3. An Introduction to Finite Elasticity. URL: https://web.mit.edu/abeyaratne/lecture_notes.html. Lecture Notes.

Airborne Systems (2020). Airborne Systems' Journey to Mars. URL: https://airborne-sys.com/2020/03/19/airborne-systems-journey-to-mars/. Accessed: 2025-10-20.

Alijani, F. and Amabili, M. (2014). Non-linear vibrations of shells: A literature review from 2003 to 2013. *International Journal of Non-Linear Mechanics*, 58:233–257, ISSN: 0020-7462, DOI: 10.1016/j.ijnonlinmec.2013.09.012.

Anderson, D. G. (1965). Iterative procedures for nonlinear integral equations. *J. ACM*, 12(4):547–560, ISSN: 0004-5411, DOI: 10.1145/321296.321305, URL: https://doi.org/10.1145/321296.321305.

Ando, R. (2024). A cubic barrier with elasticity-inclusive dynamic stiffness. *ACM Trans. Graph.*, 43(6), ISSN: 0730-0301, DOI: 10.1145/3687908.

Angoshtari, A. and Yavari, A. (2013). A geometric structure-preserving discretization scheme for incompressible linearized elasticity. *Computer Methods in Applied Mechanics and Engineering*, 259:130–153, ISSN: 0045-7825, DOI: 10.1016/j.cma.2013.03.004.

Anssari-Benam, A. and Bucchi, A. (2021). A generalised neo-Hookean strain energy function for application to the finite deformation of elastomers. *International Journal of Non-Linear Mechanics*, 128:103626, ISSN: 0020-7462, DOI: 10.1016/j.ijnonlinmec.2020.103626.

Ariza, P. and Ortiz, M. (2005). Discrete crystal elasticity and discrete dislocations in crystals. *Archive for Rational Mechanics and Analysis*, 178:149–226, DOI: 10.1007/s00205-005-0391-4.

Arnold, D., Falk, R., and Winther, R. (2010). Finite Element Exterior Calculus: from Hodge theory to numerical stability. *Bulletin of the American Mathematical Society*, 47(2):281–354, ISSN: 1088-9485, DOI: 10.1090/s0273-0979-10-01278-4.

Arnold, D. and Winther, R. (2001). Mixed finite elements for elasticity. *Numerische Mathematik*, 92, DOI: 10.1007/s002110100348.

Arnold, D. N., Falk, R. S., and Winther, R. (2006). Finite element exterior calculus, homological techniques, and applications. *Acta Numerica*, 15:1–155, DOI: 10.1017/S0962492906210018.

Beatty, M. F. (1996). *Introduction to Nonlinear Elasticity*, pages 13–112. Springer US, Boston, MA, ISBN: 978-1-4613-0329-9, DOI: 10.1007/978-1-4613-0329-9_2.

Bernd Sautter, K., Meßmer, M., Teschemacher, T., and Bletzinger, K.-U. (2022). Limitations of the St. Venant–Kirchhoff material model in large strain regimes. *International Journal of Non-Linear Mechanics*, 147:104207, ISSN: 0020-7462, DOI: https://doi.org/10.1016/j.ijnonlinmec.2022.104207.

Bochev, P. (2003). A discourse on variational and geometric aspects of stability of discretizations. Lecture Series.

Bochev, P., Garasi, C., Hu, J., Robinson, A., and Tuminaro, R. (2006). An Improved Algebraic Multigrid Method for Solving Maxwell's Equations. *SIAM Journal on Scientific Computing*, 25:623–642, DOI: 10.1137/S1064827502407706.

Bochev, P. B. and Hyman, J. M. (2006). Principles of mimetic discretizations of differential operators. In Arnold, D. N., Bochev, P. B., Lehoucq, R. B., Nicolaides, R. A., and Shashkov, M., editors, *Compatible Spatial Discretizations*, pages 89–119, New York, NY. Springer New York, ISBN: 978-0-387-38034-6.

Bossavit, A. (1988). Whitney forms: a class of finite elements for three-dimensional computations in electromagnetism. *IEE Proceedings A: Physical Science, Measurement and Instrumentation, Management and Education, Reviews*, 135(8):493–500, DOI: 10.1049/ip-a-1:19880077.

Bossavit, A. (1999). Computational electromagnetism and geometry. *J Japan Soc Appl Elctromagn & Mech*, 7. The Japanese Paper series.

Boyce, M. C. and Arruda, E. M. (2000). Constitutive models of rubber elasticity: A review. *Rubber Chemistry and Technology*, 73(3):504–523, ISSN: 0035-9475, DOI: 10.5254/1.3547602.

Breslavsky, I. D., Amabili, M., and Legrand, M. (2014). Nonlinear vibrations of thin hyperelastic plates. *Journal of Sound and Vibration*, 333(19):4668–4681, ISSN: 0022-460X, DOI: https://doi.org/10.1016/j.jsv.2014.04.028.

Brezzi, F. (1974). On the existence, uniqueness and approximation of saddle-point problems arising from Lagrangian multipliers. *Revue française d'automatique, informatique, recherche opérationnelle*, 8(2):129–151, DOI: 10.1051/m2an/197408R201291.

Brezzi, F., Douglas, J., and Marini, L. D. (1985). Two families of mixed finite elements for second order elliptic problems. *Numerische Mathematik*, 47(2):217–235, DOI: doi.org/10.1007/BF01389710.

Ciarlet, P. and Li, D. (2008). *Differential Geometry: Theory and Applications*. Series in contemporary applied mathematics. Higher Education Press, ISBN: 9789812771469.

Ciarlet, P. G. (2002). *The Finite Element Method for Elliptic Problems*. Society for Industrial and Applied Mathematics, DOI: 10.1137/1.9780898719208.

Cline, D. (2017). *Variational principles in classical mechanics*. University of Rochester River Campus Libraries, University of Rochester, ISBN: 9780998837246.

Cook, R. D. (1974). Improved two-dimensional finite element. *Journal of the Structural Division*, 100(9):1851–1863, DOI: 10.1061/JSDEAG.0003877.

Crane, K., de Goes, F., Desbrun, M., and Schröder, P. (2013). Digital geometry processing with Discrete Exterior Calculus. In *ACM SIGGRAPH 2013 courses*, SIGGRAPH '13, New York, NY, USA. ACM.

Dastjerdi, S., Alibakhshi, A., Akg oz, B., and Civalek, O. (2022a). A novel nonlinear elasticity approach for analysis of nonlinear and hyperelastic structures. *Engineering Analysis with Boundary Elements*, 143:219–236, ISSN: 0955-7997, DOI: 10.1016/j.enganabound.2022.06.015.

Dastjerdi, S., Malikan, M., Akg oz, B., Civalek, O., Wiczenbach, T., and Eremeyev, V. A. (2022b). On the deformation and frequency analyses of SARS-CoV-2 at nanoscale. *International Journal of Engineering Science*, 170:103604, ISSN: 0020-7225, DOI: 10.1016/j.ijengsci.2021.103604.

Delft High Performance Computing Centre, D. (2024). DelftBlue Supercomputer (Phase 2). URL: https://www.tudelft.nl/dhpc/ark:/44463/DelftBluePhase2.

Demoures, F. and Gay-Balmaz, F. (2022). Unified discrete multisymplectic Lagrangian formulation for hyperelastic solids and barotropic fluids. *Journal of Nonlinear Science*, 32(6), ISSN: 1432-1467, DOI: 10.1007/s00332-022-09849-y.

Demoures, F., Gay-Balmaz, F., and Ratiu, T. S. (2013). Multisymplectic variational integrators and space/time symplecticity. URL: https://arxiv.org/abs/1310.4772.

Desbrun, M., Hirani, A. N., Leok, M., and Marsden, J. E. (2005). Discrete Exterior Calculus. URL: https://arxiv.org/abs/math/0508341.

Evans, C., Pollock, S., Rebholz, L. G., and Xiao, M. (2019). A proof that Anderson acceleration improves the convergence rate in linearly converging fixed point methods (but not in those converging quadratically). URL: https://arxiv.org/abs/1810.08455.

Frankel, T. (2011). *The Geometry of Physics: An Introduction*. Cambridge University Press, 3 edition.

Fu, Y. and Ogden, R. (2001). *Nonlinear Elasticity: Theory and Applications*. London Mathematical Society Lecture Note Series. Cambridge University Press.

Gedney, S. D. (2011). *Yee Algorithm for Maxwell's Equations*, pages 39–73. Springer International Publishing, Cham, ISBN: 978-3-031-01712-4, DOI: 10.1007/978-3-031-01712-4_3.

Gent, A. N. (1996). A new constitutive relation for rubber. *Rubber Chemistry and Technology*, 69(1):59–61, ISSN: 0035-9475, DOI: 10.5254/1.3538357.

Georgi, H. (1993). *The Physics of Waves*. Prentice Hall, ISBN: 9780136656210.

Gerritsma, M. (2011). Edge functions for spectral element methods. In Hesthaven, J. S. and Rønquist, E. M., editors, *Spectral and High Order Methods for Partial Differential Equations*, pages 199–207, Berlin, Heidelberg. Springer Berlin Heidelberg, ISBN: 978-3-642-15337-2.

Gerritsma, M. (2012). An introduction to a compatible spectral discretization method. *Mechanics of Advanced Materials and Structures*, 19(1-3):48–67, DOI: 10.1080/15376494.2011.572237.

Gerritsma, M., Hiemstra, R., Kreeft, J., Palha, A., Rebelo, P., and Toshniwal, D. (2014). The geometric basis of numerical methods. In Azaïez, M., El Fekih, H., and Hesthaven, J. S., editors, *Spectral and High Order Methods for Partial Differential Equations - ICOSAHOM 2012*, pages 17–35, Cham. Springer International Publishing, ISBN: 978-3-319-01601-6.

Griffiths, D. J. (2017). *Introduction to Electrodynamics*. Cambridge University Press, 4 edition.

Griffiths, D. J. and Schroeter, D. F. (2018). *Introduction to quantum mechanics*. Cambridge University Press, Cambridge ; New York, NY, third edition edition, ISBN: 978-1-107-18963-8.

Haberman, R. (2013). *Applied Partial Differential Equations: With Fourier Series and Boundary Value Problems*. Always learning. Pearson, ISBN: 978-0-321-79705-6, URL: https://books.google.nl/books?id=hGNwLgEACAAJ.

Hackett, R. M. (2018). *Strain-Energy Functions*, pages 19–28. Springer International Publishing, Cham, ISBN: 978-3-319-73201-5, DOI: 10.1007/978-3-319-73201-5_4.

Hairer, E., Lubich, C., and Wanner, G. (2013). *Geometric Numerical Integration: Structure-Preserving Algorithms for Ordinary Differential Equations*. Springer Series in Computational Mathematics. Springer Berlin Heidelberg, ISBN: 9783662050187.

Harlow, F. H. and Amsden, A. A. (1968). Numerical calculation of almost incompressible flow. *Journal of Computational Physics*, 3(1):80–93.

Hassler, W. (1957). *Geometric Integration Theory*. Princeton Legacy Library, ISBN: 9780691652900.

Hatcher, A. (2002). *Algebraic Topology*. Algebraic Topology. Cambridge University Press, ISBN: 9780521795401.

Hirani, A. N. (2003). Discrete Exterior Calculus. URL: https://api.semanticscholar.org/CorpusID:15032612. Doctoral Thesis.

Holzapfel, G. A. and Ogden, R. W. (2025). Modeling the biomechanical properties of soft biological tissues: Constitutive theories. *European Journal of Mechanics - A/Solids*, 112:105634, ISSN: 0997-7538, DOI: 10.1016/j.euromechsol.2025.105634.

Hooke, R. (1678). *Lectures de Potentia Restitutiva, Or of Spring Explaining the Power of Springing Bodies*. Number 6 in [Cutlerian lecture. John Martyn, Pico de Teide, URL: https://books.google.nl/books?id=LAtPAAAAcAAJ.

Horgan, C. O. (2021). A note on a class of generalized neo-Hookean models for isotropic incompressible hyperelastic materials. *International Journal of Non-Linear Mechanics*, 129:103665, ISSN: 0020-7462, DOI: 10.1016/j.ijnonlinmec.2020.103665.

Hu, K. and Xu, J. (2017). Structure-preserving finite element methods for stationary MHD models. URL: https://arxiv.org/abs/1503.06160.

Hyman, J. and Scovel, J. (2005). Deriving mimetic difference approximations to differential operators using algebraic topology.

Hyman, J., Shashkov, M., and Steinberg, S. (1997). The numerical solution of diffusion problems in strongly heterogeneous non-isotropic materials. *Journal of Computational Physics*, 132(1):130–148, ISSN: 0021-9991, DOI: https://doi.org/10.1006/jcph.1996.5633.

Jain, V., Fisser, J., Palha, A., and Gerritsma, M. (2020a). A conservative hybrid method for Darcy flow. In Sherwin, S. J., Moxey, D., Peiró, J., Vincent, P. E., and Schwab, C., editors, *Spectral and High Order Methods for Partial Differential Equations ICOSAHOM 2018*, pages 215–227, Cham. Springer International Publishing, ISBN: 978-3-030-39647-3.

Jain, V., Zhang, Y., Palha, A., and Gerritsma, M. (2020b). Construction and application of algebraic dual polynomial representations for finite element methods on quadrilateral and hexahedral meshes. URL: https://arxiv.org/abs/1712.09472.

Jung-Ho, C. and Noboru, K. (1985). An analysis of metal forming processes using large deformation elastic-plastic formulations. *Computer Methods in Applied Mechanics and Engineering*, 49(1):71–108, ISSN: 0045-7825, DOI: 10.1016/0045-7825(85)90051-9.

Kamensky, D., Hsu, M.-C., Schillinger, D., Evans, J. A., Aggarwal, A., Bazilevs, Y., Sacks, M. S., and Hughes, T. J. (2015). An immersogeometric variational framework for fluid–structure interaction: Application to bioprosthetic heart valves. *Computer Methods in Applied Mechanics and Engineering*, 284:1005–1053, ISSN: 0045-7825, DOI: 10.1016/j.cma.2014.10.040. Isogeometric Analysis Special Issue.

Kanso, E., Arroyo, M., Tong, Y., Yavari, A., Marsden, J., and Desbrun, M. (2007). On the geometric character of stress in continuum mechanics. *Zeitschrift für angewandte Mathematik und Physik ZAMP*, 58, DOI: 10.1007/s00033-007-6141-8.

Khan Academy (2025). Spring Force and Hooke's Law. URL: https://www.khanacademy.org/science/ap-college-physics-1/xf557a762645cccc5:force-and-translational-dynamics/xf557a762645cccc5:spring-force/a/what-is-hookes-law. Accessed: 2025-10-20.

Khaniki, H. B., Ghayesh, M. H., Chin, R., and Amabili, M. (2023). Hyperelastic structures: A review on the mechanics and biomechanics. *International Journal of Non-Linear Mechanics*, 148:104275, ISSN: 0020-7462, DOI: 10.1016/j.ijnonlinmec.2022.104275.

Kolev, T., Pasciak, J., and Vassilevski, P. (2008). H(curl) auxiliary mesh preconditioning. *Numerical Linear Algebra with Applications*, 15:455 – 471, DOI: 10.1002/nla.534.

Kreeft, J. and Gerritsma, M. (2013). Mixed mimetic spectral element method for stokes flow: A pointwise divergence-free solution. *Journal of Computational Physics*, 240:284–309, ISSN: 0021-9991, DOI: 10.1016/j.jcp.2012.10.043.

Leok, M. and Ohsawa, T. (2011). Variational and geometric structures of discrete Dirac mechanics. *Foundations of Computational Mathematics*, 11(5):529–562, ISSN: 1615-3383, DOI: 10.1007/s10208-011-9096-2.

LeVeque, R. J. (2002). *Finite Volume Methods for Hyperbolic Problems*. Cambridge Texts in Applied Mathematics. Cambridge University Press.

Lilly, K. E. (1966). On the application of the eddy viscosity concept in the inertial sub-range of turbulence. In *Diffusion*. URL: https://api.semanticscholar.org/CorpusID:55104948.

Lipnikov, K., Shashkov, M., and Svyatskiy, D. (2006). The mimetic finite difference discretization of diffusion problem on unstructured polyhedral meshes. *J. Comput. Phys.*, 211(2):473–491, ISSN: 0021-9991, DOI: 10.1016/j.jcp.2005.05.028.

Lohi, J. and Kettunen, L. (2021). Whitney forms and their extensions. *Journal of Computational and Applied Mathematics*, 393:113520, ISSN: 0377-0427, DOI: 10.1016/j.cam.2021.113520.

Lubbers, L. A., van Hecke, M., and Coulais, C. (2017). A nonlinear beam model to describe the postbuckling of wide neo-Hookean beams. *Journal of the Mechanics and Physics of Solids*, 106:191–206, ISSN: 0022-5096, DOI: https://doi.org/10.1016/j.jmps.2017.06.001.

Mahadev, M. (2025). Lagrangian methods for inviscid barotropic flow. URL: https://resolver.tudelft.nl/uuid:c560b53e-16e3-41e2-a183-c902a171c134. Master's thesis.

Marsden, J. E., Hughes, T. J. R., and Carlson, D. E. (1984). Mathematical Foundations of Elasticity. *Journal of Applied Mechanics*, 51(4), ISSN: 0021-8936, DOI: 10.1115/1.3167757.

Marsden, J. E., Pekarsky, S., Shkoller, S., and West, M. (2001). Variational methods, multisymplectic geometry and continuum mechanics. *Journal of Geometry and Physics*, 38(3–4):253–284, ISSN: 0393-0440, DOI: 10.1016/s0393-0440(00)00066-8.

Mooney, M. (1940). A theory of large elastic deformation. *Journal of Applied Physics*, 11(9):582–592, ISSN: 0021-8979, DOI: 10.1063/1.1712836.

Mylapilli, H. and Udwadia, F. E. (2017). Control of three-dimensional incompressible hyperelastic beams. *Nonlinear Dynamics*, 90(1):115–135, ISSN: 1573-269X, DOI: 10.1007/s11071-017-3651-6.

Nédélec, J. C. (1980). Mixed finite elements in $\mathbb{R}^3$. *Numerische Mathematik*, 35:315–341, DOI: doi.org/10.1007/BF01396415.

Noether, E. (1918). Invariante variationsprobleme. *Nachrichten von der Gesellschaft der Wissenschaften zu Göttingen, Mathematisch-Physikalische Klasse*, 1918:235–257, URL: http://eudml.org/doc/59024.

Noll, W. (1974). *A New Mathematical Theory of Simple Materials*, pages 243–292. Springer Berlin Heidelberg, Berlin, Heidelberg, ISBN: 978-3-642-65817-4, DOI: 10.1007/978-3-642-65817-4_15.

Ogden, R. W. (1973). Large deformation isotropic elasticity—on the correlation of theory and experiment for incompressible rubberlike solids. *Rubber Chemistry and Technology*, 46(2):398–416, ISSN: 0035-9475, DOI: 10.5254/1.3542910.

Olesen, K., Gervang, B., Reddy, J. N., and Gerritsma, M. (2018). A higher-order equilibrium finite element method. *International Journal for Numerical Methods in Engineering*, 114(12):1262–1290, DOI: 10.1002/nme.5785.

Palha, A. (2013). High order mimetic discretization. development and application to Laplace and advection problems in arbitrary quadrilaterals. URL: https://resolver.tudelft.nl/uuid:573b66ff-f740-446a-8d46-3466dfbab679. Doctoral thesis.

Palha, A. and Gerritsma, M. (2015). Mimetic spectral element method for Hamiltonian systems. *arXiv: Numerical Analysis*, DOI: arxiv.org/abs/1505.03422.

Palha, A., Pinto Rebelo, P., Hiemstra, R., Kreeft, J., and Gerritsma, M. (2014). Physics-compatible discretization techniques on single and dual grids, with application to the Poisson equation of volume forms. *Journal of Computational Physics*, 257:1394–1422, ISSN: 0021-9991, DOI: 10.1016/j.jcp.2013.08.005.

Pedregal, P. (2000). *Variational Methods in Nonlinear Elasticity*. Society for Industrial and Applied Mathematics, DOI: 10.1137/1.9780898719529, URL: https://epubs.siam.org/doi/abs/10.1137/1.9780898719529.

Phil and Mama (2020). Foolproof Japanese Souffle Cheesecake Recipe. URL: https://www.philandmama.com/adventures/2020/4/20/foolproof-japanese-souffle-cheesecake-recipe-make-a-jiggly-japanese-cheesecake-that-doesnt-flatten-or-crack. Accessed: 2025-10-20.

Phillips, E., Shadid, J., and Cyr, E. (2018). Scalable preconditioners for structure preserving discretizations of maxwell equations in first order form. *SIAM Journal on Scientific Computing*, 40:B723–B742, DOI: 10.1137/17M1135827.

Pucci, E. and Saccomandi, G. (2002). A note on the Gent model for rubber-like materials. *Rubber Chemistry and Technology*, 75(5):839–852, ISSN: 0035-9475, DOI: 10.5254/1.3547687.

Rashad, R., Brugnoli, A., Califano, F., Luesink, E., and Stramigioli, S. (2023). Intrinsic nonlinear elasticity: An exterior calculus formulation. *Journal of Nonlinear Science*, 33(5), ISSN: 1432-1467, DOI: 10.1007/s00332-023-09945-7.

Raviart, P. A. and Thomas, J. M. (1977). A mixed finite element method for 2nd order elliptic problems. In Galligani, I. and Magenes, E., editors, *Mathematical Aspects of Finite Element Methods*, pages 292–315, Berlin, Heidelberg. Springer Berlin Heidelberg, ISBN: 978-3-540-37158-8.

Reddy, J. N. (2013). *An Introduction to Continuum Mechanics*. Cambridge University Press, 2 edition.

Rivlin, R. S. (1948). Large Elastic Deformations of Isotropic Materials. IV. Further Developments of the General Theory. *Philosophical Transactions of the Royal Society of London. Series A, Mathematical and Physical Sciences*, 241(835):379–397, ISSN: 00804614.

Roth, J. (2025). Locally hp-Adaptive MSEM Method. URL: https://resolver.tudelft.nl/uuid:b1d864a1-4097-43fc-8b85-0bac4cfa50e1. Master's thesis.

Rougée, P. (2006). An intrinsic Lagrangian statement of constitutive laws in large strain. *Computers & Structures*, 84(17):1125–1133, ISSN: 0045-7949, DOI: 10.1016/j.compstruc.2006.01.009. Formulations and Computational Models for Finite Strains.

Schröder, J., Wick, T., Reese, S., Wriggers, P., Müller, R., Kollmannsberger, S., Kästner, M., Schwarz, A., Igelbüscher, M., Viebahn, N., Bayat, H. R., Wulfinghoff, S., Mang, K., Rank, E., Bog, T., d'angella, D., Elhaddad, M., Hennig, P., Düster, A., and Heister, T. (2020). A selection of benchmark problems in solid mechanics and applied mathematics. *Archives of Computational Methods in Engineering*, 28:1–39, DOI: 10.1007/s11831-020-09477-3.

Sharma, R. (2023). Development and application of bundle-valued forms in hybrid mimetic spectral element method. URL: https://resolver.tudelft.nl/uuid:eb5a414a-e07b-4176-920f-caa4872e20e4. Master's thesis.

Shrestha, S. (2022). Hybridised Mimetic Discretisation and Variational Multiscale Theory for Advection-Dominated Problems. URL: https://resolver.tudelft.nl/uuid:afb6f8c2-58e7-42d6-b765-de30bad8e302. Master's thesis.

Stern, A. and Desbrun, M. (2006). Discrete geometric mechanics for variational time integrators. In *ACM SIGGRAPH 2006 Courses*, SIGGRAPH '06, page 75–80, New York, NY, USA. Association for Computing Machinery, ISBN: 1595933646, DOI: 10.1145/1185657.1185669.

Tonti, E. (1971). On the mathematical structure of a large class of physical theories. *Rend. Acc. Lincei*, 52:13.

Tonti, E. (1975). The formal structure of physical theories. Lecture Series.

Tonti, E. (2000). On the geometrical structure of electromagnetism. URL: https://api.semanticscholar.org/CorpusID:16758833.

Tonti, E. (2013). *Birth of Classification Diagrams*, pages 221–238. Springer New York, New York, NY, ISBN: 978-1-4614-7422-7, DOI: 10.1007/978-1-4614-7422-7_8.

Treloar, L. R. G. (1943). The elasticity of a network of long-chain molecules—II. *Trans. Faraday Soc.*, 39:241–246, DOI: 10.1039/TF9433900241.

Truesdell, C., Noll, W., and Pipkin, A. C. (1966). The non-linear field theories of mechanics. *Journal of Applied Mechanics*, 33(4):958–958, ISSN: 0021-8936, DOI: 10.1115/1.3625229.

Versteeg, H. and Malalasekera, W. (2007). *An Introduction to Computational Fluid Dynamics: The Finite Volume Method*. Pearson Education Limited, ISBN: 9780131274983.

Walker, H. F. and Ni, P. (2011). Anderson Acceleration for Fixed-Point Iterations. *SIAM Journal on Numerical Analysis*, 49(4):1715–1735, DOI: 10.1137/10078356X.

Yavari, A. (2008). On geometric discretization of elasticity. *Journal of Mathematical Physics*, 49, DOI: 10.1063/1.2830977.

Zhang, Y. (2022). Mimetic spectral element method and extensions toward higher computational efficiency. URL: https://doi.org/10.4233/uuid:a87e7be3-fb08-4706-9676-a6ae43f5aa0d. Doctoral thesis.

Zhang, Y., Fisser, J., and Gerritsma, M. (2021). A hybrid mimetic spectral element method for three-dimensional linear elasticity problems. *Journal of Computational Physics*, 433:110179, ISSN: 0021-9991, DOI: 10.1016/j.jcp.2021.110179.

Zhang, Y., Palha, A., Gerritsma, M., and Rebholz, L. G. (2022). A mass-, kinetic energy- and helicity-conserving mimetic dual-field discretization for three-dimensional incompressible Navier-Stokes equations, part i: Periodic domains. *Journal of Computational Physics*, 451:110868, ISSN: 0021-9991, DOI: 10.1016/j.jcp.2021.110868.

Zienkiewicz, O., Morgan, K., and Morgan, K. (2006). *Finite Elements and Approximation*. Dover books on engineering. Dover Publications, ISBN: 9780486453019.